Chapter 5
Morphology, Chemical, and Phase Composition of Electrodeposited Co–Ni, Fe–Ni, and Mo–Ni–O Powders

V.D. Jović, U.Č. Lačnjevac, and B.M. Jović

5.1 Introduction

The alloy powders of the iron-group metals are of great interest for many industrial applications [1–88].

Ultrafine Co–Ni powders showed significant promise for future development of hard materials [1, 2], magnetic materials [3–5], commercial batteries [6], catalysts [7–9], catalyzing electroplates [10, 11], hydrogen absorbing alloy anodes [12], and magnetoresistive sensors [13, 14]. The powders for these applications were made by several different techniques such as mechanical alloying–ball milling [15, 16], sonochemical synthesis [17–19], chemical reduction [13, 14, 20–23], synthesis in microemulsion [24, 25], gas evaporation [26, 27], multimellow reduction [28, 29], coprecipitation [30], gas reduction [31, 32], freeze-drying [33], and spray pyrolysis [34]. Depending on the technique used for powders synthesis, dimensions of Co–Ni powder particles varied from 40 nm [33] to 700 nm [34]. Unfortunately, limited number of papers concerning Co–Ni powder

V.D. Jović (✉) • U.Č. Lačnjevac • B.M. Jović
Department of Materials Science, Institute for Multidisciplinary Research, University of Belgrade, Kneza Višeslava 1, P.O. Box 33, Belgrade 11030, Serbia
e-mail: vladajovic@imsi.rs; uros.lacnjevac@imsi.rs; bjovic@imsi.rs

Stojan S. Djokić (ed.), *Electrochemical Production of Metal Powders*, Modern Aspects of Electrochemistry 54, DOI 10.1007/978-1-4614-2380-5_5,

electrodeposition exists in the literature [35–40]. Among them four are our publications [37–41]. As shown in these papers [37–41], the morphology and composition of electrodeposited powders were found to be sensitive to the solution composition (to the ratio of Ni^{2+}/Co^{2+} ions concentration).

Fe–Ni-based alloy powders are known as promising soft magnetic materials with low coercivity and high permeability [42–66]. Most of the literature data concerning the procedure of their production deal with the mechanical alloying using ball-milling process [42–55]. It is shown that the grain size of particles is closely related to the magnetic properties of Fe–Ni alloy powders obtained by mechanical alloying, being also very sensitive to the conditions of ball-milling process (the vial rotation speed, the disc rotation speed, and the time of milling). Gas condensation method using Ar with H_2 as convection gas is used for preparing nanograined Fe–12Ni powders [56]. In this investigation it is shown that the fcc-to-bcc phase transformation might be inhibited if the grain size is sufficiently small (below 27 nm). Nanocrystalline $FeNi_3$ powders with the particles size of 40–50 nm, prepared by powder processing (calcination of the Fe: Ni = 1:3 mixture of Fe and Ni oxalates with subsequent annealing in hydrogen atmosphere at 600°C), showed higher coercive force and lower permeability, with such behavior being explained by the role of interfacial regions in the samples [57]. Hydrodynamic electrospray technique [58] and electroless plating procedure [59] were also used for the synthesis of nanosized Fe–Ni powders. Recently it is discovered that these powders could be used for the absorption of electromagnetic waves [60, 61], which is a very important issue for both commercial and military application. Fe–Ni nanofibers for this application were synthesized by calcination and subsequent hydrogen reduction of electrospun Fe, Ni nitrates, and polystyrene [61].

Among our recent papers [62, 63] the electrodeposition of Fe–Ni alloy powders was the subject of only few papers. Zhelibo et al. [64, 65] suggested a method for producing very fine Fe–Ni alloy powder by electrolysis in a two-layer electrolytic bath, using a hydrocarbon solvent from an oil refining fraction as an upper organic layer with evaporation at 180°C, and subsequent reduction annealing in a hydrogen atmosphere. The influence of the reduction annealing temperature [64] and the electrolysis temperature [65] on the formation,

chemical and phase composition, structure, and magnetic properties of highly dispersed Fe–Ni alloy powders were investigated and the optimal thermal conditions for the production of powders with micron-sized particles were determined [64, 65]. The effect of complexing agents (citric and oxalic acid) on the process of Fe–Ni alloy powders was also investigated [66]. It was shown that complexing agents influence the kinetics of powders electrodeposition as well as the morphology of the Fe–Ni powders. Finer powders were produced in the presence of citric acid in comparison with those obtained in the presence of oxalic acid [66].

The subject of our recent investigations was the analysis of morphology and composition of electrodeposited Fe–Ni powders as a function of the solution composition [62], as well as the possibility of $NiFe_2O_4$ formation after additional oxidation of electrodeposited powders [63].

One of the components of the Fe–Ni system, formed by oxidation of Fe–Ni mixture at high temperatures, is a nickel ferrite, $NiFe_2O_4$, an inverse spinel in which the tetrahedral sites are occupied by Fe^{3+} ions and octahedral sites by Fe^{3+} and Ni^{2+} ions [67].

According to the literature [68, 69], the $NiFe_2O_4$ is the most suitable material for device applications in the upper microwave and lower millimeter wave ranges. At the same time, $NiFe_2O_4$ was found to be a highly reproducible humidity [70] and gas [71, 72] sensor material. Numerous techniques, such as ferrite plating [73, 74], oxidation of metallic films [75], arc plasma method [76], chemical transport [77, 78], chemical vapor deposition [79–82], the dip coating process [83], spray pyrolysis [84, 85], and pulsed wire discharge [86], have been used for the preparation of $NiFe_2O_4$ films. The main difficulty of these methods is the limit in the choice of substrate material, since it must be kept at a high temperature after deposition. In the work of Sartale et al. [87] less expensive and more popular method for the preparation of the spinel nanocrystalline $NiFe_2O_4$ films has been proposed. The procedure was based on the electrodeposition of $NiFe_2$ alloy coating from a nonaqueous ethylene glycol sulfate bath and subsequent electrochemical oxidation of the alloy in an aqueous alkaline bath at room temperature. It is shown that the air annealing of the as-deposited $NiFe_2O_4$ thin films at 500°C for 5 h improved the crystallinity and morphology of the films.

In the work of Fang et al. [88] the $NiFe_2O_4$ ultrafine powder with high crystallinity has been prepared through a reverse microemulsion route. After optimizing the composition in the starting solution, the resulting $NiFe_2O_4$ was formed at a temperature of about 550–600°C, which is much lower than that observed from the solid state reaction. Magnetic investigation indicates that samples are soft magnetic materials with low coercivity and with the saturation magnetization close to the bulk value of nickel ferrite. Most recently $NiFe_2O_4$ nanoparticles were synthesized via solid state reaction process of the $Fe_{67}Ni_{33}$ alloy nanopowder at different annealing temperatures in the air [89]. It was shown by XRD and TEM analysis that $NiFe_2O_4$ started to form at around 450°C, being well defined after annealing at 550°C with the powder particle size ranging between 15 and 50 nm.

The Mo–Ni alloys possess several useful properties: exceptional corrosion and wearing resistance [90–92], high catalytic activity for hydroprocessing of aromatic oils [93], and gas phase hydrogenation of benzene [94], as well as high hardness [95]. Their catalytic activity for hydrogen evolution has been one of the most investigated properties in the literature [96–110].

The Mo–Ni alloys can be produced by several methods, from which metallurgical ones are not convenient because of easy oxidation and high melting temperature of molybdenum. The powder metallurgy and mechanical alloying [111, 112], spark plasma sintering [113], and laser cladding [114] are mostly used for the Mo–Ni alloy preparation. Recently, coated superconductor tapes of high mechanical strength were made of the Mo–Ni alloy powder by rolling assisted biaxially textured substrates method (RABiTS™) [115].

All the above-mentioned methods are expensive in comparison with the electrodeposition of Mo–Ni alloy coatings. Although molybdenum cannot be separately deposited from aqueous solutions, it can be codeposited with the iron-group metals (Fe, Co, Ni) in the presence of appropriate complexing agents, by the type of alloy electrodeposition defined by Brenner [116] as induced codeposition.

Most of the papers concerning electrodeposition of compact Mo–Ni alloy coatings are dealing with the mechanism of their electrodeposition (mechanism of induced codeposition), and according to the literature, the most probable mechanism is the one reported by Podlaha and Landolt [117–120].

It should be emphasized here that, except our recent papers [121–123], there are no papers in the literature concerning electrodeposition of Mo–Ni alloy powders (actually powders of the system Mo–Ni–O) and their characterization.

5.2 System Co–Ni

Electrodeposition of Co–Ni powders was performed in two types of ammonium hydroxide containing electrolytes: 1 M $(NH_4)_2SO_4$ + 0.7 M NH_4OH and 1 M NH_4Cl + 0.7 M NH_4OH. In sulfate containing electrolytes cobalt and nickel sulfates were used, while in chloride containing electrolytes cobalt and nickel chlorides were used as a source of Co^{2+} and Ni^{2+} ions [37–40]. The Co–Ni alloy powders were also electrodeposited from a solution containing 0.4 M H_3BO_3 + 0.2 M Na_2SO_4 and Ni and Co sulfate salts [41]. Three different Ni^{2+}/Co^{2+} concentration ratios were used: $Ni^{2+}/Co^{2+} = 1.00$ (0.01 M $NiSO_4$/0.01 M $CoSO_4$); $Ni^{2+}/Co^{2+} = 0.50$ (0.01 M $NiSO_4$/0.02 M $CoSO_4$); and $Ni^{2+}/Co^{2+} = 0.33$ (0.01 M $NiSO_4$/0.03 M $CoSO_4$). From this solution Co–Ni alloy powders were electrodeposited at a constant current density of approximately 70 mA cm^{-2}, corresponding to the cell voltage of about 5.0 V [41].

5.2.1 Polarization Curves for Co–Ni Alloy Powders Electrodeposition from Ammonium Sulfate–Ammonium Hydroxide Electrolyte

In Fig. 5.1 are shown polarization curves corrected for IR drop (see Chap. 2), for the processes of Co, Ni, and Co–Ni alloy powders electrodeposition from ammonium sulfate–ammonium hydroxide containing supporting electrolyte (1 M $(NH_4)_2SO_4$ + 0.7 M NH_4OH). As can be seen their shape is identical to that for pure Co, Fe, and Ni powders electrodeposition, characterized with two inflection points, A and B. For Co electrodeposition, sharp increase of current occurs at

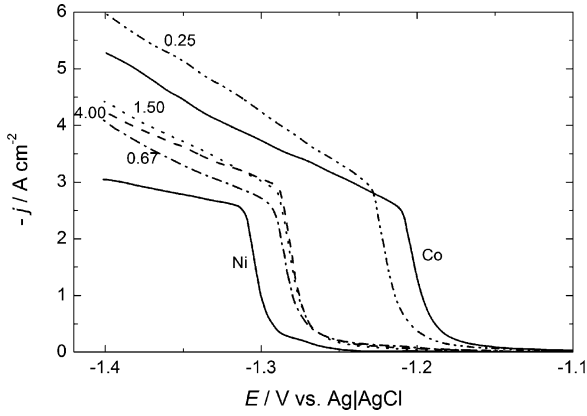

Fig. 5.1 Polarization curves for the electrodeposition of cobalt (Co), nickel (Ni), and Co–Ni alloy powders after IR drop correction recorded for different Ni^{2+}/Co^{2+} ions ratios: 4.00, 1.50, 0.67, and 0.25 (marked in the figure) (Reprinted from [40] with the permission of Elsevier.)

about −1.19 V, while for Ni electrodeposition this phenomenon is moved to more negative potentials (at about −1.30 V), indicating that the overvoltage for Ni electrodeposition in this solution is for about 0.1 V higher than that for Co electrodeposition, as it is the case for hydrogen evolution from pure supporting electrolytes (Fig. 2.24). In the case of alloy electrodeposition sharp increase of current density on the polarization curves recorded for Ni^{2+}/Co^{2+} ratios 4.00, 1.50, and 0.67 takes place at almost identical potentials, while the one for $Ni^{2+}/Co^{2+} = 0.25$ is moved to more positive potential, close to the polarization curve for pure Co.

Polarization curves corresponding only to the processes of electrodeposition of pure metals and alloy powders are shown in Fig. 5.2a, while corresponding η_j vs. E curves for alloy powders electrodeposition are presented in Fig. 5.2b.

As can be seen, significantly different polarization curves are obtained indicating different contribution of the hydrogen evolution current in all cases. It is quite interesting (Fig. 5.2a) that diffusion limiting current densities for Co and Ni are significantly different for the same cations concentration (0.1 M), $j_{l(Co)} = -0.76$ A cm^{-2} and $j_{l(Ni)} = -0.36$ A cm^{-2}. Taking into account these values, it is

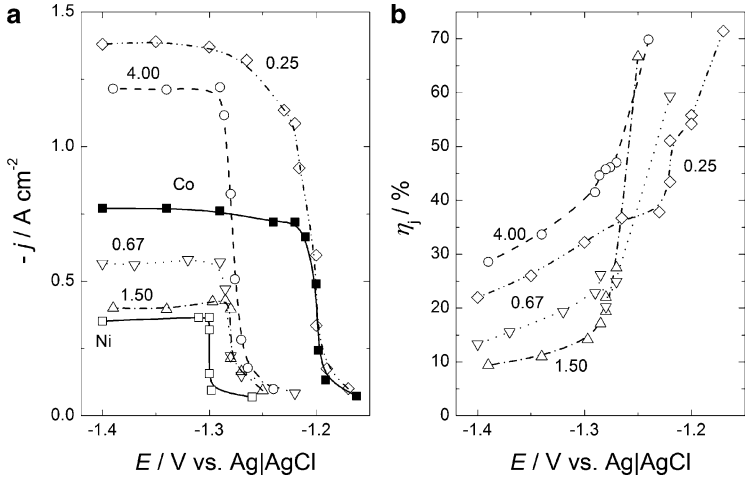

Fig. 5.2 (**a**) Polarization curves for the electrodeposition of cobalt (Co), nickel (Ni), and Co–Ni alloy powders (after subtraction of the current density for hydrogen evolution) recorded for different Ni^{2+}/Co^{2+} ions ratios: 4.00, 1.50, 0.67, and 0.25 (marked in the figure). (**b**) Corresponding current efficiency vs. potential curves for Co–Ni powders electrodeposition (Reprinted from [40] with the permission of Elsevier.)

obvious that at the same concentration of their ions the difference in their diffusion limiting current densities could be either due to different complexes that those metals may form with ammonia [124], or due to different metal electrodeposition process (difference in the contribution of hydrogen evolution current). Since both metals form the same number of complexes with ammonia (6 complexes) and their stability constants are very similar [124], it is most likely that the complex formation is not responsible for the observed difference in diffusion limiting current densities for Ni and Co. On the other side, hydrogen evolution current density in the case of Co electrodeposition is higher than that for Ni electrodeposition in the region of the diffusion limiting current, indicating that most likely this phenomenon could be ascribed to the increase of the real surface area during metal (powder) electrodeposition. It is important to note that it is quite difficult to make any convincing conclusion concerning this phenomenon, since there is no possibility to obtain the data about the increase

of the real surface area of the electrode during the processes of Co and Ni powders and Co–Ni alloy powders electrodeposition. If the increase of the real surface area is more pronounced during Co electrodeposition, the diffusion limiting current density could be lower and its value could be closer to the one obtained for Ni electrodeposition. According to the morphology of Co and Ni powders [37–40], it is most likely that the increase of the real surface area during the electrodeposition of Co is much higher than that for Ni electrodeposition.

It is interesting to note that the current density plateaus (diffusion limiting current densities) for the electrodeposition of Co–Ni alloys at the Ni^{2+}/Co^{2+} ratios 4.00 and 0.25 are higher than that for pure Co electrodeposition. The reason for such behavior is the fact that the total concentration of cations in these two solutions was not 0.1 M, since the compositions of these solutions were 0.1 M $NiSO_4$ + 0.025 M $CoSO_4$ + 1 M $(NH_4)_2SO_4$ + 0.7 M NH_4OH; 0.025 M $NiSO_4$ + 0.1 M $CoSO_4$ + 1 M $(NH_4)_2SO_4$ + 0.7 M NH_4OH (total concentration of cations 0.125 M). At the same time, the current efficiency for Co–Ni powder electrodeposition is the highest in these two solutions. Such behavior is most probably the consequence of the independence of the current density for hydrogen evolution on the total concentration of cations, so that the same curve for hydrogen evolution is subtracted from the higher values of j_{tot} (see Fig. 5.2a).

5.2.2 *Polarization Curves for Co–Ni Alloy Powders Electrodeposition from Ammonium Chloride–Ammonium Hydroxide Electrolyte*

The polarization curves corrected for IR drop for the processes of pure cobalt (Co), pure nickel (Ni), and Co–Ni alloy (powders) electrodeposition from ammonium chloride–ammonium hydroxide containing supporting electrolyte are presented in Fig. 5.3 (in this case the total concentration of cations in all investigated solutions was 0.1 M). As can be seen, cobalt electrodeposition (Co) commences at about −1.1 V, while sharp increase of current density (massive Co

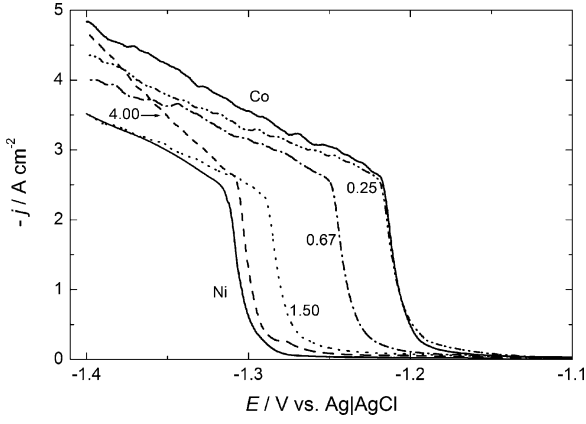

Fig. 5.3 Polarization curves for the electrodeposition of cobalt (Co), nickel (Ni), and Co–Ni alloy powders after IR drop correction recorded for different Ni^{2+}/Co^{2+} ions ratios: 4.00, 1.50, 0.67, and 0.25 (marked in the figure)

electrodeposition and hydrogen evolution) occurs at about −1.19 V. In the case of nickel electrodeposition (Ni), sharp increase of current density is moved to more negative potentials (at about −1.30 V), indicating that the overvoltage for massive Ni electrodeposition (and hydrogen evolution) in this solution is for about 0.1 V higher than that for Co electrodeposition, as it is the case for hydrogen evolution from pure supporting electrolytes (see Fig. 2.24, Chap. 2). In the case of Co–Ni alloy powders electrodeposition, polarization curves recorded for all Ni^{2+}/Co^{2+} ratios are placed between the polarization curves for pure Co and pure Ni.

Polarization curves corresponding only to the processes of electrodeposition of pure metals and alloy powders are shown in Fig. 5.4a, while corresponding η_j vs. E curves for pure metals and alloy powders electrodeposition are presented in Fig. 5.4b, respectively.

As in the case of sulfate supporting electrolyte (Fig. 5.2a), "diffusion limiting current density" (in this case not represented with the plateau) for Co is higher than that for Ni (Fig. 5.4a). At the same time, all polarization curves for Co–Ni alloy powders electrodeposition are characterized with higher values of current densities, indicating more efficient process of powders formation in the chloride

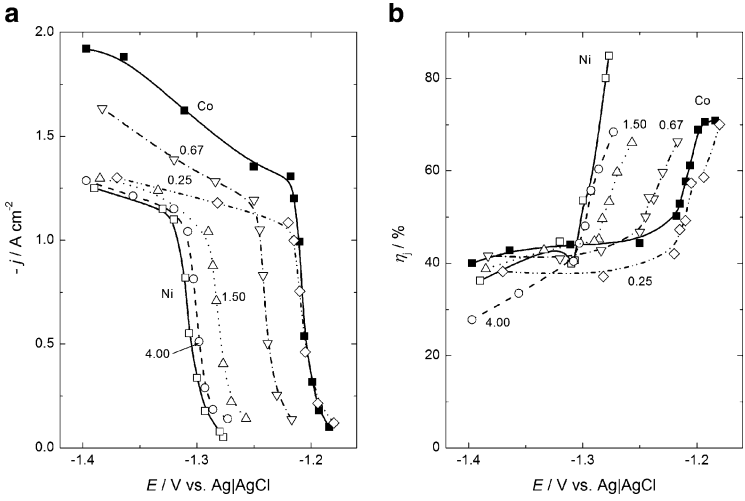

Fig. 5.4 (**a**) Polarization curves for the electrodeposition of cobalt (Co), nickel (Ni), and Co–Ni alloy powders (after subtraction of the current density for hydrogen evolution) recorded for different Ni^{2+}/Co^{2+} ions ratios: 4.00, 1.50, 0.67, and 0.25 (marked in the figure). (**b**) Corresponding current efficiency vs. potential curves for cobalt (Co), nickel (Ni), and Co–Ni powders electrodeposition (Reprinted from [39] with the permission of Elsevier.)

supporting electrolyte. This statement is supported with the η_j vs. E curves presented in Fig. 5.4b, where the current efficiency for powders electrodeposition is much higher than that in the sulfate supporting electrolyte (Fig. 5.2b).

5.2.3 *Chemical Compositions of the Co–Ni Alloy Powders*

All powder samples for chemical analysis, phase composition analysis, and morphology investigations were electrodeposited at the room temperature in the cylindrical glass cell of the total volume of 1 dm^3 with cone-shaped bottom of the cell to collect powder particles in it. Working electrode was a glassy carbon rod of the diameter of 5 mm with a total surface area of 7.5 cm^2 immersed in the

solution and placed in the middle of the cell. Cylindrical Pt–Ti mesh placed close to the cell walls was used as a counter electrode providing excellent current distribution in the cell.

In all cases certain small amount of disperse deposit remained on the glassy carbon electrode, while only powder particles that were detached from the electrode surface and collected at the cone-shaped bottom of the cell were analyzed.

Chemical composition of all electrodeposited Co–Ni alloy powders was determined by the AAS technique after dissolving certain amount of powders in HCl. The compositions of powders electrodeposited from sulfate and chloride containing supporting electrolytes were different.

5.2.3.1 Chemical Compositions of the Co–Ni Alloy Powders Electrodeposited from Ammonium Sulfate–Ammonium Hydroxide Electrolyte

The dependence of atomic percentages of both metals as a function of Ni^{2+}/Co^{2+} ratio is presented in Fig. 5.5a. As it could be expected, the content of Ni increases, while the content of Co decreases with the increase of the Ni^{2+}/Co^{2+} ratio.

It is well known that the electrodeposition of compact deposits of Co–Ni alloys belongs to the type of anomalous codeposition according to Brenner's classification [116]. The influence of the electrolyte composition on the alloy powder composition is shown in Fig. 5.5a, b. As can be seen in Fig. 5.5a, the content of Ni increases by increasing the ratio of Ni^{2+}/Co^{2+} ions, while the content of Co decreases and both dependences are approximately linear after sharp increase (decrease) at low values of Ni^{2+}/Co^{2+}. According to Brenner's classification [116], the behavior presented in Fig. 5.5b indicates two types of powder codeposition: irregular, up to about 60 at.% of Ni (or 40 at.% of Co) in the solution and anomalous at higher amounts of Ni. The irregular codeposition is expected to occur in systems in which the static potentials of the parent metals are close together and with metals that form solid solution. Both conditions are fulfilled for the system Co–Ni [116]. The characteristic of anomalous codeposition is that it occurs only under certain conditions of concentration and operating variables for a given plating bath [116]. Hence, if the deposition of the more noble metal is so strongly

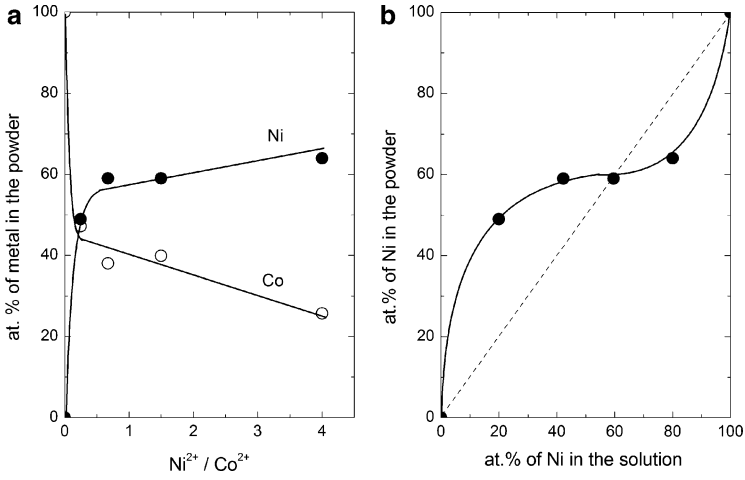

Fig. 5.5 (**a**) Composition of powders as a function of the Ni^{2+}/Co^{2+} ions ratio. (**b**) Corresponding diagram according to Brenner's classification [116] (Reprinted from [38] with the permission of Springer-Verlag.)

inhibited that no current can be recorded as the potential is driven negative, at some potential the less noble metal would start depositing causing the increase of deposition current. At some more negative potential a breakthrough in the deposition of the more noble metal may happen as a result of reduction or removal of the additive or by opening some alternative mechanism of discharge, not operative at less negative potential. Such a case is found in the deposition of Ni–Zn alloys and is explained by "the hydroxide suppression mechanism" [125, 126]. It has already been shown that from simple salt containing electrolytes codeposition of Co and Ni possesses anomalous character [116, 127–129], as well as in the electrolytes containing metal complexes [130], but in all cases compact deposits were obtained. As can be seen in Fig. 5.5b, at the conditions of powder electrodeposition where both components deposit at their diffusion limiting current densities, irregular and/or anomalous character of Co–Ni alloy deposition is achieved, depending on the solution composition.

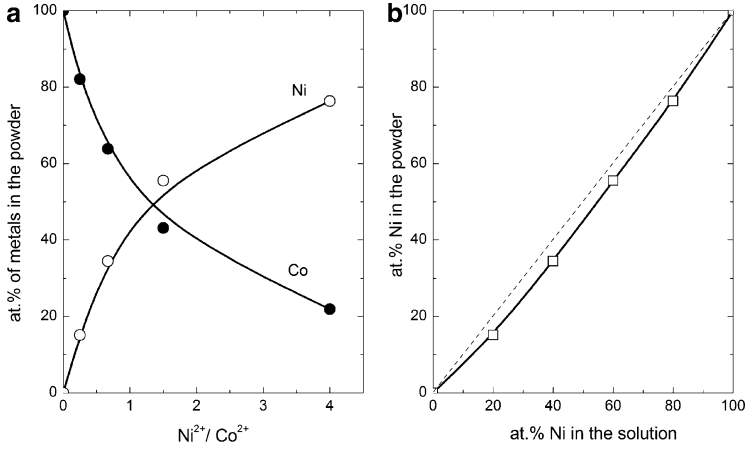

Fig. 5.6 (**a**) Composition of powders as a function of the Ni^{2+}/Co^{2+} ions ratio. (**b**) Corresponding diagram according to Brenner's classification [116] (Reprinted from [39] with the permission of Elsevier.)

5.2.3.2 Chemical Compositions of the Co–Ni Alloy Powders Electrodeposited from Ammonium Chloride–Ammonium Hydroxide Electrolyte

The same dependences as in Fig. 5.5 are presented in Fig. 5.6 for chloride containing supporting electrolyte. In this case anomalous codeposition is obtained for all Co–Ni alloy powders compositions, with the more noble metal electrodeposition (Ni) being suppressed by the presence of the less noble metal (Co) in the solution, i.e., less noble metal is more readily deposited.

5.2.3.3 Chemical Compositions of the Co–Ni Alloy Powders Electrodeposited from Borate–Sulfate Electrolyte

The polarization curves for this system showed that the current efficiency for Co–Ni powder formation is very low, about 1–2%.

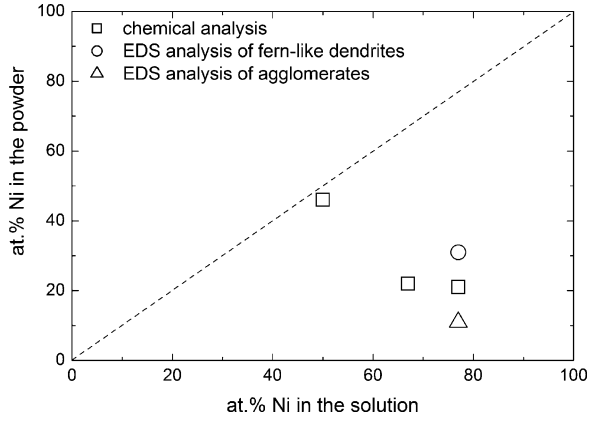

Fig. 5.7 Diagram corresponding to Brenner's classification for the Co–Ni powders electrodeposited from borate–sulfate containing electrolyte (results of chemical analysis—*open squares*, result of EDS analysis—*open triangle*—agglomerates, *open circle*—fern like dendrites)

In this case longer time for powders deposition was needed in order to obtain sufficient amount of powder to be analyzed [41].

In Fig. 5.7 is shown diagram corresponding to Brenner's classification for this system. Since the morphology of electrodeposited powders was different for different values of the Ni^{2+}/Co^{2+} ratios (see Figs. 5.18–5.20), composition of all powders was determined by the chemical analysis (□), while the powder with the highest amount of cobalt ($Ni^{2+}/Co^{2+} = 0.33$) was analyzed by the EDS analysis too. According to the results presented in Fig. 5.7, anomalous codeposition is characteristic for all investigated solutions, being more pronounced for lower values of Ni^{2+}/Co^{2+} ratios. As can be seen in Fig. 5.7, the composition of agglomerates (see Fig. 5.20a) showed lower content of Ni (△), while the composition of fern-like dendrites (see Figs. 5.18a, b, 5.19a, and 5.20b) showed higher content of Ni (○) in comparison with the results of chemical analysis (□). The average value of the EDS analysis for both morphologies was identical to the chemical composition analysis.

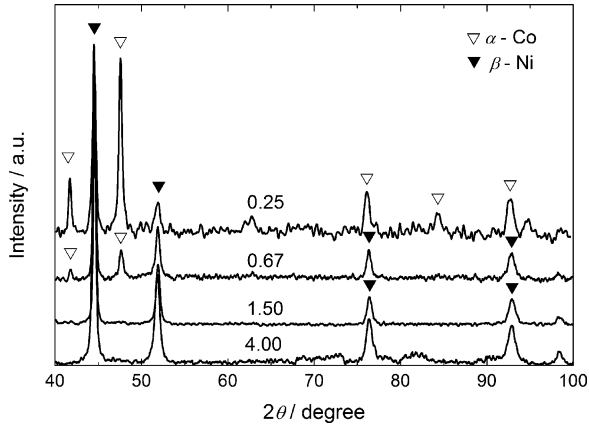

Fig. 5.8 Diffractograms of the Co–Ni powders electrodeposited from the solutions of different Ni^{2+}/Co^{2+} ions ratios (marked in the figure). The phase composition was identical for powders electrodeposited from sulfate and chloride supporting electrolytes (Reprinted from [38] with the permission of Springer-Verlag.)

5.2.4 *Phase Compositions of the Co–Ni Alloy Powders*

The phase composition of all alloy powder samples was determined by the X-ray technique. The X-ray diffraction patterns of all four samples electrodeposited from ammonium hydroxide containing solutions are shown in Fig. 5.8.

As can be seen, XRD patterns contain the characteristic peaks for Ni-based solid solution (Ni-rich phase, β-Ni phase) (▼) with face-centered cubic lattice (f.c.c., space group Fm3m) and h.c.p. α-Co phase (▽). It is seen in Fig. 5.8 that with the decrease of Ni^{2+}/Co^{2+} ions ratio peaks for β-Ni phase (▼) become smaller and some of them disappear, while the peaks for h.c.p. α-Co phase (▽) become more pronounced. For samples electrodeposited from the solutions containing higher concentration of Ni^{2+} ions than Co^{2+} ions ($Ni^{2+}/Co^{2+} = 4.00$ and 1.50) only the presence of β-Ni phase (▼) was detected, while at concentration ratios $Ni^{2+}/Co^{2+} < 1$ h.c.p. α-Co phase (▽) together with

Table 5.1 Crystallite size of phases detected in the Co–Ni powders

Ni^{2+}/Co^{2+}	β-Ni phase (nm)	α-Co phase (nm)
4.00	24	
1.50	28	
0.67	31	17
0.25	30	16

Reprinted from [38] with the permission of Springer-Verlag

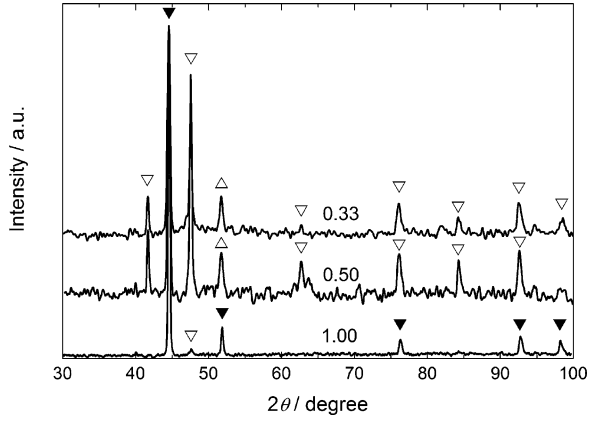

Fig. 5.9 Diffractograms of the Co–Ni powders electrodeposited from the solutions of different Ni^{2+}/Co^{2+} ions ratios (marked in the figure) from the borate–sulfate containing solutions (β-Ni phase—*inverted filled triangle*, α-Co phase—*inverted open triangle*, f.c.c. Co phase—*open triangle*)

β-Ni phase (▼) was detected in the alloy powder deposit. The dimensions of crystallites for both phases were determined from the diffractograms presented in Fig. 5.8 using Scherrer formula [131]. The results are presented in Table 5.1.

The X-ray diffraction patterns of three samples electrodeposited from borate–sulfate containing solutions are shown in Fig. 5.9.

The XRD patterns contain the characteristic peaks for Ni-based solid solution (Ni-rich phase, β-Ni phase) (▼) with face-centered cubic lattice (f.c.c., space group Fm3m) and h.c.p. α-Co phase (▽). It is seen in Fig. 5.9 that with the decrease of Ni^{2+}/Co^{2+} ions ratio peaks for β-Ni

phase (▼) become smaller and some of them disappear, while the peaks for h.c.p. α-Co phase (▽) become more pronounced and f.c.c. Co phase (△) becomes visible (0.50 and 0.33). According to the literature [132], the f.c.c. Co phase could be expected at temperatures higher than 450°C, while in the case of alloy powder electrodeposition this structure has been formed at the room temperature, indicating that during the process of alloy powder electrodeposition the conditions for the formation of this phase are fulfilled and that in the case of alloy powder electrodeposition the data available in the literature for equilibrium conditions of corresponding alloy formation [132] are not fully reliable.

5.2.5 *The Morphology of the Co–Ni Alloy Powders*

The morphology of pure Co and pure Ni powders electrodeposited from ammonium sulfate or ammonium chloride supporting electrolytes, as well as the mechanism of powder agglomerates formation, has been discussed in Chap. 2. The mechanism of alloy powders formation is practically the same as that of pure metal powders. The morphology was found to depend mainly on the Ni^{2+}/Co^{2+} ions ratio (i.e., the composition of the alloy powders) and to some extent on the presence of sulfate or chloride anions, or borate.

5.2.5.1 The Morphology of the Co–Ni Alloy Powders Electrodeposited from the Sulfate Containing Supporting Electrolyte

The morphology of the Co–Ni alloy powders electrodeposited at the current density $j = 0.5$ A cm^{-2} from the electrolytes containing different Ni^{2+}/Co^{2+} ions ratio is shown in Figs. 5.10–5.13. As can be seen, the morphology of Co–Ni alloy powder is sensitive to the Ni^{2+}/Co^{2+} ions ratio, i.e., to the composition of the alloy powder.

In the powder containing the highest amount of Ni, of about 64 wt.% Ni, electrodeposited at the $Ni^{2+}/Co^{2+} = 4.00$, more than 90% of agglomerates were typical spongy agglomerates varying in

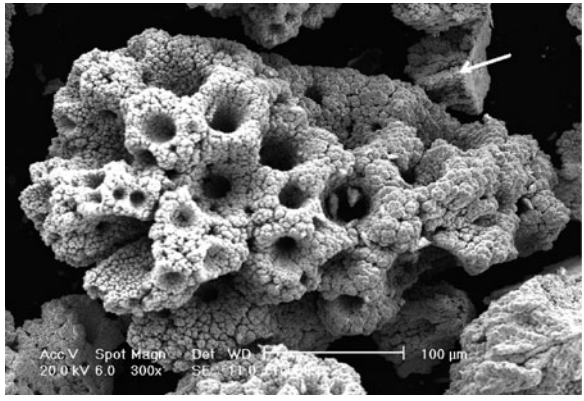

Fig. 5.10 Typical powder agglomerate detected in the powder electrodeposited at the $Ni^{2+}/Co^{2+} = 4.00$ (Reprinted from [38] with the permission of Springer-Verlag.)

size from about 50 μm to about 200 μm, shown in Fig. 5.10. Very few cauliflower-like agglomerates of slightly different shape than those typical for pure Ni powder were also detected in the alloy powder. One such particle is marked with the arrow in the upper right corner of Fig. 5.10. It is important to note that this particle has a flat surface on one side, indicating that this type of growth belongs to the beginning of the powder formation with this particle falling off from the electrode surface before a bigger, typical spongy agglomerate is formed. Spongy agglomerates are more similar to the ones detected in pure Co powder, with the presence of large number of cavities, but contrary to the situation in the case of pure Co powder, here practically none of the cavities possess fern-like dendrites on their bottom, indicating that most of the agglomerates detached from the electrode surface before the hydrogen bubble in the cavity was liberated. It is interesting that practically no dendrites are found in this powder, although about 26 wt.% of Co is present in the powder.

As the Ni^{2+}/Co^{2+} ions ratio in the electrolyte decreases from 4.00 to 1.50, the composition of the Co–Ni alloy powder changes from about 78 at.% Ni—22 at.% Co to about 56 at.% Ni—44 at.% Co (Fig. 5.5) and this change influences the morphology of the powder. All powder agglomerates electrodeposited at $Ni^{2+}/Co^{2+} = 1.50$ are

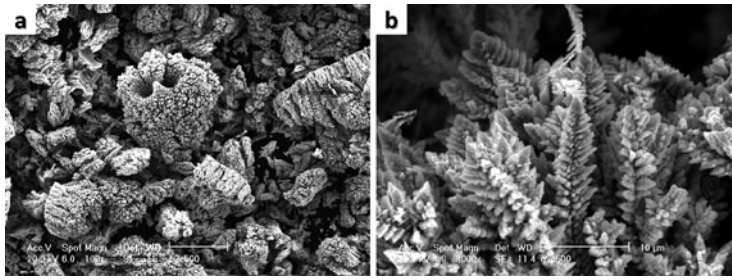

Fig. 5.11 Typical powder agglomerates detected in the powder electrodeposited at the $Ni^{2+}/Co^{2+} = 1.50$ (Reprinted from [38] with the permission of Springer-Verlag.)

covered with the fern-like dendrites (Fig. 5.11b). Only a few agglomerates are bigger (about 200 μm) and the number of cavities observed on them is significantly reduced (Fig. 5.11a) in comparison with the one obtained at the ratio $Ni^{2+}/Co^{2+} = 4.00$. As can be seen in Fig. 5.11a, significant number of dendritic agglomerates is detected in this powder deposit (around the agglomerate). Very few spongy-like agglomerates of the size of about 500 μm are also present in the powder and they are also covered with the fern-like dendrites, indicating that in the presence of higher amount of Co in the powder dendritic growth prevails. With further decrease of the Ni^{2+}/Co^{2+} ions ratio (0.67) in the electrolyte, the composition of the Co–Ni alloy powder changes towards lower content of Ni (Fig. 5.5) and the morphology of powder agglomerates is slightly different. In this case the number of agglomerates increases in comparison with the ratio $Ni^{2+}/Co^{2+} = 1.50$, with the shape of agglomerates being different, as can be seen in Fig. 5.12a–c. The common characteristic of all agglomerates obtained at $Ni^{2+}/Co^{2+} = 0.67$ is that they are covered with the fern-like dendrites. At the same time, higher amount of dendritic particles (around the agglomerate shown in Fig. 5.12b) is formed during Co–Ni powder electrodeposition. The size of dendrite particles vary from about 5 μm to about 50 μm.

In the Co–Ni alloy powder deposit with the highest percentage of Co (85 at.%), Fig. 5.13, different types of agglomerates could be detected (1) spongy-like agglomerates of the size of about 500 μm

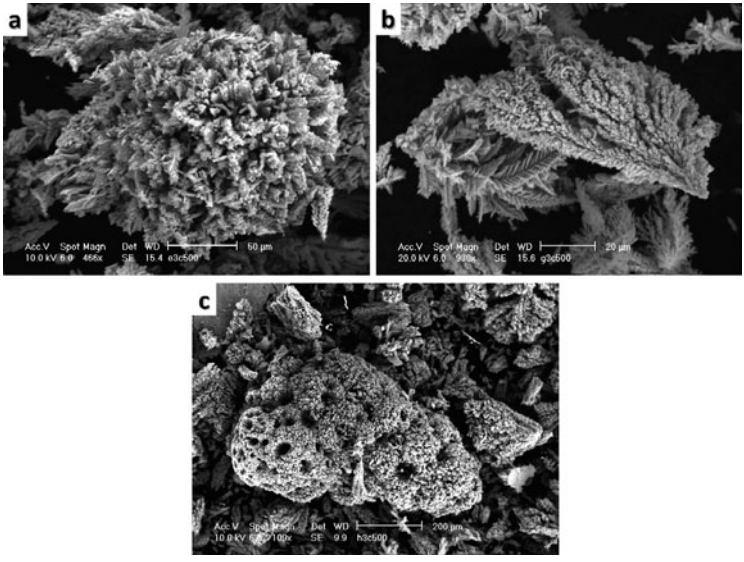

Fig. 5.12 Typical powder agglomerates detected in the powder electrodeposited at the $Ni^{2+}/Co^{2+} = 0.67$ (Reprinted from [38] with the permission of Springer-Verlag.)

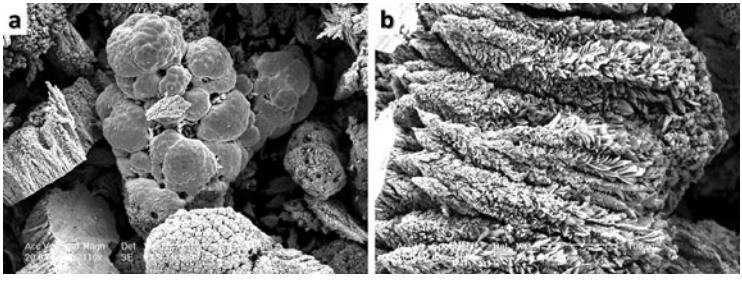

Fig. 5.13 Typical powder agglomerates detected in the powder electrodeposited at the $Ni^{2+}/Co^{2+} = 0.25$ (Reprinted from [38] with the permission of Springer-Verlag.)

covered with the fern-like dendrites, also found in the powder obtained at $Ni^{2+}/Co^{2+} = 0.67$ (Fig. 5.12c); (2) compact agglomerates, characteristic for pure Co powder deposit (Fig. 5.13a); and (3) agglomerates composed of closely packed fern-like dendrites about 200 μm long (Fig. 5.13b). By the EDS analysis of the compact agglomerate, shown in Fig. 5.13a, it is found that it does not represent pure Co particle, but the Co–Ni alloy of almost identical composition as the rest of the powder, indicating that the formation of alloy agglomerates follows a growth mechanism for Co powder formation.

Considering all detected types of agglomerates in electrodeposited Co–Ni alloy powders of different compositions, one can conclude that only one powder (with 78 at.% of Ni) contains very small amount of cauliflower-like agglomerates typical for pure Ni powder, but slightly different, while the rest of them contain some of the agglomerates detected in pure Co powder. The difference between the agglomerates detected in pure Co powder and in Co–Ni alloy powder (except for the agglomerates obtained from the electrolyte with the highest Ni^{2+}/Co^{2+} ions ratio, Fig. 5.11) is the presence of fern-like dendrites on the surface of these agglomerates. Such a behavior indicates that for these three alloy compositions the presence of Ni^{2+} and Co^{2+} ions promotes dendrite formation on the surface of all agglomerates detected in Co–Ni alloy powders. Hence, it appears that although some similarities between the type of agglomerates detected in pure Co and Co–Ni alloy powders exists, it is practically not possible to strictly correlate composition of alloy powders with their morphology.

To explain the difference in the morphology as a function of alloy composition (Ni^{2+}/Co^{2+} ions ratio), one should refer to the polarization curves presented in Fig. 5.2a. As can be seen in the figure, at the applied current density of -0.5 A cm^{-2} only one alloy, electrodeposited at the $Ni^{2+}/Co^{2+} = 1.50$, deposits at its diffusion limiting current density. The one electrodeposited at the $Ni^{2+}/Co^{2+} = 0.67$ deposits at a slightly lower current density than its diffusion limiting current density, while for the alloys electrodeposited at $Ni^{2+}/Co^{2+} = 4.00$ and 0.25 the applied current density lies in the region of mixed control of deposition, being much less than the diffusion limiting current density for those electrolyte compositions. Bearing in mind that the currents presented in this figure represent only 20% of the total

current and that massive hydrogen evolution takes place together with the process of alloy electrodeposition, it is quite difficult to find good explanation for the phenomena observed. Different theories concerning powder formation during metal electrodeposition exist in the literature [133] with one of them claiming that powder formation takes place at the diffusion limiting current at potentials of hydrogen evolution, which is necessary process for powder formation. In the case of Co–Ni alloy powder electrodeposition hydrogen evolution commences already at the beginning of the electrodeposition process, being catalyzed by the electrodeposition. Hence, any comparison between these two processes is not realistic, but it is obvious that hydrogen evolution plays an important role in the process of powder electrodeposition.

5.2.5.2 The Morphology of the Co–Ni Alloy Powders Electrodeposited from the Chloride Containing Supporting Electrolyte

In Figs. 5.14–5.17 are shown SEMs of Co–Ni alloy powders obtained from a solution containing different Ni^{2+}/Co^{2+} ions ratios. At the Ni^{2+}/Co^{2+} ions ratio of 4.00, Fig. 5.14, two types of agglomerates are detected: cauliflower ones (a), varying in size between 60 and 100 μm, and bigger (varying in size between 200 and 400 μm), spongy ones (b), similar to the morphology of pure Ni powder. In the case of alloy, these two types of agglomerates are not equally distributed, but most of the agglomerates (over 80%) are spongy-like agglomerates.

With increasing the content of Co^{2+} ions in the solution, as well as in the powder (Ni^{2+}/Co^{2+} ions ratio of 1.50), very few cauliflower-like agglomerates can be detected in the powder deposit (Fig. 5.15a), being of the size of about 100 μm, while most of them are spongy-like ones of a bigger size of about 200 μm (Fig. 5.15b). It is characteristic for spongy agglomerates that two types of cavities could be detected on all powder agglomerates: narrow (cylindrical) cavities with fern-like dendrites formed at their bottom (Fig. 5.15c), indicating that before agglomerates detached from the electrode surface conditions of planar diffusion in the cavity were established causing formation of fern-like dendrites and wider, cone-shaped cavities without fern-like dendrites on their bottom (Fig. 5.15a, b). It is most likely that the

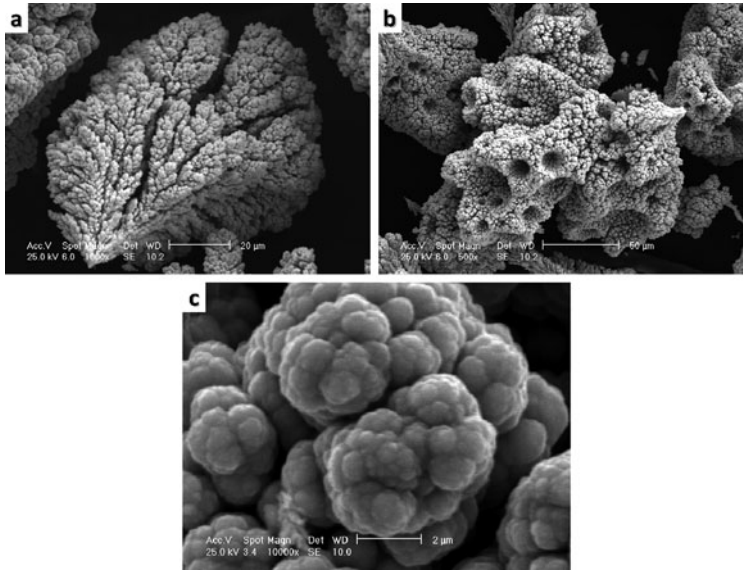

Fig. 5.14 Typical agglomerates detected in the powder electrodeposited at the $Ni^{2+}/Co^{2+} = 4.00$ (Reprinted from [39] with the permission of Elsevier.)

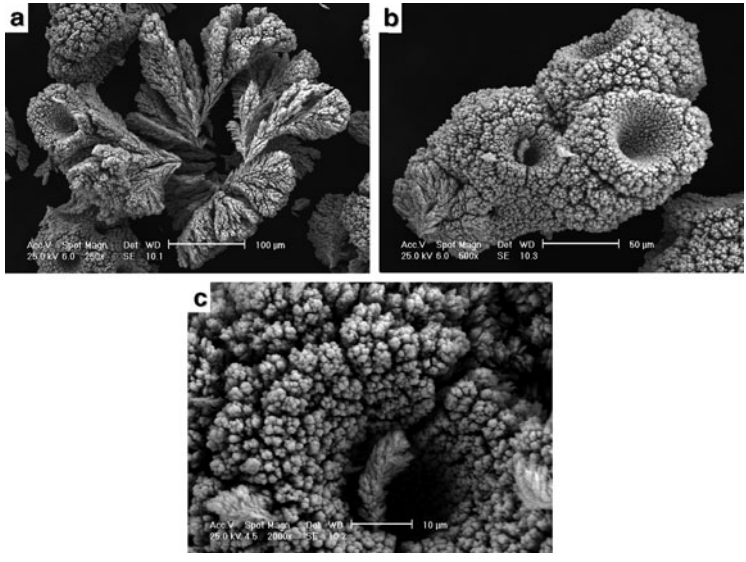

Fig. 5.15 Typical powder agglomerates detected in the powder electrodeposited at the $Ni^{2+}/Co^{2+} = 1.50$ (Reprinted from [39] with the permission of Elsevier.)

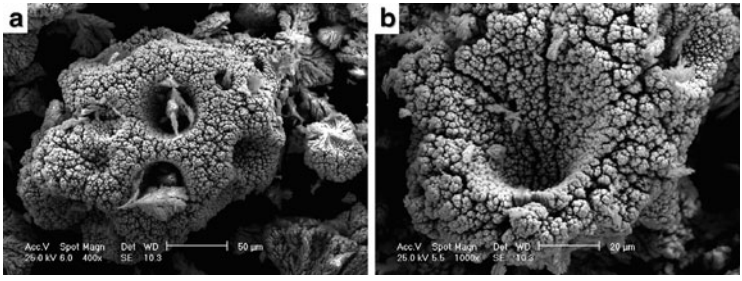

Fig. 5.16 Typical powder agglomerates detected in the powder electrodeposited at the $Ni^{2+}/Co^{2+} = 0.67$ (Reprinted from [39] with the permission of Elsevier.)

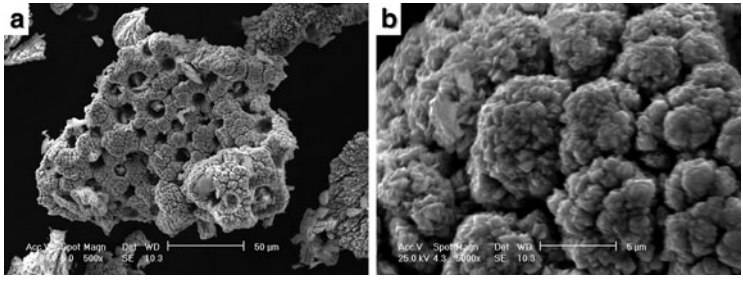

Fig. 5.17 Typical powder agglomerates detected in the powder electrodeposited at the $Ni^{2+}/Co^{2+} = 0.25$ (Reprinted from [39] with the permission of Elsevier.)

absence of fern-like dendrites at the bottom of cone-shaped cavities is the consequence of the fact that because of such a shape, with wide opening, no condition for planar diffusion in these cavities was established.

With further decrease of Ni^{2+}/Co^{2+} ions ratio to 0.67 no cauliflower-like agglomerates are detected. All agglomerates are spongy-like, again with two types of cavities: narrow (cylindrical) ones with fern-like dendrites on their bottom (Fig. 5.16a) and cone-shaped ones (Fig. 5.16b) without fern-like dendrites on their bottom. The top surface of all agglomerates obtained from these three solutions is practically identical, being characterized by cauliflower nature, as shown in Fig. 5.14c.

At the lowest Ni^{2+}/Co^{2+} ions ratio of 0.25 the same types of spongy agglomerates as ones obtained from the solution containing Ni^{2+}/Co^{2+} ions ratio of 0.67 are obtained, Fig. 5.17a. In this case two types of spongy agglomerates, concerning the top surface of the agglomerates, are detected: agglomerates with flat noodle-like endings, Fig. 5.14c, and agglomerates with the presence of well-defined crystals on the cauliflower endings, as shown in Fig. 5.17b. It is most likely that the detachment of agglomerates shown in Fig. 5.17b occurred later than the detachment of agglomerates shown in Fig. 5.14c, allowing the formation of a second layer of their growth to take place. Hence, in comparison with pure metal powders, agglomerates of alloy powders are characterized by the presence of two types of cavities: cylindrical ones with the fern-like dendrites on their bottom, indicating that hydrogen bubbles are liberated before the powder agglomerates detachment, and cone-shaped ones without fern-like dendrites on their bottom (because of the cavity shape planar diffusion cannot be established in the cavity), detected at smaller powder agglomerates. The appearance of such cavity is most probably due to different (higher) rate of hydrogen bubble formation in this solution. Comparing results obtained in chloride containing electrolyte with the results obtained in sulfate containing electrolyte, the following remarks could be made (1) polarization curves for hydrogen evolution in supporting electrolytes are different, with the one recorded in the chloride containing supporting electrolyte being characterized with higher current densities, indicating faster hydrogen evolution in the presence of smaller anions (see Fig. 2.24); (2) correct polarization curves for pure metals and alloy powders electrodeposition are also characterized with higher current densities, as well as higher current efficiencies for powder electrodeposition, indicating faster and easier powder formation in chloride containing electrolyte; (3) relatively similar morphologies of powder agglomerates are detected in both solutions, with the distribution of agglomerates being different in all cases. The characteristic feature of powder agglomerates obtained from chloride containing electrolytes is the presence of cone-shaped cavities.

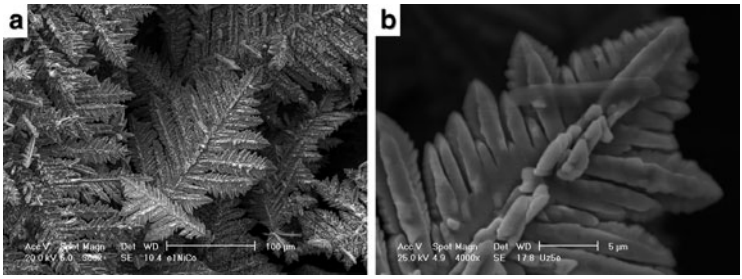

Fig. 5.18 Typical powder particles detected in the powder electrodeposited at the $Ni^{2+}/Co^{2+} = 1.00$

5.2.5.3 The Morphology of the Co–Ni Alloy Powders Electrodeposited from the Borate–Sulfate Containing Supporting Electrolyte [41]

At the highest Ni^{2+}/Co^{2+} ions ratio in the solution all powder agglomerates possess 2D fern-like shape, varying in the size from about 100 μm to about 200 μm, as can be seen in Fig. 5.18. They are all practically two dimensional (Fig. 5.18a), although at higher magnification (Fig. 5.18b) it can be seen that a third dimension of their growth also exists, but it seems that this is practically a two-dimensional layer-by-layer growth following original dendrite shape. It can also be seen that on the main branch of such dendrite small dendritic agglomerates, growing in the direction normal to the layer-by-layer growth, could be detected, Fig. 5.18b.

With the decrease of the Ni^{2+}/Co^{2+} ions ratio in the solution (0.50), i.e., the increase of the Co content in the alloy powder, among 2D fern-like agglomerates of a smaller size than in a previous case (varying in size between 50 and 100 μm—Fig. 5.19a), agglomerates of the size of about 100 μm composed of a densely packed dendritic agglomerates were detected, as can be seen in Fig. 5.19b. It is interesting to note that dendrites covering the surface of such agglomerates are not 2D fern-like type. As can be seen in Fig. 5.19c, they are branching in four directions, but they are more compact and branches are much smaller, as are the dendrites (about 10 μm long and about 2 μm wide).

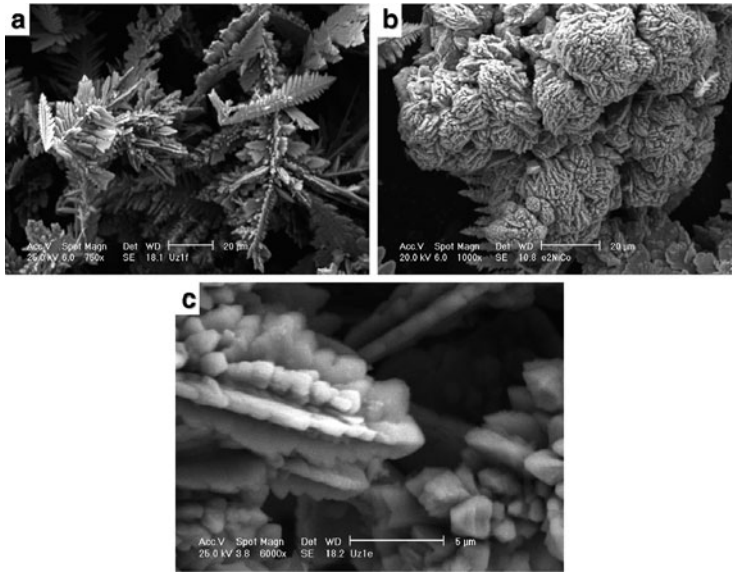

Fig. 5.19 Typical powder particles and agglomerates detected in the powder electrodeposited at the $Ni^{2+}/Co^{2+} = 0.50$

With further decrease of the Ni^{2+}/Co^{2+} ions ratio in the solution (0.33), compact agglomerates, typical for pure Co powder, could be clearly detected in the powder deposit, as can be seen in Fig. 5.20a, together with the 2D fern-like dendrites. By the EDS analysis of compact agglomerates it was confirmed that they do not represent pure Co particle, but the Co–Ni alloy, indicating that similar shapes of agglomerates characterize pure Co and Co–Ni alloy powder deposit. The presence of densely packed 3D dendritic agglomerates can also be seen in this powder, as shown in Fig. 5.20b. Again, these dendrites are more compact and smaller than those recorded on powder agglomerates electrodeposited at the Ni^{2+}/Co^{2+} ions ratio 0.50.

It is noteworthy that with the increase of the h.c.p. α-Co (100) phase in the powder deposit (Fig. 5.9) and the decrease of the f.c.c. β-Ni (111) phase, the shape of dendrite agglomerates changes from typical 2D fern-like dendrites to 3D dendrites. This is in accordance with the statement [134] that in the presence of the (111) orientation

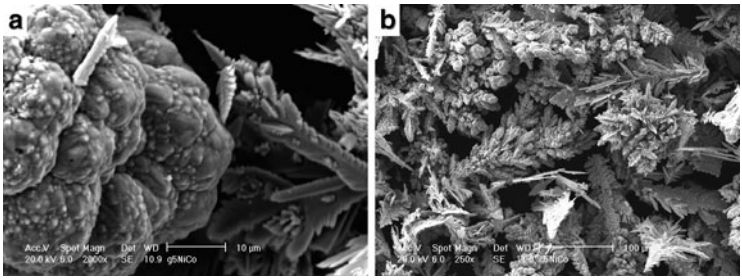

Fig. 5.20 Typical powder particles and agglomerates detected in the powder electrodeposited at the $Ni^{2+}/Co^{2+} = 0.33$

(f.c.c. β-Ni (111) phase) 2D dendrite growth prevails (the highest intensity for f.c.c. β-Ni (111) phase is detected in sample 1.00, Fig. 5.9). Such dendrites are denoted in the literature [134] as 2D {100}60°, with the angle of 60° between the main tree of the dendrite and the branches. To explain the influence of other orientations (h.c.p. α-Co (100) etc.) on the growth of dendrites in the investigated powder and appearance of 3D dendrites in the powder deposit, additional experiments and more detailed analysis are needed.

It should be emphasized here that the morphology of Co–Ni powders presented in the paper of El-Halim et al. [35] is completely different than the one presented in this chapter. This difference is most probably the consequence of the fact that in our work only powder agglomerates detached from the electrode surface were analyzed by the SEM, while in the paper of El-Halim et al. [35] disperse deposit still on the electrode surface was investigated.

5.3 System Fe–Ni

Electrodeposition of Fe–Ni powders was performed in ammonium chloride–sodium citrate containing electrolyte of the composition 1 M NH_4Cl + 0.2 M $Na_3C_6H_5O_7$. Iron(III) and iron(II) chloride and

nickel chloride were used as a sources of Fe^{3+} or Fe^{2+} and Ni^{2+} ions. The total concentration of cations was kept at 0.1 M. Four different Ni/Fe concentration ratios were investigated: Ni/Fe = 9/1; Ni/Fe = 3/1; and Ni/Fe = 1/1; Ni/Fe = 1/3. In the case of iron(III) ions pH of the solution was adjusted to 4.5, while in the case of iron(II) ions pH of the solution was adjusted to 4.0. All solutions were made from analytical grade purity chemicals and distilled water by the following procedure: $Na_3C_6H_5O_7$ was first dissolved and the pH was adjusted to slightly higher value than desired by HCl; in the next step metal (Fe(III), or Fe (II) or Ni) salts were dissolved; finally, ammonium chloride was added and pH adjusted to the exact value. Concerning the stability of solutions it is well known that during investigation some Fe(II) become oxidized into Fe(III). This should be particularly pronounced during the deposition of powders for 1 or 2 h. Taking into account that in all cases Fe(II) or Fe(III) made very stable complexes with citrate anions, we did not experience problems in the case of polarization measurements (polarization curves were practically the same after 3–4 measurements), but for any case before each experiment fresh solution was made and used for investigation as well as for powder electrodeposition.

It should be mentioned here that an attempt was made to deposit Fe–Ni powders from the electrolytes of the same composition but of low pH 2. The powder agglomerates were successfully produced on the cathode, but immediately after detaching from the cathode surface they started dissolving with gas evolution in all investigated electrolytes. Only in the case of very short time of electrolysis and removal of remained powder (which had not yet been dissolved) it was possible to obtain small amount of powder for further analysis. That was the reason why all experiments were performed in the solutions of pH 4.0 or 4.5, since in this solution powders were stable after deposition.

From all solutions Fe–Ni alloy powders were electrodeposited at a constant current density corresponding to the slightly lower value (j_{pd}) than the inflection point B [marked with (●)] on the polarization curves (see Fig. 5.21).

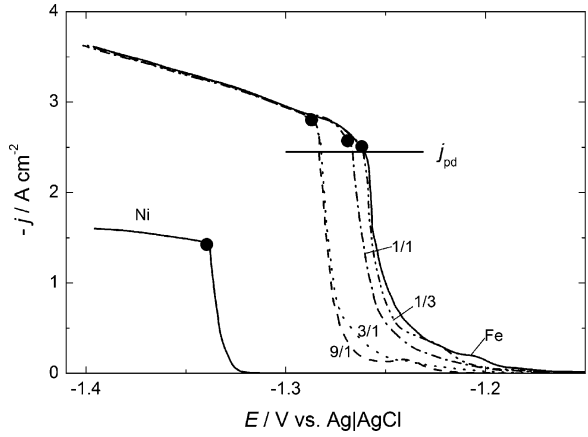

Fig. 5.21 Polarization curves for the electrodeposition of iron (Fe), nickel (Ni), and Fe–Ni alloy powders after IR drop correction recorded for different Ni/Fe ions ratios 9/1, 3/1, 1/1, and 1/3 (marked in the figure), in the solution of Fe(II) and Ni(II) species (Reprinted from [61] with the permission of Elsevier.)

5.3.1 Polarization Curves for Fe–Ni Alloy Powders Electrodeposition from Ammonium Chloride–Sodium Citrate Electrolyte

The polarization curves corrected for IR drop for the processes of Fe, Ni, and Fe–Ni alloy powders electrodeposition from ammonium chloride–sodium citrate containing supporting electrolyte in the presence of Fe(II) and Ni(II) species are shown in Fig. 5.21. In the case of Fe(II) salts polarization curve for iron electrodeposition (Fe) was placed at more positive potentials than that for nickel (Ni) as it is expected from the values of their reversible potentials. The polarization curves for Fe–Ni alloy powders electrodeposition are placed in between and all of them were placed at more positive potentials than expected from the Ni/Fe ratio, indicating anomalous codeposition.

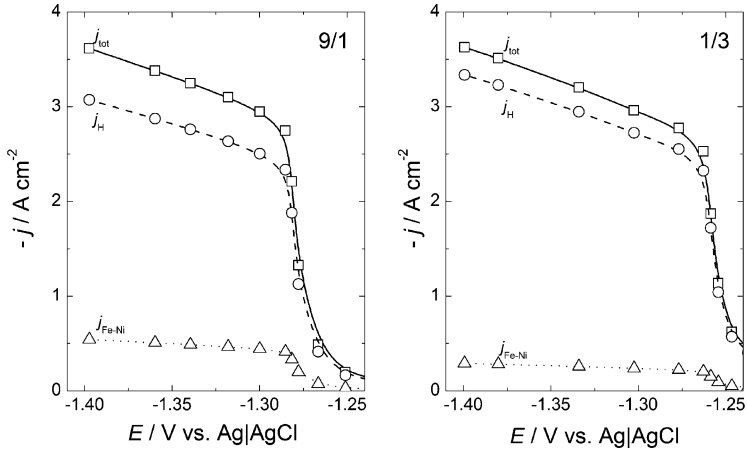

Fig. 5.22 Polarization curve for the Fe–Ni alloy powders electrodeposition (j_{tot}) (*open square*), polarization curve for hydrogen evolution (j_H) (*open circle*), and polarization curve for Fe–Ni powder electrodeposition after subtraction of hydrogen evolution current ($j_{Fe–Ni}$) (*open triangle*). The values of Ni/Fe ions ratios are marked in the figure (Reprinted from [61] with the permission of Elsevier.)

It was found that for the Fe(III) salts electrolytes the current efficiency was very low, 1–2% (the polarization curves for powder deposition (j_{tot}) and for hydrogen evolution (j_H) practically overlapped), and it was necessary to deposit powders at least for 2 h to obtain the amount of powder that could be used for the morphology and composition analysis (SEM, EDS). In the case of Fe(II) salt electrolytes, current efficiency at the potentials more negative than the second inflection point (● in Fig. 5.21) varied between 8% and 15% depending on the Ni/Fe ratio, as shown in Fig. 5.22. The average values for the diffusion limiting current densities for alloy powder electrodeposition were $j_{Fe–Ni} = -0.26$ A cm^{-2} for the ratio 1/3 and $j_{Fe–Ni} = -0.49$ A cm^{-2} for the ratio 9/1.

With the increase of iron concentration (as well as with the increase of the amount of iron in the powder—decrease of Ni/Fe ratio) the current efficiency for powder electrodeposition decreased, which is in accordance with the data obtained for compact Fe–Ni alloy deposits [135].

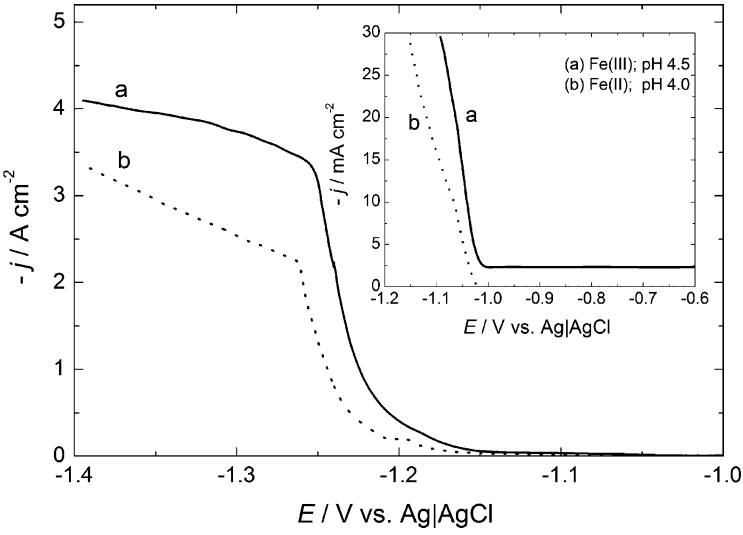

Fig. 5.23 The polarization curves for the electrodeposition of Fe powders from the electrolyte containing 0.1 M $FeCl_3$ + 0.2 M $Na_3C_6H_5O_7$ + 1 M NH_4Cl (a) and 0.1 M $FeCl_2$ + 0.2 M $Na_3C_6H_5O_7$ + 1 M NH_4Cl (b) (Reprinted from [61] with the permission of Elsevier.)

The polarization curves were recorded starting from the potential of −0.6 V vs. Ag|AgCl. By comparing the polarization curves for Fe powder deposition from Fe(III) (curve a) and Fe(II) (curve b) salts in ammonium chloride–sodium citrate electrolyte, shown in Fig. 5.23, certain cathodic current density (~−2.5 mA cm^{-2}) has been detected already at the starting potential for curve a (inset of Fig. 5.23). This cathodic current density remained constant down to the potential of about −1.0 V and it started rising at the same potential value at which the current density recorded in the presence of Fe(II) salt started to rise.

A low current efficiency for the Fe–Ni alloy powder deposition from the solution containing Fe(III) salt is the consequence of the first step in the overall reaction being reduction of Fe(III) species into Fe(II) species, which takes place at all potentials more negative than −0.2 V.

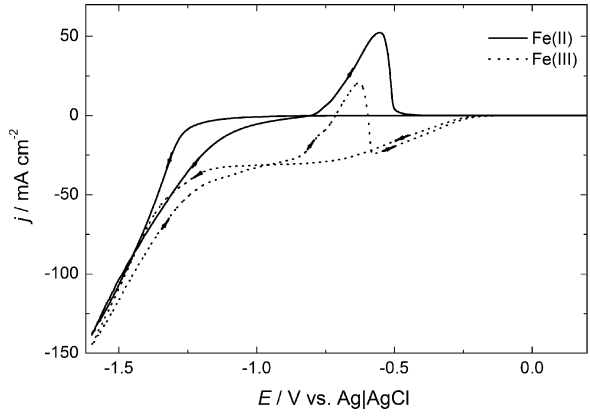

Fig. 5.24 The cyclic voltammograms recorded at the sweep rate of 10 mV s^{-1} and RPM = 1,000 onto Au electrode in the electrolytes containing 0.1 M Fe(III) (*dotted line*) and 0.1 M Fe(II) (*solid line*) salts (Reprinted from [61] with the permission of Elsevier.)

5.3.1.1 Cyclic Voltammograms of Fe Electrodeposition from Fe(III) and Fe(II) Salts

To investigate this phenomenon more closely, RDE electrode was used. The cyclic voltammograms at the sweep rate of 10 mV s^{-1} and RPM = 1,000 were recorded in both solutions in the potential limit from −1.6 to 0.6 V. The results are shown in Fig. 5.24 (from 0.2 to 0.6 V there was no indication of any reaction).

In the conditions of convective diffusion the deposition of Fe starts at about −1.3 V in both solutions, with the peaks of Fe dissolution being placed between −0.8 V and −0.5 V. In the presence of Fe(III) salt well-defined cathodic wave, typical for the diffusion controlled process, has been detected in the potential range between −0.2 V and −1.2 V. Hence, it is obvious that before the commencement of Fe deposition from Fe(III) salt, the reduction of Fe(III) into Fe(II) occurs. The reduction process of Fe(III) into Fe(II) has been investigated at different rotation rates. As can be seen in Fig. 5.25a, the current density plateau for this process increases with increasing rotation rate. By plotting the values of the current density plateaus recorded

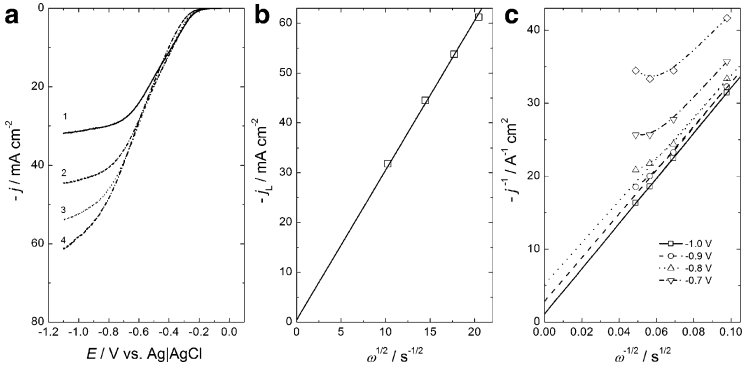

Fig. 5.25 (**a**) Cathodic cyclic voltammograms for Fe(III) reduction ($v = 10$ mV s^{-1}) recorded at different RPM's: 1—RPM = 1,000; 2—RPM = 2,000; 3—RPM = 3,000 and 4—RPM = 4,000. (**b**) j_L vs. $\omega^{1/2}$ recorded at the potential of −1.0 V. (**c**) j^{-1} vs. $\omega^{-1/2}$ recorded at different potentials (marked in the figure). Electrolyte: 0.1 M $FeCl_3$ + 0.2 M $Na_3C_6H_5O_7$ + 1 M NH_4Cl (Reprinted from [61] with the permission of Elsevier.)

at the potential of −1.0 V (j_L) as a function of the $\omega^{1/2}$, well-defined linear relation has been obtained, Levich's equation [136], as shown in Fig. 5.25b. The diffusion coefficient of the species undergoing reduction during this process, calculated from the slope of this dependence, amounts to ~3.7×10^{-5} cm^2 s^{-1}. In comparison with the diffusion coefficient for $Fe(CN)_6^{3-}$ ions (0.6×10^{-5} cm^2 s^{-1}) [136] higher value has been obtained, indicating that this process is not a simple diffusion-controlled one electron exchange from Fe(III) to Fe (II), since in both cases the reduction of complexes ($Fe(CN)_6^{3-}$ and $FeC_6H_5O_7$) is considered. Taking into account that the concentration of reacting Fe(III) species (actually $FeC_6H_5O_7$ complex) is high (0.1 M), a mixed activation–diffusion control could be expected. Considering plots presented in Fig. 5.25c (j^{-1} vs. $\omega^{-1/2}$ recorded at different potentials marked in the figure), it is obvious that the reduction of Fe(III) species into Fe(II) species is not under pure diffusion control. As can be seen the intercept on the j^{-1} axis exists at potentials of −1.0 V, −0.9 V, and −0.8 V, while at more positive potentials this dependence deviates from linearity, indicating the presence of activation-controlled current density [136]. It should be emphasized here

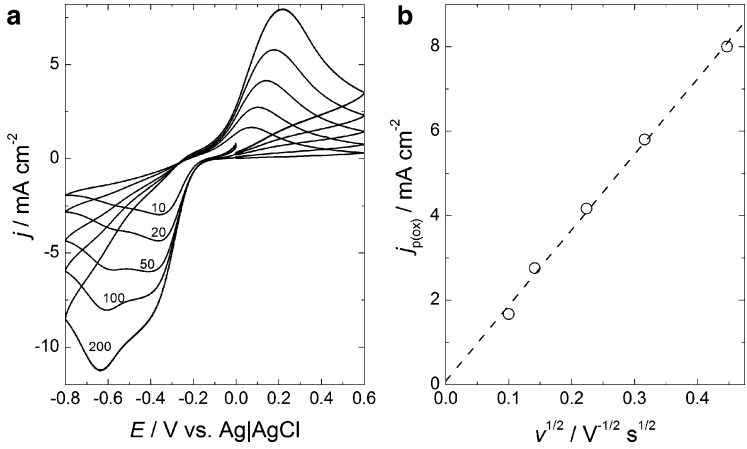

Fig. 5.26 (**a**) The cyclic voltammograms of Fe(III) species reduction and Fe(II) species oxidation recorded at different sweep rates (marked in the figure in mV s^{-1}) in the stagnant electrolyte (RPM = 0) onto Au electrode in the electrolyte containing 0.1 M $FeCl_3$ + 0.2 M $Na_3C_6H_5O_7$ + 1 M NH_4Cl. (**b**) $j_{p(ox)}$ vs. $v^{1/2}$ dependence obtained from the anodic current density peaks of oxidation shown in (**a**) (Reprinted from [61] with the permission of Elsevier.)

that in the case of convection (RPM > 0) no counter peak for the oxidation of these species could be detected at potentials more positive than 0.0 V. In the case of stagnant electrolyte (RPM = 0) the reduction and oxidation peaks of these species are clearly seen on the cyclic voltammograms, as shown in Fig. 5.26a.

The presence of two cathodic peaks and one anodic peak confirms the statement that this process is not a simple diffusion-controlled one electron exchange from Fe(III) to Fe(II), as well as not pure diffusion controlled process (activation control is also involved [136]). By plotting current density of oxidation peaks ($j_{p(ox)}$) versus $v^{1/2}$, well-defined linear dependence is also obtained (Fig. 5.26b), indicating diffusion-controlled oxidation [136], but the value of the diffusion coefficient calculated from the slope of this dependence (assuming that the concentration of reduced species is 0.1 M) was one order of magnitude lower than expected. Hence, it could be concluded that Fe(III) species reduce in the potential range between −0.2 V and −1.0 V and that under the convective diffusion reduced

species were removed from the electrode surface into the bulk of solution and could not be oxidized during the reverse sweep. Their oxidation is possible only in stagnant electrolyte, where they remain in the vicinity of the electrode surface (Fig. 5.26a).

Considering the stability (formation) constants for all complexes that could be formed in the investigated solutions, following data have been obtained: [124]

$$Fe^{3+} + HC_6H_5O_7{}^{2-} \rightarrow [FeHC_6H_5O_7]^{+} \quad K_1 = 3.17 \times 10^{12} \tag{5.1}$$

$$Fe^{3+} + C_6H_5O_7{}^{3-} \rightarrow [FeC_6H_5O_7] \quad K_1 = 1.0 \times 10^{25} \tag{5.2}$$

$$Fe^{3+} + OH^{-} \rightarrow [FeOH]^{2+} \quad K_1 = 7.4 \times 10^{11} \tag{5.3}$$

$$Fe^{3+} + 2OH^{-} \rightarrow [Fe(OH)_2]^{+} \quad K_2 = 1.5 \times 10^{21} \tag{5.4}$$

$$Fe^{3+} + 3OH^{-} \rightarrow [Fe(OH)_3] \quad K_3 = 4.7 \times 10^{29} \tag{5.5}$$

$$Fe^{2+} + HC_6H_5O_7{}^{2-} \rightarrow [FeHC_6H_5O_7] \quad K_1 = 1.2 \times 10^{3} \tag{5.6}$$

$$Fe^{2+} + C_6H_5O_7{}^{3-} \rightarrow [FeC_6H_5O_7]^{-} \quad K_1 = 3.16 \times 10^{15} \tag{5.7}$$

$$Fe^{2+} + OH^{-} \rightarrow [FeOH]^{+} \quad K_1 = 3.6 \times 10^{5} \tag{5.8}$$

$$Fe^{2+} + 2OH^{-} \rightarrow [Fe(OH)_2] \quad K_2 = 5.9 \times 10^{9} \tag{5.9}$$

$$Fe^{2+} + 3OH^{-} \rightarrow [Fe(OH)_3]^{-} \quad K_3 = 4.7 \times 10^{9} \tag{5.10}$$

$$Fe^{2+} + 4OH^{-} \rightarrow [Fe(OH)_4]^{2-} \quad K_4 = 3.8 \times 10^{8} \tag{5.11}$$

As can be seen, 11 different species could be formed, five with Fe^{3+} ions and six with Fe^{2+} ions. Taking into account their stability constants and concentration of complexing agents, it appears that for Fe(III) salt the most stable ones are $[FeC_6H_5O_7]$ and $[Fe(OH)_3]$, while for Fe(II) salt the most stable ones are $[FeC_6H_5O_7]^{-}$ and $[Fe(OH)_2]$. The possibility of $Fe(OH)_3$ formation could be excluded since at

pH 4.5 concentration of OH^- ions is 3.16×10^{-10} M and the dominant species in the Fe(III) salt electrolyte is complex $[FeC_6H_5O_7]$.

Let us reconsider the process of Fe powder deposition from the electrolyte containing Fe(III) salt. The reduction of $[FeC_6H_5O_7]$ starts at about −0.2 V producing Fe(II) species. Taking into account the presence of two cathodic peaks during this reduction process, it could not be specified which species were formed, pure Fe^{2+} ions or complex $[FeC_6H_5O_7]^-$ (the most stable complex with the Fe^{2+} ions), or both. It is most likely that both species were formed and that Fe deposition occurs by further reduction of these species with simultaneous hydrogen evolution which should be pronounced at potentials more negative than −1.3 V. Since during the Fe deposition pH in the vicinity of the electrode surface is much higher due to massive hydrogen evolution, it is possible that Fe^{2+} ions react with OH^- ions forming $[Fe(OH)_2]$ which precipitates and prevents deposition of pure Fe powder. On the other side, in the solution containing Fe(II) salt the possibility of $[Fe(OH)_2]$ formation could also be excluded since at pH 4.0 concentration of OH^- ions is 1.0×10^{-10} M and the dominant species is complex $[FeC_6H_5O_7]^-$. Accordingly, the reduction of this complex starts at about −1.3 V producing Fe deposit directly, without the possibility of eventual $[Fe(OH)_2]$ formation, and in this solution Fe powder has been successfully deposited.

In the case of the solutions for Fe–Ni alloy powder electrodeposition, among the species presented above for Fe, the following species could be formed with Ni in the investigated solutions: [124]

$$Ni^{2+} + HC_6H_5O_7{}^{2-} \rightarrow [NiHC_6H_5O_7] \quad K_1 = 1.3 \times 10^5 \tag{5.12}$$

$$Ni^{2+} + C_6H_5O_7{}^{3-} \rightarrow [NiC_6H_5O_7]^- \quad K_1 = 2.0 \times 10^{14} \tag{5.13}$$

$$Ni^{2+} + OH^- \rightarrow [NiOH]^+ \quad K_1 = 9.3 \times 10^{14} \tag{5.14}$$

$$Ni^{2+} + 2OH^- \rightarrow [Ni(OH)_2] \quad K_2 = 3.5 \times 10^8 \tag{5.15}$$

$$Ni^{2+} + 3OH^- \rightarrow [Ni(OH)_3]^- \quad K_3 = 2.0 \times 10^{11} \tag{5.16}$$

As can be seen, again the most stable one is $[NiC_6H_5O_7]^-$ and the same conclusion concerning the formation of Ni-hydroxide species in the investigated solutions as the one given above for Fe could be applied. Hence, Ni electrodeposition occurs by the reduction of citrate complex $[NiC_6H_5O_7]^-$ without the possibility for Ni-hydroxide species formation.

Among the above-mentioned complexes of Fe and Ni, ammonium complexes could be formed with Fe(II) and Ni ions in ammonium chloride solution, chloride complex could be formed with Fe(II) and Fe(III) and sulfate complexes could be formed with Fe(III) and Ni, but they all have several orders lower stability constants in comparison with citrates and cannot influence the reaction mechanism.

5.3.2 *Chemical Compositions of the Fe–Ni Alloy Powders*

All powder samples for chemical analysis, phase composition analysis, and morphology investigations were electrodeposited under the same conditions as for Co–Ni alloy powders, except that the current density for powder electrodeposition was the value presented in Fig. 5.21 with j_{pd}.

Chemical composition of all electrodeposited Fe–Ni alloy powders was determined by the AAS technique after dissolving certain amount of powders in HCl. Also, chemical composition of these alloy powders was determined from the average values of EDS analysis. All powder samples were analyzed by EDS in such a way that at least 8 powder agglomerates (maximum number 20) on the SEM micrographs were chosen and EDS analysis was performed at 3–10 different positions on each particle. In some cases the analysis was performed at a point of 1 μm^2, while in some cases rectangle surface from 120 μm^2 (10 $\times$ 12 μm) to 9,600 μm^2 (80 $\times$ 120 μm) has been analyzed. In some cases the composition of the powder agglomerates was uniform all over the agglomerates surface, while in some cases at. % of oxygen was found to vary significantly on the surface of one particle, or on specific part of the analyzed particle. This behavior was

Table 5.2 The average composition of the Fe–Ni powders electrodeposited from Fe(III) and Fe(II) salts containing electrolytes, obtained by the EDS analysis (in at.%)

	Fe(III) solution			Fe(II) solution			Ni solution	
Ni/Fe	O	Fe	Ni	O	Fe	Ni	O	Ni
Ni							20	80
9/1	22	34	44	5	21	74		
3/1	34	41	25	8	35	57		
1/1	33	55	12	12	58	30		
1/3	12	83	5	30	62	8		
Fe				20	80			

Reprinted from [61] with the permission of Elsevier

independent of the shape of the investigated particle (flat surface, cone-shaped cavities, different crystals on the particle surface), as well as of the composition of the powders. Taking into account that the EDS analysis strongly depends on the position and angle of the beam, for powder agglomerates like these presented in this work the EDS analysis results should not be considered as quantitative ones. Hence, in Table 5.2 are presented average values (obtained by the analysis of significant number of agglomerates for each powder) for the EDS analysis of all powder samples. From the presented results it is most likely that the presence of oxygen could be the consequence of washing and drying procedure. It could also be possible that the oxygen is a result of eventual [$Fe(OH)_2$] formation during the powder deposition, as explained in Sect. 5.3.1.1 for pure Fe powder deposition. In such a case it would be reasonable to expect higher percentage of oxygen in the powders containing higher amount of Fe for Fe–Ni alloy powders deposited from the electrolyte containing Fe(III) salt, while for powders deposited from the electrolyte containing Fe(II) salt percentage of oxygen should be relatively constant for all investigated compositions.

As can be seen in Table 5.2, this was not the case. Hence, it appeared that during the deposition of Fe–Ni alloy powders the behavior of pure metals cannot be considered as relevant for the properties of alloy powders, since they form solid solution-type alloys which behave in a different way than pure metals. It should be stated that the results of the chemical and EDS analysis (after subtraction of oxygen percentages) were in good agreement.

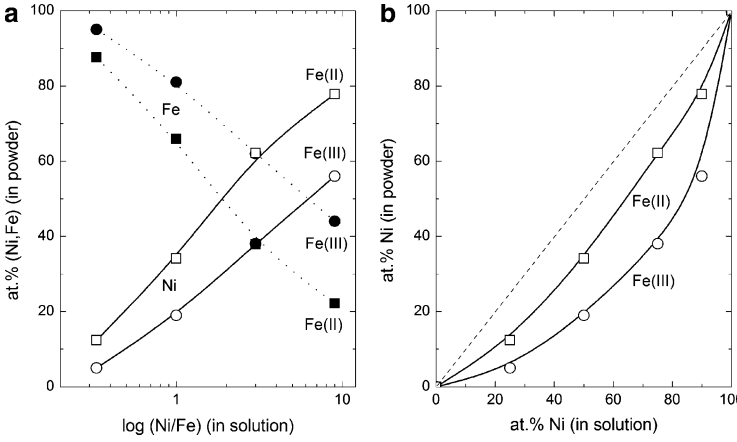

Fig. 5.27 (**a**) Dependences of at.% of Fe (*filled circle and square*) and Ni (*open circle and square*) in the powders as a function of the Ni/Fe ratio: electrolyte containing Fe(III) (*filled and open circle*) and Fe(II) (*filled and open square*) salts. (**b**) Typical Brenner's presentation of anomalous codeposition for the powders electrodeposited from the electrolytes containing Fe(III) (*open circle*) and Fe(II) (*open square*) salts [116] (Reprinted from [61] with the permission of Elsevier.)

The composition analysis was performed for powders electrodeposited from the solutions containing Fe(III) and Fe(II) salts.

The dependence of at. % of both metals as a function of the log (Ni/Fe) ratio is presented in Fig. 5.27a. As it could be expected the content of Ni increases, while the content of Fe decreases with the increase of the Ni/Fe ratio. According to Fig. 5.27a almost linear dependence of the percentage of both metals in the powder as a function of the logarithm of their concentration ratios indicates that their content in the powder depends exponentially on the Ni/Fe ratio. Considering Fig. 5.27b it could be concluded that the anomalous character is more pronounced in the electrolytes containing Fe(III) salt. This is in accordance with the statement that the formation of some amount of $[Fe(OH)_2]$ is possible in this electrolyte and assuming "hydroxide suppression" mechanism [125, 126] the anomalous character of Fe and Ni deposition should be more pronounced in this electrolyte.

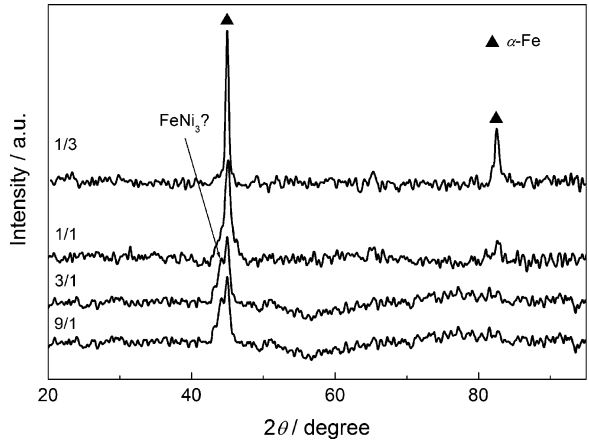

Fig. 5.28 Diffractograms of Fe–Ni alloy powders electrodeposited at different Ni/Fe ions ratios (marked in the figure) (Reprinted from [62] with the permission of Springer-Verlag.)

5.3.3 Phase Compositions of the Fe–Ni Alloy Powders

The diffractograms of Fe–Ni alloy powders electrodeposited at different Ni/Fe ions ratios from the solution of Fe(II) species are presented in Fig. 5.28. It should be stated that the dimensions of crystallites were 7 nm for the Ni/Fe ratio 9/1 and that they increased with the increase of iron content in the powder to 20 nm (for Ni/Fe = 1/3). Because of very small dimensions of crystallites, only phases with the highest intensity were determined with high certainty and these were peaks of the α-Fe phase (▲). Taking into account that the peaks of FeNi (37-0474), α-Fe (06-0696), and Ni (45-1027) practically overlap, a wide peak at about 44.5° for Ni/Fe = 9/1, 3/1, and 1/1 could be ascribed to any of these phases. The appearance of a small peak at about 44.3° for Ni/Fe = 9/1 and 3/1 indicates the presence of $FeNi_3$ {111} (38-0419), since pagoda-like crystals, typical for this phase, have been detected on the surface of powder agglomerates obtained from these solutions (see Sect. 5.3.4).

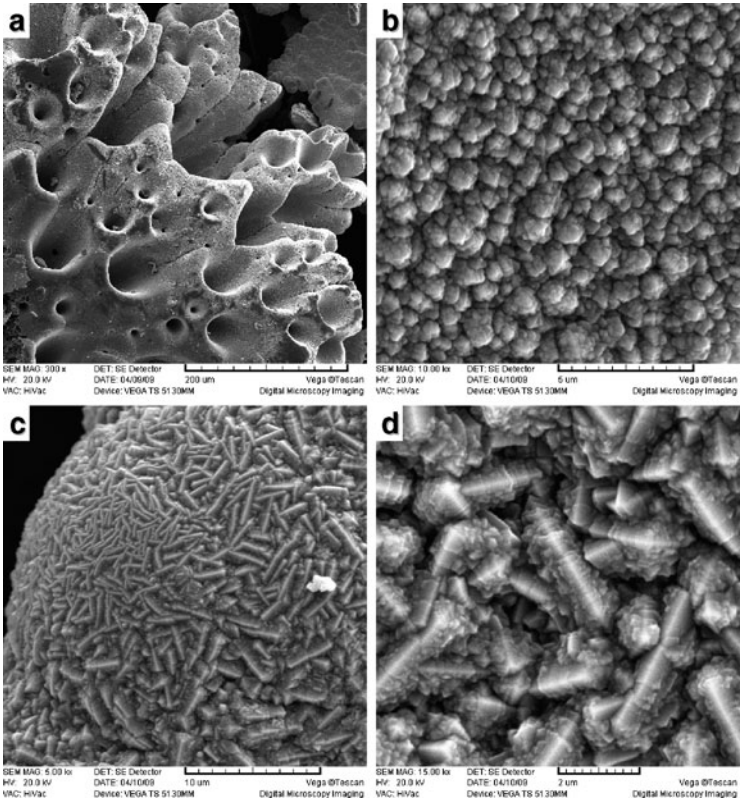

Fig. 5.29 Morphology of the Fe–Ni alloy powder electrodeposited at the Ni/Fe = 9/1

5.3.4 Morphology of Electrodeposited Fe–Ni Powders

5.3.4.1 The Fe–Ni Alloy Powders Obtained from the Solutions Containing Fe(II) Species

The morphology of the Fe–Ni alloy powders electrodeposited at different Ni/Fe ratios are presented in Figs. 5.29–5.32. A common characteristic of all investigated Fe–Ni powders is the formation of

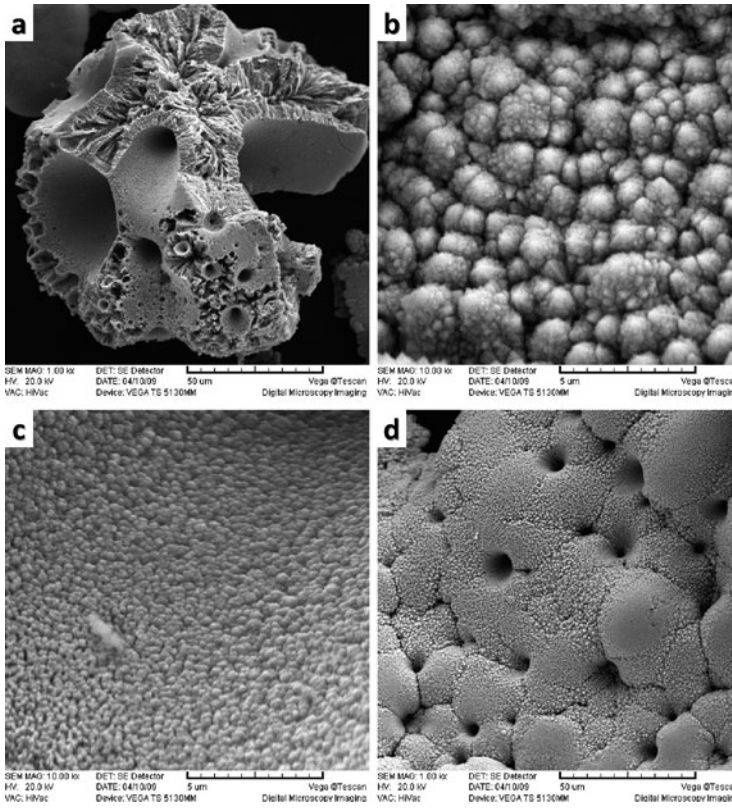

Fig. 5.30 Morphology of the Fe–Ni alloy powder electrodeposited at the Ni/Fe = 3/1

big agglomerates (up to 500 μm). Their surfaces are covered with large cone-shaped cavities, as well as with much smaller cylindrical cavities.

In Fig. 5.29 are presented typical agglomerates for Fe–Ni alloy powders electrodeposited at the Ni/Fe ratio 9/1. Large cone-shaped cavities and much smaller cylindrical cavities, corresponding to the places were hydrogen bubbles were formed, are clearly seen in Fig. 5.29a. Nodular surfaces are covered with two types of crystals: pagoda-like crystals (Fig. 5.29b) and crystals of the shape of

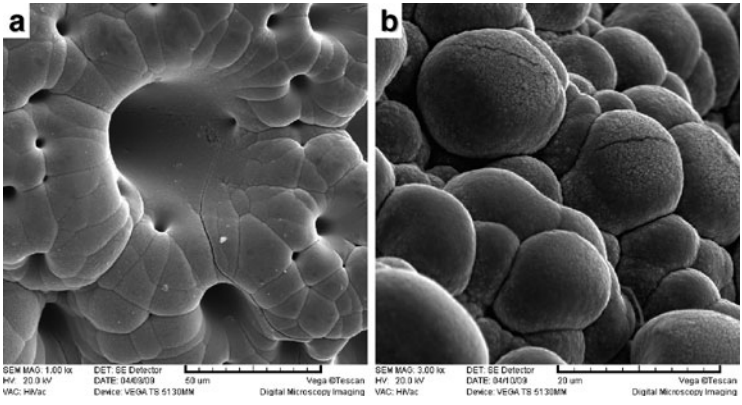

Fig. 5.31 Morphology of the Fe–Ni alloy powder electrodeposited at the Ni/Fe = 1/1 (Reprinted from [62] with the permission of Springer-Verlag.)

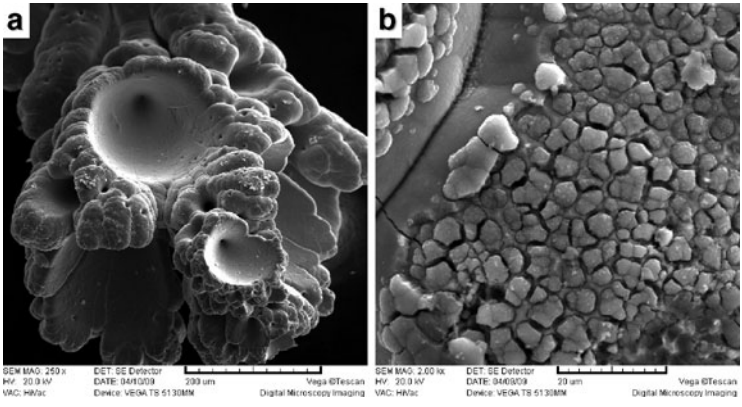

Fig. 5.32 Morphology of the Fe–Ni alloy powder electrodeposited at the Ni/Fe = 1/3 (Reprinted from [62] with the permission of Springer-Verlag.)

elongated prism (Fig. 5.29c, d), indicating possible presence of different phases.

Large cone-shaped cavities and much smaller cylindrical cavities are also present in the powder electrodeposited at Ni/Fe = 3/1

(Fig. 5.30a). Nodular surfaces (Fig. 5.30d) as well as the inside surface of cone-shaped cavities (Fig. 5.30c) are covered with spherical crystals (Fig. 5.30b).

Much smoother surface of both types of cavities and the nodular endings were obtained from the solution with Ni/Fe = 1/1 (Fig. 5.31).

In the case of the highest content of iron in the powder (Ni/Fe = 1/3) similar shape of cavities (Fig. 5.32a) was obtained as in Fig. 5.31a, while the surface of nodular endings was not smooth.

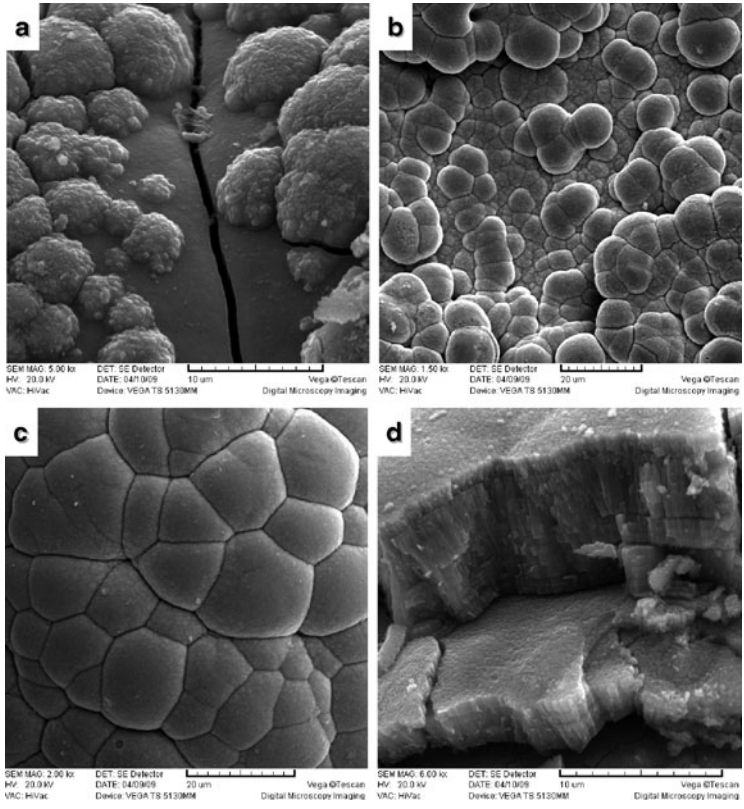

Fig. 5.33 Typical phases of the Fe–Ni powder growth

On some parts of the agglomerates surface new crystals were separated with the cracks, as shown in Fig. 5.32b.

Considering Figs. 5.29–5.32 it could be seen that on the compact surface of all agglomerates smaller spherical (rounded) grains were formed (Figs. 5.30b–d and 5.31b). The formation of such spherical grains is typical for the electrodeposition of copper from acidic sulfate electrolytes under the conditions of activation–diffusion controlled process [137]. Such mechanism has been explained for the electrodeposition of pure cobalt. The development of spherical grains in the case of Fe–Ni electrodeposition is presented in Fig. 5.33. As can be seen in Fig. 5.33a, the second generation of spherical grains grow in all directions. On the compact surface spherical grains are well defined (Fig. 5.33b) and since they are close to each other they start to overlap. During the further growth the overlapping of the diffusion zones formed over each spherical grain becomes more pronounced producing practically flat surface of the agglomerates (Fig. 5.33c). It is interesting to note that the growth of compact agglomerates of spherical grains occurs through the formation of layer-by-layer stick-like densely packed crystals of submicron dimensions, as shown in Fig. 5.33d. Presented figures are in excellent agreement with already given explanation for the electrodeposition of powders.

5.3.4.2 The Fe–Ni Alloy Powders Obtained from the Solutions Containing Fe(III) Species

The main characteristic of these powders is the presence of high number of both types of cavities on the surfaces of big agglomerates (up to 500 μm), as shown in Fig. 5.34. Taking into account that the current efficiency for the electrodeposition of these powders is only 1–2%, massive hydrogen evolution must produce larger number of cavities than in previous cases. Also, one of the characteristics of these powders is the presence of several different types of crystals on the surface of agglomerates around the cavities, which are presented in Figs. 5.35–5.38. On the agglomerates surfaces electrodeposited from the solutions with Ni/Fe = 9/1 and 3/1 mostly spherical agglomerates could be detected, as shown in Fig. 5.35a. At the

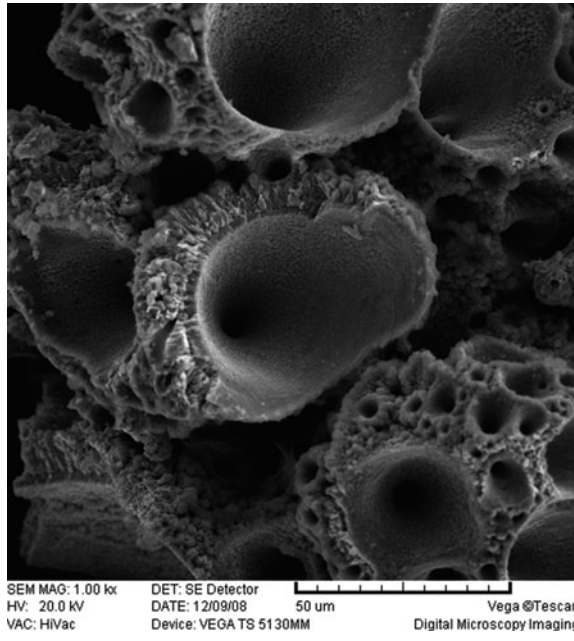

Fig. 5.34 Typical distribution of cavities on the surface of the Fe–Ni alloy powder agglomerates electrodeposited from the solution containing Fe(III) species

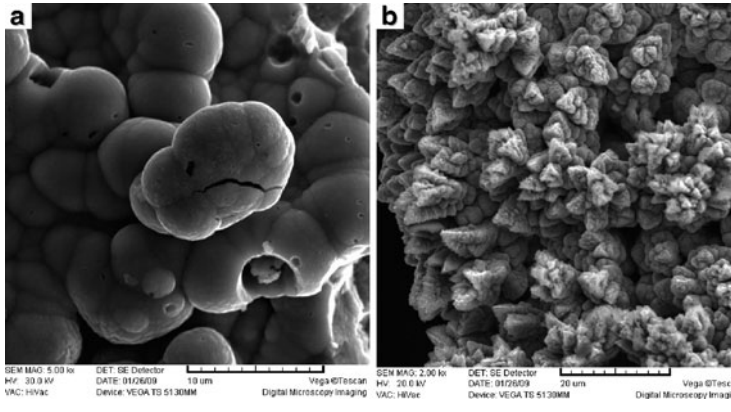

Fig. 5.35 Crystals formed on the surface of the Fe–Ni alloy powder agglomerates electrodeposited from the solution with Ni/Fe = 9/1 (Reprinted from [61] with the permission of Elsevier.)

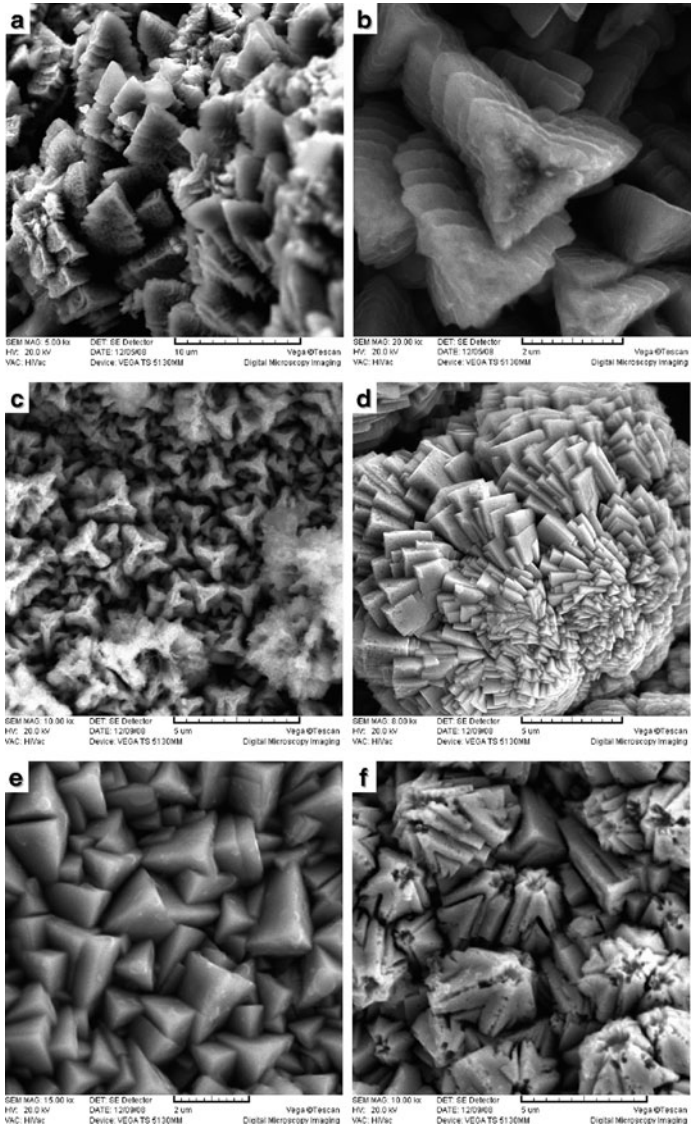

Fig. 5.36 Crystals formed on the surface of the Fe–Ni alloy powder agglomerates electrodeposited from the solution with Ni/Fe < 1

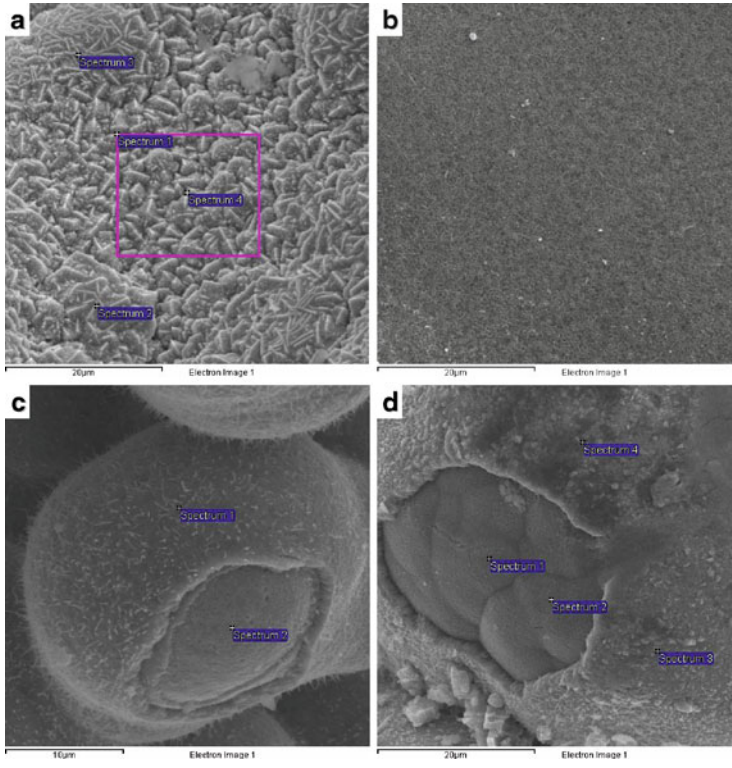

Fig. 5.37 Typical surface morphologies for all electrodeposited Fe–Ni alloy powders after annealing in air at 400°C for 3 h: (**a**) Ni/Fe = 9/1; (**b**) Ni/Fe = 3/1; (**c**) Ni/Fe = 1/1; and (**d**) Ni/Fe = 1/3 (Reprinted from [62] with the permission of Springer-Verlag.)

same time, pagoda-like crystals (b) have been detected on a certain, not negligible, number of agglomerates. Particularly interesting are crystals of the shape of pagoda. Such crystals were detected in the Fe–Ni powder synthesized in high yield by a simple and facile hydrothermal method without the presence of surfactants [137]. According to this investigation [137], $FeNi_3$ {111} single crystals were formed during the described procedure. The products obtained at 120°C were a mixture of $FeNi_3$ and Fe–Ni hydroxides composed of

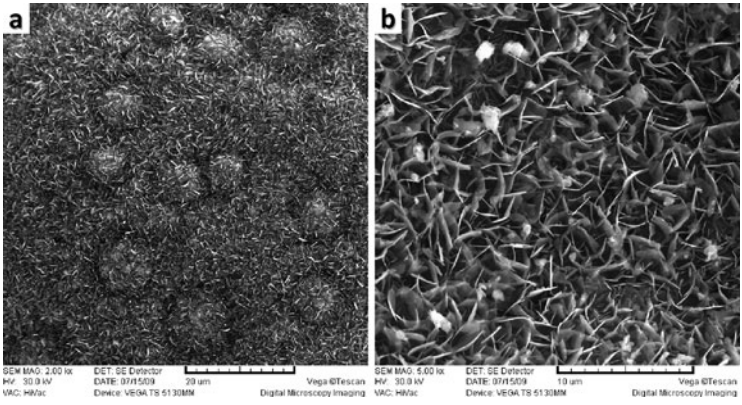

Fig. 5.38 (**a**) Typical surface morphologies for the Fe–Ni alloy powders electrodeposited at Ni/Fe ratios 9/1 and 3/1 after annealing in air at 600°C for 3 h. (**b**) Typical surface morphologies for the Fe–Ni alloy powders electrodeposited at Ni/Fe ratios 1/1 and 1/3 after annealing in air at 600°C for 3 h (Reprinted from [62] with the permission of Springer-Verlag.)

monodispersed microspheres (probably spheres presented in Fig. 5.35a). With the increase of temperature to 140°C these microspheres became micropagodas very similar to those shown in Fig. 5.35b. At higher temperatures (180°C) these agglomerates transform into perfect 3D $FeNi_3$ dendritic superstructures in certain directions [137]. Hence, comparing the crystals presented in Fig. 5.35b with those obtained by hydrothermal method [137] it seems reasonable to ascribe them to the $FeNi_3$ {111} single crystals (there is also an indication for the existence of $FeNi_3$ phase in electrodeposited powder—see XRD analysis presented in Fig. 5.28).

As the amount of iron increases in the powders (above 50 at.%), the number of different crystals detected on the agglomerates surfaces also increases. In the powders electrodeposited from the solutions with Ni/Fe = 1/3 very small amount of agglomerates is covered with spherical agglomerates, while most of them are characterized with the presence of several different shapes of crystals. These crystals are presented in Fig. 5.36a–f. It is quite difficult to explain the reasons for their appearance, since so many different phases do not exist in the Fe–Ni system

and the only reasonable explanations could be that these crystals represent some superstructures formed under massive hydrogen evolution. Their shapes could be defined as follows: (a) Christmas tree-like crystals; (b) triangle-like crystals growing layer by layer; (c) propeller-like crystals; (d) plate-like crystals; (e) tetrahedral crystals, and (f) traversed polyhedron.

5.3.5 *Formation of $NiFe_2O_4$ by the Oxidation of Fe–Ni Alloy Powders*

To produce $NiFe_2O_4$, all electrodeposited powders were annealed in air, at first at the temperature of 400°C for 3 h. After SEM, EDS, and XRD analysis, powders were additionally annealed at 600°C for 3 h and analyzed by SEM, EDS, and XRD. Finally, since it was found that big agglomerates had not been completely oxidized during annealing at 600°C, powders were ground in mortar, annealed at 700°C for 3 h, and analyzed by XRD.

Typical morphologies of the surface of annealed (recrystallized) powders agglomerates (EDS) for all investigated electrolyte compositions after the first annealing procedure are shown in Fig. 5.37. The appearance of different types of crystals on powder agglomerates surface for different Ni/Fe ions ratios is characteristic for these powders. To find out what is the composition of the obtained crystals, the EDS analysis of all samples was performed and the results at different spectrum positions are given in Table 5.3. A common characteristic of the EDS analysis is the decrease of Ni content on the surface of analyzed samples with the decrease of Ni/Fe ratio (42 at.% Ni for the 9/1 ratio, Fig. 5.37a, and 27 at.% Ni for the 3/1 ratio, Fig. 5.37b), i.e., the decrease of Ni content in the alloy powders, while for the Ni/Fe ratios 1/1 and 1/3 the content of Ni on the powder agglomerates surfaces is practically zero. It is interesting to note that on the surface of samples with the Ni/Fe ratios 1/1 and 1/3 some parts of the agglomerates surfaces have been peeled off (Fig. 5.37c, d) and that the composition of the surface layer is completely different than that of the bulk of particle (Table 5.3).

Table 5.3 Results of the EDS analysis of powder samples electrodeposited from different electrolytes, obtained at different positions (spectra) at powder agglomerates presented in Fig. 5.37

Ni/Fe	Spectrum number	at.% O	at.% Fe	at.% Ni
9/1	1	39	25	36
	2	24	23	53
	3	31	19	50
	4	41	29	30
3/1	1	57	19	24
1/1	1	48	52	0
	2	42	35	23
1/3	1	29	67	4
	2	51	43	6
	3	58	42	0
	4	51	49	0

Reprinted from [62] with the permission of Springer-Verlag

According to the EDS analysis of these two samples, it appears that the surface layer is composed of iron oxide (most likely Fe_2O_3), since the content of Ni is zero. For powder samples with lower content of Fe (Ni/Fe = 9/1 and 3/1, Fig. 5.37a, b) layered structure was observed (no peeling off of the surface layer was detected) and, accordingly, only the composition of the surface was analyzed. Taking into account that for such surfaces EDS results cannot be considered as quantitative, a convincing conclusion about the properties of these powder agglomerates surfaces could not be made. Hence, it appears from the EDS analysis of the powder agglomerates surfaces that for samples with higher content of Fe (Ni/Fe = 1/1 and 1/3, Fig. 5.37c, d) the oxidation of all powders agglomerates was not complete and that only surfaces were completely oxidized due to iron oxide diffusion to the surface of the agglomerates during the oxidation process. Taking into account the dimensions of the powder agglomerates (agglomerates up to about 400 μm), it is quite possible that the oxidation process took place mostly on the agglomerates surface. It is possible that the same conclusion could be valid for samples rich in Ni, but on the SEM micrographs peeling off of the surface layer was not detected.

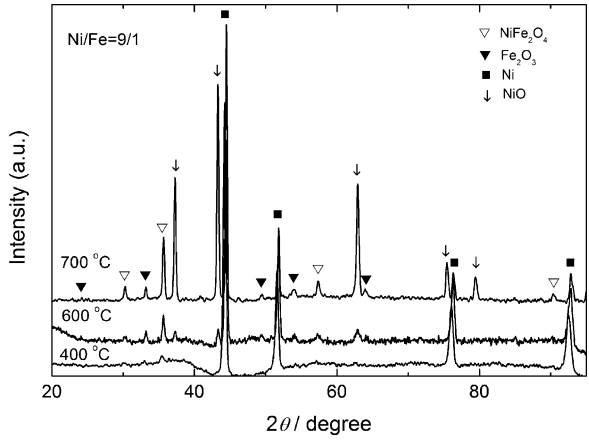

Fig. 5.39 Diffractograms for the Fe–Ni alloy powders electrodeposited at Ni/Fe = 9/1 after annealing in air at 400°C, 600°C, and 700°C for 3 h (Reprinted from [62] with the permission of Springer-Verlag.)

During the second annealing procedure (additional annealing at 600°C for 3 h in air) all powder samples were characterized with the presence of needle-like crystals on the surface of agglomerates (most likely corresponding to the Fe_2O_3 phase), with their dimensions being bigger for samples with higher content of Fe. This is shown in Fig. 5.38a for Ni/Fe ratios 9/1 and 3/1 and in Fig. 5.38b for Ni/Fe ratios 1/1 and 1/3. In comparison with the samples annealed at 400°C the EDS analysis showed higher content of Fe and O for samples obtained at Ni/Fe ratios 9/1 and 3/1, while for samples obtained at Ni/Fe ratios 1/1 and 1/3 identical results were obtained as those for the annealing at 400°C (see Table 5.3).

XRD results recorded after annealing at 400°C, 600°C, and 700°C are shown in Figs. 5.39–5.42. These results are in good agreement with the EDS analysis, showing that all powder agglomerates were oxidized during annealing, forming NiO, Fe_2O_3, and $NiFe_2O_4$ phases. As can be seen, the intensity of some peaks increases, while the intensity of some peaks decreases with increasing annealing temperature.

The intensity of Ni peaks (■) was found to decrease with increasing annealing temperature for Ni/Fe ratios 9/1, 3/1, and 1/1, with

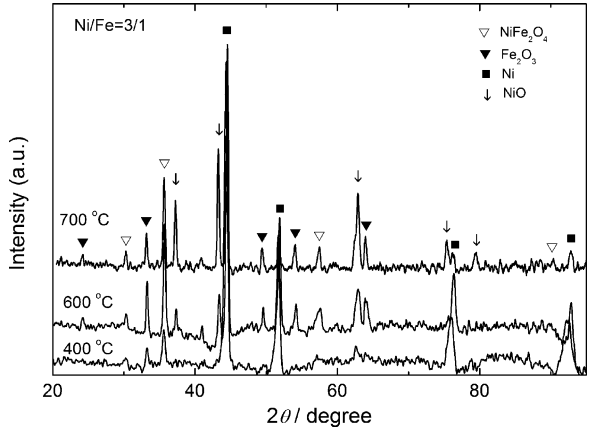

Fig. 5.40 Diffractograms for the Fe–Ni alloy powders electrodeposited at Ni/Fe = 3/1 after annealing in air at 400°C, 600°C, and 700°C for 3 h (Reprinted from [62] with the permission of Springer-Verlag.)

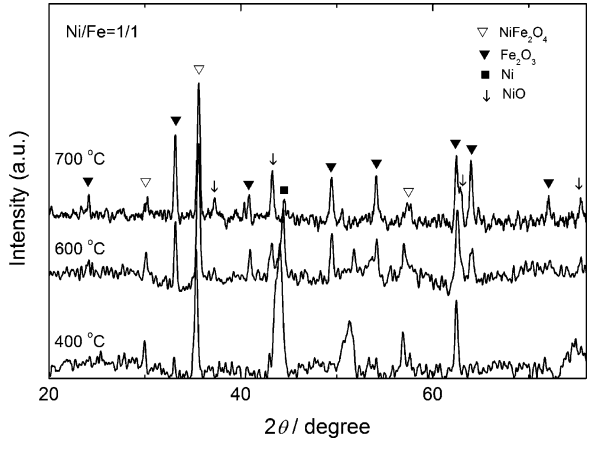

Fig. 5.41 Diffractograms for the Fe–Ni alloy powders electrodeposited at Ni/Fe = 1/1 after annealing in air at 400°C, 600°C, and 700°C for 3 h (Reprinted from [62] with the permission of Springer-Verlag.)

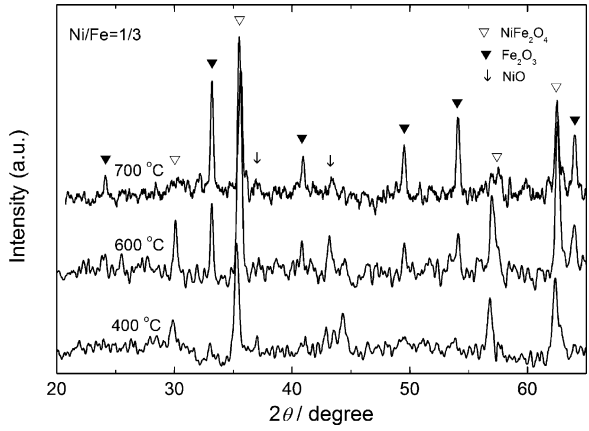

Fig. 5.42 Diffractograms for the Fe–Ni alloy powders electrodeposited at Ni/Fe = 1/3 after annealing in air at 400°C, 600°C, and 700°C for 3 h (Reprinted from [62] with the permission of Springer-Verlag.)

Ni being most likely oxidized into NiO and/or $NiFe_2O_4$ phases. The Ni phase practically disappeared in powders electrodeposited at the Ni/Fe ratio 1/3 annealed at all temperatures. Its presence on the diffractograms recorded for the annealing temperatures 400°C and 600°C in powders electrodeposited at the Ni/Fe ratios 9/1, 3/1, and 1/1 indicates that in these powders Ni cannot be completely oxidized at given annealing temperatures. The disappearance of the Ni phase in powder electrodeposited at Ni/Fe = 1/1 after annealing at 700°C confirms that during additional oxidation whole amount of Ni has been oxidized.

The intensity of the peak for NiO phase (↓) increased with increasing annealing temperature for samples rich in Ni (Ni/Fe = 9/1 and 3/1), while for other two samples NiO peaks (↓) of small intensities were detected. As can be seen in Fig. 5.42, this phase practically disappeared in the powder electrodeposited at Ni/Fe ratio 1/3 after annealing at 700°C.

The intensity of the peaks for Fe_2O_3 phase (▼) also increased with increasing annealing temperature in all samples. In samples with high content of Ni this phase has not been detected on the diffractograms recorded after annealing at 400°C only. After annealing at 700°C this phase became dominant in Fe-rich samples (Ni/Fe = 1/1 and 1/3).

Similar conclusion could be made for the $NiFe_2O_4$ phase (▽). In all samples peaks of this phase could be detected on the diffractograms recorded after annealing at 600°C and 700°C. It is interesting to note that the peaks of $NiFe_2O_4$ phase (▽) possess the highest intensity in the powder electrodeposited at Ni/Fe ratio 1/3 after annealing at 600°C, indicating that these are the best conditions for its formation. Such behavior is in accordance with the findings of Ceylan et al. [89] that well-defined $NiFe_2O_4$ nanoparticles crystallize at 550°C after solid state reaction in $Fe_{67}Ni_{33}$ nanopowder. Hence, it appears that for a powder composition 89 at.% Fe—11 at.% Ni (powder obtained for Ni/Fe ratio 1/3), which is different than that for $Fe_{67}Ni_{33}$, dominant phase is $NiFe_2O_4$ after annealing of electrodeposited powder at 600°C.

5.4 System Mo–Ni–O

The Mo–Ni–O powders were electrodeposited from two supporting electrolytes, as in the case of Co–Ni system: 1 M NH_4Cl + 0.7 M NH_4OH and 1 M $(NH_4)_2SO_4$ + 0.7 M NH_4OH, with the pH of the solutions being 9.0.

5.4.1 Polarization Curves

5.4.1.1 Polarization Curves in Chloride Containing Electrolytes

Three different electrolytes were used for the investigations: 0.1 M $NiCl_2$ + 1 M NH_4Cl + 0.7 M NH_4OH + x M Na_2MoO_4, with x being 0.05 M, 0.1 M, and 0.3 M, respectively. In such a way the Ni/Mo ions concentration ratio was 1/0.5, 1/1, and 1/3. All powders for microstructure, composition, and phase composition analysis were electrodeposited at the limiting current density (position of the inflection point B on the polarization curves, see Fig. 5.43). In all cases small amount of the rough compact deposit (necessary for powder formation) remained on the glassy carbon surface and only agglomerates detached from the cathode surface were analyzed.

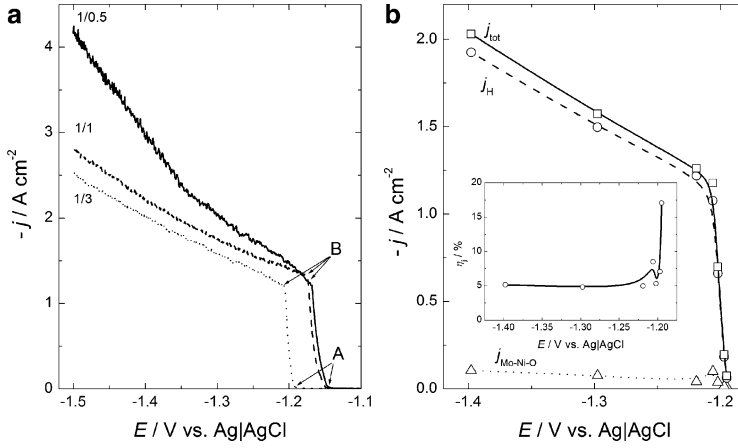

Fig. 5.43 (**a**) Polarization curves in chloride containing electrolytes for different Ni/Mo ratios (marked in the figure). (**b**) Polarization curve for powder electrodeposition and hydrogen evolution (j_{tot}), polarization curve for hydrogen evolution (j_H), and polarization curve for powder electrodeposition after subtraction of the current density for hydrogen evolution ($j_{Mo–Ni–O}$). *Inset*: current efficiency for Mo–Ni–O powder electrodeposition (η_j) as a function of potential (Reprinted from [121] with the permission of Elsevier.)

The polarization curves are presented in Fig. 5.43. As can be seen, the polarization curves characterized by two inflection points (Fig. 5.43a), as in all previous cases, were obtained. It is important to note that the potential of the beginning of alloy deposition (A) becomes more negative with the increase of molybdate ions concentration (with the decrease of Ni/Mo ratio), as it could be expected, since the potential of the Mo deposition is much more negative than that of Ni [116]. At the same time, a deposition of Mo can only take place in the presence of Ni (induced codeposition [116]). Taking into account that the concentration of Ni^{2+} ions was constant, it is quite reasonable that the value of current density of the inflection point B does not change with changing Ni/Mo ions concentration ratio (being about -1.2 A cm^{-2}).

It should also be mentioned that the current efficiency for alloy deposition in all cases was very low, about 5%. This could be seen in the inset of Fig. 5.43b for the Ni/Mo ratio 1/3, where the η_j vs. E changes from 17% to 5% in the region of sharp increase of current

density, while at the potentials more negative than the second inflection point (B) the value of η_j is constant, being about 5%.

5.4.1.2 Polarization Curves in Sulfate Containing Electrolytes

Three different electrolytes were used for the investigations: 0.1 M $NiSO_4$ + 1 M $(NH_4)_2SO_4$ + 0.7 M NH_4OH + x M Na_2MoO_4, with x being 0.03 M, 0.1 M, and 0.3 M, respectively. In such a way the Ni/Mo ions concentration ratio was 1/0.3, 1/1, and 1/3. The polarization curves recorded in the solution containing sulfate ions are presented in Fig. 5.44. In this case all polarization curves are moved to slightly more cathodic potentials, indicating higher overvoltage for the process of Mo–Ni–O alloy electrodeposition in the presence of sulfate ions (Fig. 5.44a). At the same time, the total current densities in the range of potentials more negative than the inflection point (B) are smaller and the slopes of their changes are smaller in comparison with those recorded for chloride electrolyte (Fig. 5.43a). As in the case of chloride electrolyte, the potential of the beginning of alloy deposition (A) becomes more negative with the increase of molybdate ions concentration (with the decrease of Ni/Mo ratio). As shown in Fig. 5.44b, the current efficiency for alloy deposition is sensitive to the Ni/Mo ions ratio: for Ni/Mo = 1/0.3, $\eta_j = 10\%$, for Ni/Mo= 1/1, $\eta_j = 7\%$, and for Ni/Mo = 1/3, $\eta_j = 5\%$ [all η_j values correspond to the potentials more negative than the second inflection point (B)].

5.4.2 Morphology of As-Deposited Mo–Ni–O Powders

5.4.2.1 Morphology of Powders Electrodeposited from Chloride Containing Electrolytes

The morphologies of powder agglomerates electrodeposited onto glassy carbon electrode from electrolytes with different Ni/Mo ions concentration ratios (1/0.5, 1/1, and 1/3, samples 1, 2, and 3, respectively) are shown in Figs. 5.45 and 5.46, respectively. For the highest

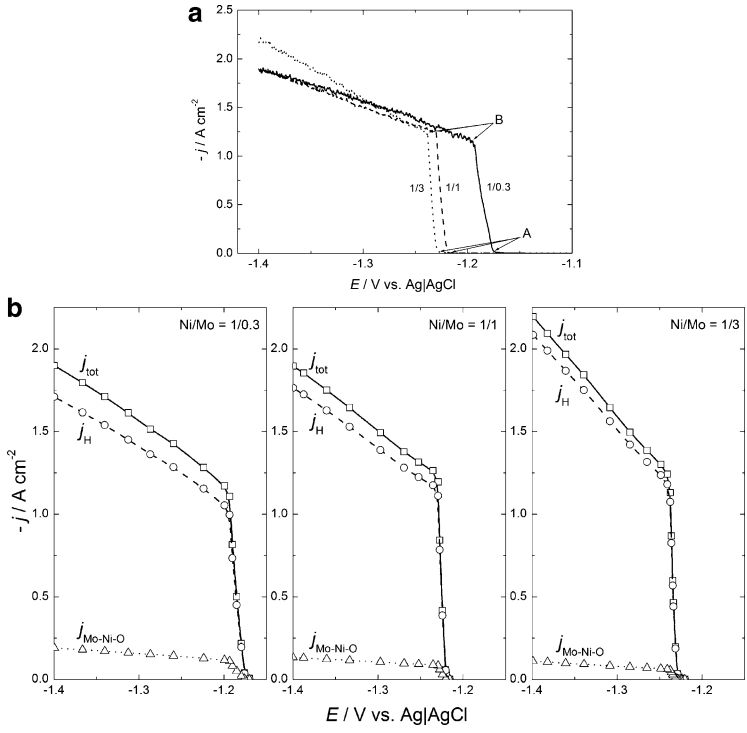

Fig. 5.44 (**a**) Polarization curves in sulfate containing electrolytes for different Ni/Mo ratios (marked in the figure). (**b**) Polarization curves for powder electrodeposition and hydrogen evolution (j_{tot}), polarization curves for hydrogen evolution (j_H), and polarization curves for powder electrodeposition after subtraction of the current density for hydrogen evolution ($j_{Mo–Ni–O}$) (Reprinted from [122] with the permission of Elsevier.)

Ni/Mo ratio of 1/0.5 (Fig. 5.46) the size of the agglomerates varies in the range of about 2–50 μm. At the same time, sharp edges could be detected on top of the surfaces of all agglomerates, indicating crystallinity of electrodeposited powder (Fig. 5.45b).

With the decrease of the Ni/Mo ratio (1/1), a cauliflower-type agglomerate, Fig. 5.46a, b, characterized with spherical edges (c) and the presence of cracks, was obtained. Its size is much higher than that of the powder particles electrodeposited at the 1/0.5 ratio, varying in

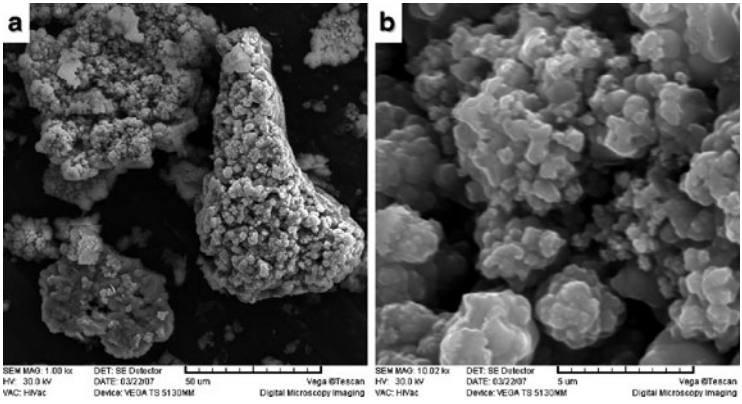

Fig. 5.45 Typical agglomerates for the Mo–Ni–O powders electrodeposited at the Ni/Mo = 1/0.5 (Reprinted from [121] with the permission of Elsevier.)

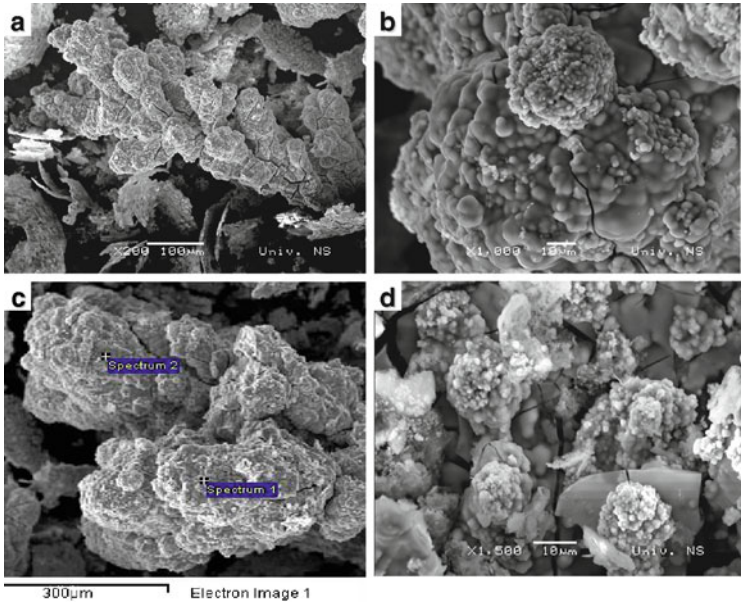

Fig. 5.46 (**a**, **b**, **c**) Typical particles for the Mo–Ni–O powders electrodeposited at the Ni/Mo = 1/1. (**d**) Typical particles for the Mo–Ni–O powders electrodeposited at the Ni/Mo = 1/3 (Reprinted from [121] with the permission of Elsevier.)

the range of about 50–500 μm. In the case of Ni/Mo ratio of 1/3, Fig. 5.46d, flat and thin parts of the powder, corresponding most likely to the compact deposit, were covered with spherical agglomerates, while the cracks are more pronounced. The appearance of a large number of cracks is the result of high tensile stresses present in the powder and the hydrogen evolution [138]. According to the presented results, it is obvious that the crystallinity of the particles becomes less pronounced with the increase of molybdate ions in the electrolyte, influencing at the same time the morphology of as-deposited powder particles.

5.4.2.2 The EDS Analysis of the As-Deposited Powders

All powder samples were analyzed by EDS in such a way that one powder particle on the SEM micrograph is chosen and EDS analysis was performed at two (or sometimes three) different positions on this particle, as shown in Fig. 5.46c. The approximate compositions of all alloy powders, evaluated by the EDS microanalysis, revealed that the composition depends not only on the Ni/Mo concentration ratio but also on the position at which the EDS analysis was performed. The results of the EDS analysis indicate the presence of significant amount of oxygen in the powders (up to about 70 at.%), as well as the nonhomogeneous composition of the as-deposited powders. At the same time the composition does not follow the Ni/Mo ions concentration ratio, although the theory of induced codeposition [116–120] predicts the increase of Mo amount in the deposit with increasing concentration of molybdate ions in the electrolyte. Such a behavior indicates that in the case of powder electrodeposition from ammonium chloride electrolyte, most likely, molybdenum is not deposited only as pure metal, but also as MoO_x species, as found in the literature for compact deposits [139–141]. At the same time, taking into account nonhomogeneous distribution of molybdenum, nickel, and oxygen in the electrodeposited powders, any conclusion concerning composition of the alloy obtained by the EDS analysis cannot be considered as reliable for this particular case.

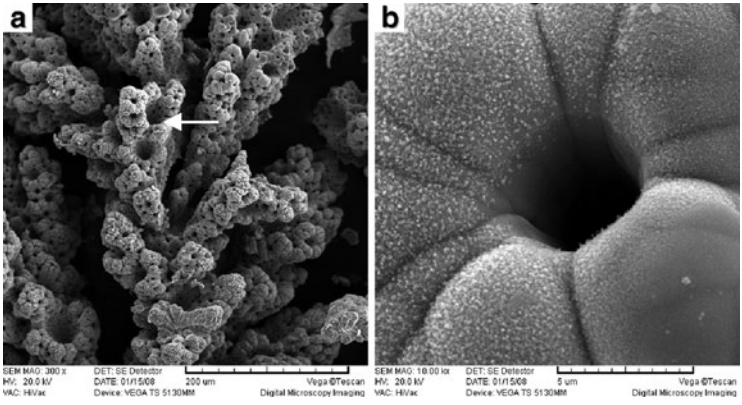

Fig. 5.47 (**a**) Typical spongy particles electrodeposited at the Ni/Mo = 1/0.3. (**b**) Cavity marked with *arrow* in (**a**) at higher magnification (Reprinted from [122] with the permission of Elsevier.)

5.4.2.3 Morphology of Powders Electrodeposited from Sulfate Containing Electrolytes

The morphology of powder particles electrodeposited from electrolytes with different Ni/Mo ions concentration ratios (1/0.3, 1/1, and 1/3) are shown in Figs. 5.47–5.49. Different morphology of the powder particles was obtained.

For the Ni/Mo ratio 1/0.3 typical spongy particles were detected, Fig. 5.47a. The characteristic of these particles is very flat surface around the holes, as shown in Fig. 5.47b.

With the decrease of the Ni/Mo ratio (1/1), two types of particles were obtained, as shown in Fig. 5.48. Both are spherical (rounded), one with flat edges (a) and another one with rough endings on top of the surface (b). Taking into account our previous investigations of alloy powders morphology [37–40], this is not unexpected. Since the growth of powder particles is characterized by the presence of two or more growth zones, it appears that spherical particles with flat edges have been detached from the electrode surface before the beginning of a growth of new zone, while the particles with rough endings have been detached after the beginning of the growth of a new crystals.

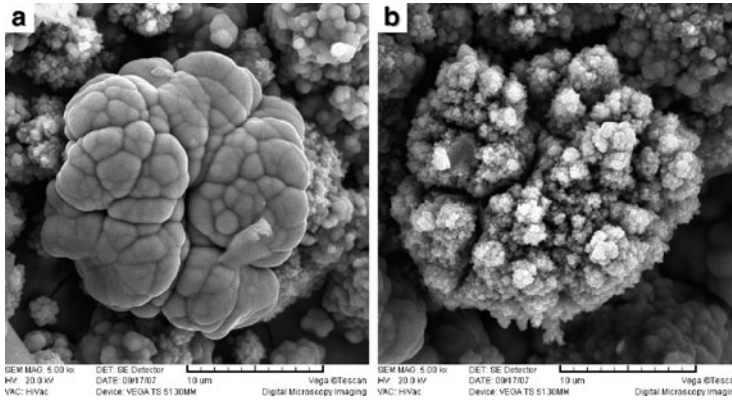

Fig. 5.48 Typical particles electrodeposited at the Ni/Mo = 1/1 (Reprinted from [122] with the permission of Elsevier.)

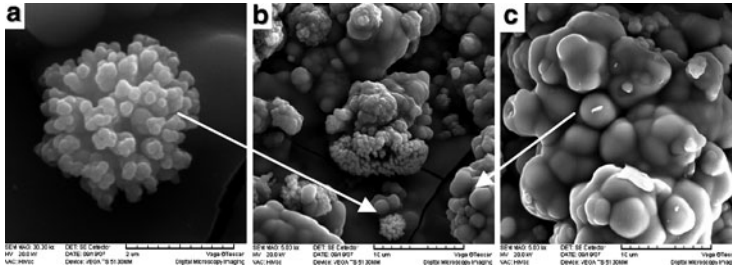

Fig. 5.49 (**a**) Agglomerate with dendritic surface. (**b**) Typical powder electrodeposited at the Ni/Mo = 1/3. (**c**) Agglomerate with flat surface (Reprinted from [122] with the permission of Elsevier.)

It should be noted (not shown in this figure) that some particles were characterized by the presence of cracks.

In the case of Ni/Mo ratio of 1/3 (powder with the highest amount of molybdenum) completely different morphology was detected, as shown in Fig. 5.49. The powder is composed of flat and thin parts with pronounced cracks, corresponding most likely to the compact deposit, and spherical agglomerates growing on top of a flat deposit (b). The surfaces of these agglomerates are either dendritic (a) or flat (c).

5.4.3 Composition and Phase Composition Analysis of As-Deposited and Recrystallized Powders Obtained from Chloride Electrolyte

The phase composition analysis of the powders was performed using XRD. In the case of as-deposited powders practically no peaks were detected on the diffractograms (except one broad peak observed near $2\theta = 40°$, see Fig. 5.51a—quasiamorph). It seems that, as in the case of compact deposits [121, 142], the crystallites were extremely small, i.e., of the order of nanometers and the powders were quasiamorphous. It was obvious that the Ni–Mo alloy powders should be previously recrystallized to determine their phase composition.

Two powder samples, electrodeposited from the solutions with Ni/Mo = 1/1 (sample 2) and Ni/Mo = 1/3 (sample 3), were analyzed by DSC and TGA to determine recrystallization temperature (Fig. 5.50) [121]. For both samples a multistep process with the sharp exothermic maximum on the DSC curves indicates that the recrystallization occurs at 543°C and should be performed at this or higher temperature. It should be noted that on the DSC curve for sample 2 additional small exothermic maximum, appearing at lower temperature of about 420°C, could be ascribed to the recrystallization of another phase present in the powder. At the same time, the TGA analysis revealed the weight loss of the samples of about 15%, corresponding most probably to the evaporation of electrolyte left in the pores of as-deposited powders.

Annealing (recrystallization) was performed in N_2 atmosphere at 600°C for 2 h. XRD analysis, shown in Fig. 5.51, revealed structural transformation and formation of $NiMoO_4$ and MoO_3 phases. For the recrystallized powder sample 3, Fig. 5.51a (recryst.), with the exception of few small peaks, all peaks correspond to the $NiMoO_4$ phase (▼), indicating that it is possible to obtain single phase Mo–Ni–O powder by electrochemical deposition and subsequent annealing in nitrogen. With the increase of Ni/Mo ratio (samples 1 and 2, Fig. 5.51b), among the $NiMoO_4$ phase (▼), MoO_3 phase (▽) was also detected in the powders with the intensity of its peaks increasing with the increase of the Ni/Mo ratio. From the intensity of the MoO_3 peaks it could be estimated that in sample 1 about 20% of MoO_3 is

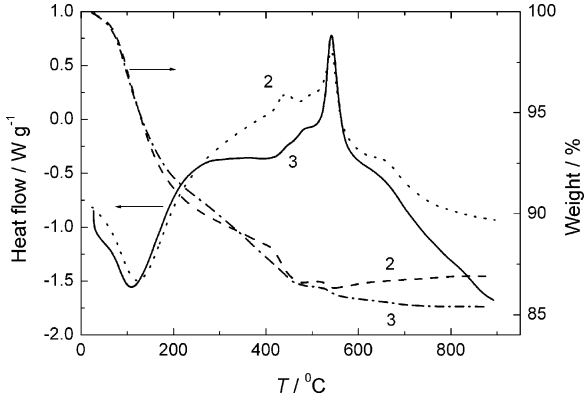

Fig. 5.50 The results of the DSC–TGA analysis for the samples 2 and 3 (marked in the figure) (Reprinted from [121] with the permission of Elsevier.)

present, while in sample 2 about 10% of MoO_3 is present. It is most probable that the peak at about $2\theta = 27^\circ$ corresponds to the $NiMoO_4$—K_β reflection (✦) [121].

5.4.3.1 The Morphology and EDS Analysis of Recrystallized Powders

The morphology of the recrystallized powders (SEM) is shown in Fig. 5.52a–c for samples 1, 2, and 3 respectively (see Table 5.3). In all cases regular crystals were obtained with smooth surfaces and well-defined crystal planes. The size of particles is much smaller than the size of as-deposited particles, varying between about 2 μm and about 10 μm, indicating that during the annealing procedure agglomerates formed by electrodeposition separate into much smaller crystals [121].

The EDS analysis was performed on the single crystal grains, mainly with an electron beam covering the area from about 6 μm^2 to about 30 μm^2 (depending on the dimensions of the crystal grains). In some cases the point analysis (as in the case of as-deposited

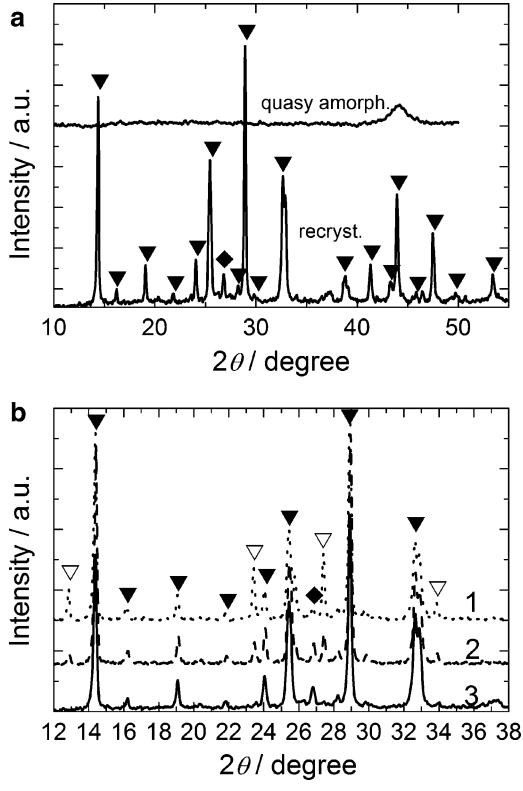

Fig. 5.51 (**a**) Diffractograms of the as-deposited (quasiamorph.) and recrystallized (recryst.) powder sample 3. (**b**) Diffractograms of the trecrystallized powder samples 1, 2, and 3 (marked in the figure) (Reprinted from [121] with the permission of Elsevier.)

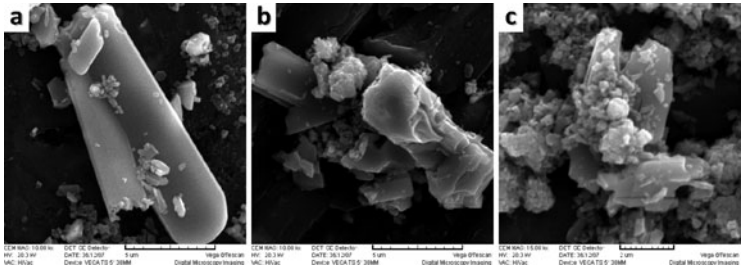

Fig. 5.52 Typical crystals for samples 1—(**a**), 2—(**b**), and 3—(**c**), detected after annealing of corresponding Mo–Ni–O powders at 600°C for 2 h (Reprinted from [121] with the permission of Elsevier.)

Table 5.4 The average composition of the recrystallized powders, determined by the EDS analysis

Sample No.	Ni/Mo	at.% O_2	at.% Ni	at.% Mo
1	1/0.5	79.49	7.54	12.97
2	1/1	80.19	8.02	11.79
3	1/3	76.99	10.28	12.73

Reprinted from [121] with the permission of Elsevier

powders, see Fig. 5.46c) was also performed. The results of the EDS analysis are presented in Table 5.4.

It is interesting to note that the average amount of Ni increases with increasing the concentration of molybdate ions in the solution (decrease of the Ni/Mo ratio), while at the same time the amount of Mo practically does not change with the decrease of the Ni/Mo ratio. Such a behavior is not in accordance with the described model, as well as with the theory of the induced codeposition [117–120]. This could be either due to the low precision of the EDS analysis, or the fact that the model and the theory were developed for the compact deposits (not applicable in the case of powder electrodeposition), or different mechanism of induced codeposition of Ni and Mo, or the consequence of solid state reaction occurring during annealing, or all of them together.

Ternary phase diagram for the system Mo–Ni–O [142, 143] is shown in Fig. 5.53. As can be seen, recrystallized samples 1, 2, and 3 are placed (according to the EDS analysis) in the region where three compounds could be expected, $NiMoO_4$, MoO_3, and O_2. Since XRD analysis cannot detect oxygen, the presence of MoO_3 and $NiMoO_4$ should be expected. At the same time the composition of all samples (EDS—Table 5.4) is not proportional to the ratio expected only for $NiMoO_4$ (1:1:4). Excess of molybdenum and oxygen clearly indicates the presence of MoO_3 and oxygen, particularly in samples 1 and 2. In the case of sample 3 only $NiMoO_4$ is detected by the XRD, most probably due to the composition of the recrystallized sample 3, which is very close to the line corresponding to $NiMoO_4$, so that the small amount of MoO_3 (less than 10%) cannot be detected. In this case the ratio expected only for $NiMoO_4$ (1:1:4) is also not achieved since some amount of oxygen (according to the ternary phase diagram [142, 143]) is present in the powder.

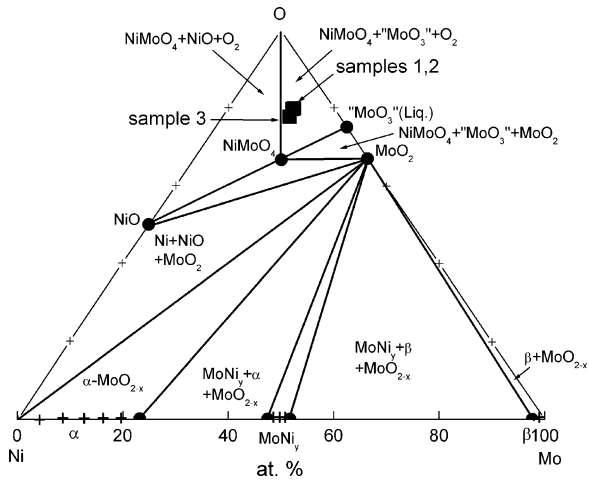

Fig. 5.53 Ternary phase diagram of the system Ni–Mo–O with the position of the recrystallized samples 1, 2, and 3 (marked in the figure—*filled square*) (Reprinted from [121] with the permission of Elsevier.)

According to the DSC analysis (Fig. 5.50), a small exothermic maximum appearing at lower temperature of about 420°C for sample 2 might correspond to the recrystallization of the MoO_3. It is most likely that during the annealing at 600°C in N_2 atmosphere for 2 h, not only recrystallization but also solid state reaction occurs, producing MoO_3 and $NiMoO_4$ phases. This assumption needed further clarification by other techniques (high temperature XRD, TEM) and is the subject of the investigations presented in Sect. 5.4.6.

5.4.4 Morphology, Composition and Phase Composition Analysis of Recrystallized Powders Obtained from Sulfate Electrolyte

To define temperatures of recrystallization and solid state reaction in the investigated Mo–Ni–O powders, stepwise annealing for 2 h in nitrogen atmosphere was performed (1) at 300°C, (2) at 400°C, (3) at

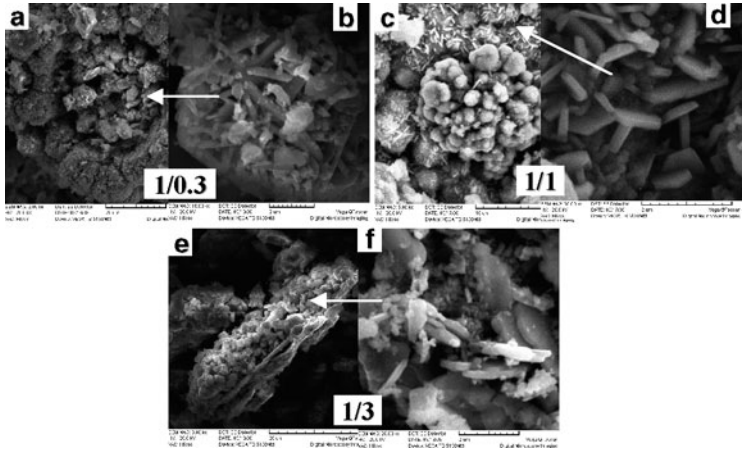

Fig. 5.54 SEM micrographs of the powders annealed at 300°C for the Ni/Mo ions ratios marked in the figure. Certain features of the powders are marked with *arrows* and shown at higher magnification in pictures (**b**) for the ratio 1/0.3, (**d**) for the ratio 1/1 and (**f**) for the ratio 1/3 (Reprinted from [122] with the permission of Elsevier.)

500°C, and (4) at 600°C. After each annealing procedure their morphology, composition, and phase composition were analyzed.

5.4.4.1 Analysis of Powders After Annealing at 300°C and 400°C

After the annealing at 300°C only small parts of the powders particles were recrystallized. As shown in Fig. 5.54, small crystals could be detected on the particles of all powders. It should be emphasized that the morphology of powder electrodeposited at Ni/Mo ratio 1/3 became completely different after this treatment. No flat and thin parts characterized by cracks (as it was the case for the as-deposited powder), corresponding most probably to the quasiamorphous (nanocrystalline) part of the powder deposit, could be detected. Hence, it appears that mostly this part of the powder crystallized.

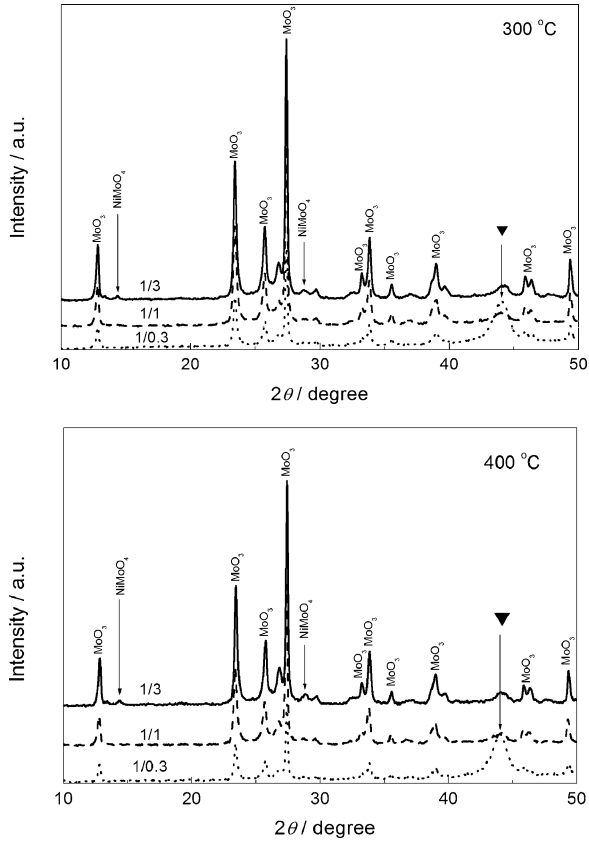

Fig. 5.55 Diffractograms for the powders annealed at 300°C and 400°C electrodeposited at different Ni/Mo ions ratios (marked in the figure) (Reprinted from [122] with the permission of Elsevier.)

Almost identical morphology was detected for the powders annealed at 400°C [122].

The corresponding diffractograms are shown in Fig. 5.55. As can be seen, already after annealing at 300°C MoO_3 phase was detected in powders electrodeposited at the Ni/Mo ions ratios 1/0.3 and 1/1, while for the powder electrodeposited at the Ni/Mo ions ratio 1/3 both MoO_3 and $NiMoO_4$ phases were detected, with the peaks for the

$NiMoO_4$ phase being very small, indicating that very small amount of this phase was present in the corresponding powder. A broad peak at about $2\theta = 44^\circ$ (▼), particularly pronounced for the powder electrodeposited for Ni/Mo = 1/0.3, could be, most likely, ascribed to a still nanocrystalline $NiMoO_4$ phase, but there is a possibility that a small amount of the $MoNi_4$ phase is present in the powder, since the peaks of these two phases overlap at $2\theta = 44$–45°. With the increase of the annealing temperature to 400°C practically the same results were obtained, indicating that no additional recrystallization occurred [122].

5.4.4.2 Analysis of Powders After Annealing at 500°C

The annealing at 500°C produced certain change in the powders morphology. As can be seen in Fig. 5.56, the powder containing the smallest amount of molybdenum [1/0.3(a) and 1/0.3(b)] retained mostly the same, spongy-type morphology. At the same time, agglomerates with flat surfaces are still visible [1/0.3(b)], while the bigger crystals and higher number of crystals could be detected on their surfaces. It is characteristic that the surface of agglomerates for all samples is covered with well-defined crystals of the shape of elongated stubs, corresponding to the α-MoO_3 phase [144].

After annealing the powders at 500°C (Fig. 5.57) more pronounced peaks for the $NiMoO_4$ phase appeared on all diffractograms, reflecting the increase of this phase in all powders. A broad peak at about $2\theta = 44^\circ$ became sharp, particularly for the powders electrodeposited at Ni/Mo ratios 1/1 and 1/3, corresponding to the $NiMoO_4$ phase with bigger dimension of crystallites (see Table 5.5).

5.4.4.3 Analysis of Powders After Annealing at 600°C

As can be seen in Fig. 5.58, the annealing at 600°C produced significant change in the morphology of powders. All powders transformed into well-defined crystals of much smaller dimensions than the dimensions of agglomerates, confirming the statement that a complete recrystallization of the Mo–Ni–O alloy powders occurred.

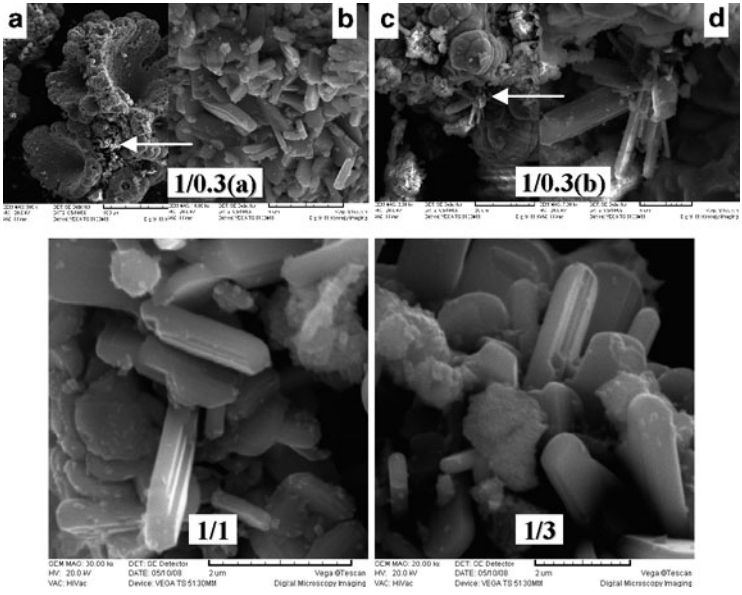

Fig. 5.56 SEM micrographs of the powders annealed at 500°C for the Ni/Mo ions ratios marked in the figure. Certain features of the powders are marked with *arrows* and shown at higher magnification in pictures (**b**) and (**d**) (Reprinted from [122] with the permission of Elsevier.)

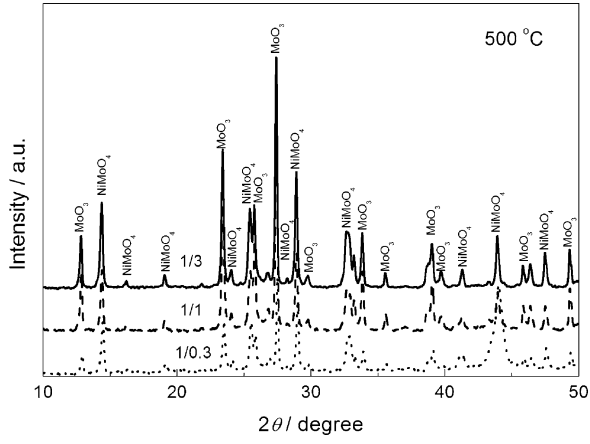

Fig. 5.57 Diffractograms for the powders annealed at 500°C electrodeposited at different Ni/Mo ions ratios (marked in the figure) (Reprinted from [122] with the permission of Elsevier.)

Table 5.5 The dimensions of crystallites of different phases of the system Ni–Mo–O as a function of the recrystallization temperature (T_r)

Phase	Ni/Mo	T_r (°C)	D_{110} (nm)[a]
MoO_3	1/0.3	300	31.37
		400	34.15
		500	43.47
	1/1	300	29.86
		400	29.57
		500	67.77
		600	95.51
	1/3	300	34.97
		400	35.49
		500	45.48
		600	82.25
Phase	Ni/Mo	T_r (°C)	D_{220} (nm)[b]
$NiMoO_4$	1/0.3	500	44.55
		600	70.04
	1/1	500	67.07
		600	81.28
	1/3	500	45.56
		600	75.94

Reprinted from [122] with the permission of Elsevier
[a]Reflections of the 110 (JCPDS 05-0508)
[b]Reflections of the 220 (JCPDS 33-0948)

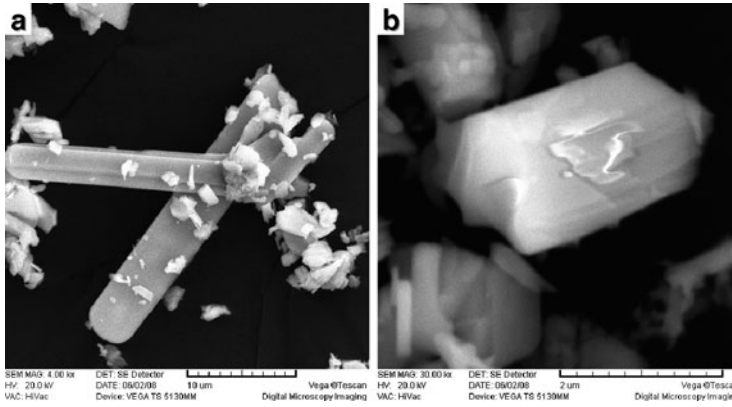

Fig. 5.58 SEM micrographs of the typical powder particles detected for all samples after annealing at 600°C (Reprinted from [122] with the permission of Elsevier.)

The most characteristic is the shape of elongated stubs (Fig. 5.58a) of bigger dimensions in comparison with the dimensions of other crystals (Fig. 5.58b).

The diffractograms recorded after annealing at 600°C are shown in Fig. 5.59a, b. As can be seen, significant change occurred for the powder electrodeposited at Ni/Mo = 1/0.3. The peaks for the MoO_3 phase disappeared, while the peaks for the $NiMoO_4$ phase became more pronounced. Such a behavior could be ascribed to the solid state reaction, with the $NiMoO_4$ phase being formed on the account of the MoO_3 phase. It is most likely that the solid state reaction took place in all powders, but only for the powder with the lowest amount of molybdenum (32 mass %, Table 5.6) all MoO_3 phase was consumed in the formation of the $NiMoO_4$ phase. It seems that the sharp peak recorded on the DSC curve at 543°C [121] corresponds to both complete recrystallization and solid state reaction of the Ni–Mo–O alloy powders.

The size of crystallites for both phases present in the Ni–Mo–O alloy powder deposits was determined by the analysis of certain peaks on the diffractograms shown in Figs. 5.55, 5.57, and 5.59a. Results are presented in Table 5.5. As expected, the size of MoO_3 and $NiMoO_4$ phase crystallites increases with increasing the annealing temperature of powders [122].

To find out whether the $MoNi_4$ phase had been formed after annealing the powder electrodeposited at the Ni/Mo = 1/0.3 at 600°C, additional XRD analysis of this sample was performed up to higher values of 2θ. The corresponding diffractogram is shown in Fig. 5.59b. As can be seen almost all peaks for this phase are present at the diffractogram, indicating that a small amount of the $MoNi_4$ phase has been formed. According to the shape (broad) and the height of the peaks, it is most likely that the crystallites were still small and that higher temperature should be applied for the complete recrystallization of this particular phase [122, 144–151].

According to the positions of the peaks on the diffractograms, for both MoO_3 and $NiMoO_4$ phases only α modifications were detected.

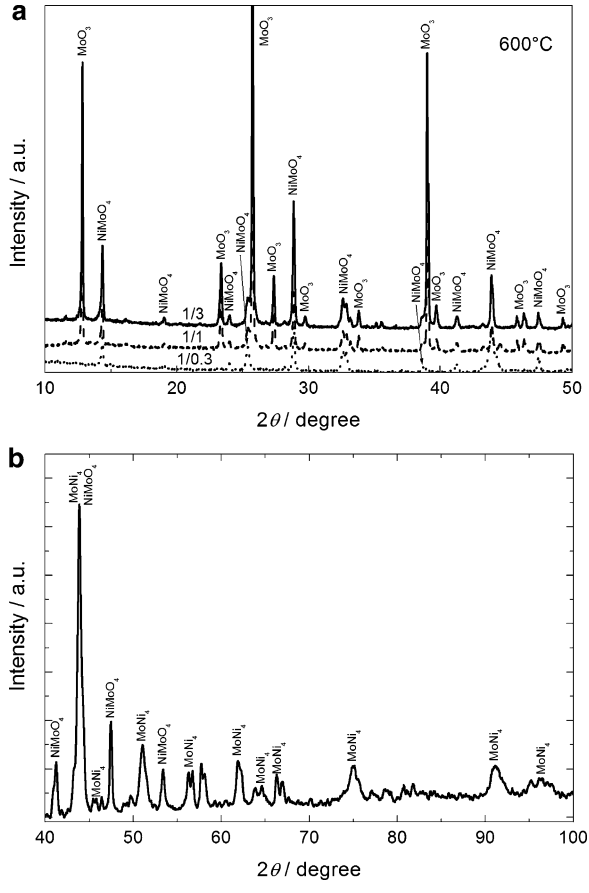

Fig. 5.59 (**a**) Diffractograms for the powders annealed at 600°C electrodeposited at different Ni/Mo ions ratios (marked in the figure). (**b**) Diffractogram for the powder annealed at 600°C electrodeposited at Ni/Mo =1/0.3, recorded at higher values of 2θ (from 40° to 100°) (Reprinted from [122] with the permission of Elsevier.)

Table 5.6 Chemical and EDS analysis of the Ni–Mo–O powders

	Chemical analysis			EDS analysis		
	Mass %		Spectrum	At.%		
Ni/Mo	Ni	Mo		O	Ni	Mo
1/0.3	68	32	1	66.69	15.80	17.52
			2	68.94	14.94	16.12
			3	61.64	13.34	16.84
1/1	50	50	1[a]	73.36	0.14	26.50
			2	69.84	13.11	17.05
			3	71.04	12.49	16.47
			4[a]	72.93	0.94	26.13
1/3	34	66	1[a]	73.72	0.00	5.46
			2[a]	72.31	0.00	25.32
			3[a]	75.59	0.00	24.41
			4	69.54	12.65	17.81
			5	65.02	13.52	14.55

Reprinted from [122] with the permission of Elsevier
[a]Particles of MoO_3

5.4.5 *The EDS and Chemical Analysis of the Powders Recrystallized at 600°C*

The EDS analysis was performed on the crystal grains (certain particles bigger than 1 μm) with an electron beam covering the area of 1 μm^2 (shown in Fig. 5.60 for all three powder compositions). The results of the EDS analysis are presented in Table 5.6 together with the results of the chemical analysis. In the chemical analysis only the mass percentages of Ni and Mo were determined.

As can be seen, the chemical composition of electrodeposited powders is identical to the ratios of Ni/Mo ions in the solution. It is characteristic that in powders electrodeposited at Ni/Mo ratio 1/0.3 all powder particles (agglomerates) are of the same, not well defined crystal shape, while at higher magnification their crystals of about 1–2 μm are well-defined (Fig. 5.60). In the case of powders electrodeposited at Ni/Mo ratios 1/1 and 1/3, two types of powder particles were detected. One, characteristic for the α-MoO_3, having a shape of very thin elongated stabs [144] reaching up to 20 μm in length, and another one of a rounded shape, belonging mainly to the

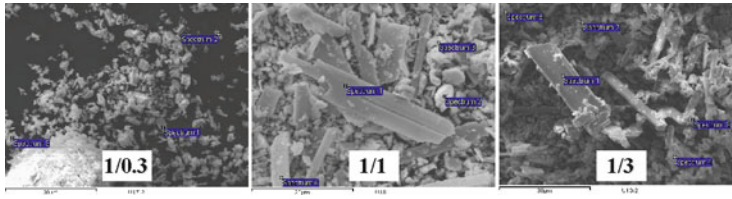

Fig. 5.60 SEM and EDS analysis of electrodeposited Mo–Ni–O powders after annealing at 600°C (Reprinted from [122] with the permission of Elsevier.)

α-$NiMoO_4$ phase [148–151]. This is confirmed by the results of the EDS analysis presented in Table 5.6. Taking into account the precision of the EDS analysis, it is quite difficult to obtain exact at. % ratio, particularly for small particles ($NiMoO_4$), but for bigger particles (like MoO_3) almost ideal Mo–O ratio has been detected on most of the analyzed samples (Fig. 5.60, Table 5.6).

As shown earlier, according to the ternary phase diagram for the system Ni–Mo–O [142, 143], the $NiMoO_4$ and MoO_3 phases should be seen at a given compositions of recrystallized powders. It is interesting to note that the previous [121] and present results [122] differ, since the presence of only one phase ($NiMoO_4$) in a previous work has been detected in the sample with the highest amount of molybdenum (Ni/Mo = 1/3), while in a present work this phase has been detected in the sample with the lowest amount of molybdenum (Ni/Mo = 1/0.3). Although previous powders were electrodeposited from the chloride containing solution, it is most likely that this difference is a consequence of the different procedures of powders annealing (recrystallization). Since in this investigation the existence of the phase transition has been confirmed, it seems more realistic that this process was more pronounced in the sample with the lowest amount of molybdenum in the powder, where the whole amount of MoO_3 phase has been consumed in the phase transition of MoO_3 phase into $NiMoO_4$ phase. Hence, single $NiMoO_4$ phase (with small amount of $MoNi_4$ phase) has been detected in this powder.

Taking into account that the investigated powders had to be annealed (recrystallized) to perform their phase composition analysis, the question arises: are these phases present in the as-deposited

powders? The only way to answer this question was to perform TEM analysis of as-deposited powders.

5.4.6 *The Results of TEM Analysis of As-Deposited Powders Obtained from Sulfate Electrolyte*

The TEM analysis was performed on two Mo–Ni–O powders: Ni-rich (Ni/Mo = 1/0.3) and Mo-rich (Ni/Mo = 1/3) powders. The common characteristic of both powders is the presence of amorphous and crystalline particles.

5.4.6.1 The TEM Analysis of Electrodeposited Ni-Rich Mo–Ni–O Powders

The specimen is composed of large amorphous clusters containing nanosized crystalline particles. Fig. 5.61 shows a TEM image of an amorphous particle (a) and the corresponding SAED pattern (b).

Diffuse diffraction rings clearly indicate amorphous character of this powder particle. Weak spots in the diffraction pattern correspond to the {211} reflections of fine $MoNi_4$ nanoparticles (JCPDF # 65-1533) [152], shown in the close-up in Fig. 5.61c. In the crystalline parts of the Ni-rich powder the following phases were detected: NiO, MoO_3, and $MoNi_4$, in the form of idiomorphic crystallites measuring up to 70 nm in diameter. Figure 5.62 shows a cluster of well-crystallized nanoparticles. The SAED pattern (shown in Fig. 5.62b) from these clusters best corresponds to the monoclinic MoO_3 phase (JCPDF # 89-1554) [153], or one of its structural variants, depending on the position in the sample. Typical morphology of euhedral MoO_3 crystals is shown in Fig. 5.62a and on the close-up in Fig. 5.62c. Most of the crystals are tabular on {200}. The strongest SAED diffraction rings in the pattern correspond to: $D_1 = \{200\}$, $D_2 = \{211\}$, $D_3 = \{220\}$, and $D_4 = \{022\}$. In the Ni-rich areas of the sample we observe crystalline $MoNi_4$ and NiO. $MoNi_4$ appears in the form of irregularly intergrown grains measuring up to 10 nm in average.

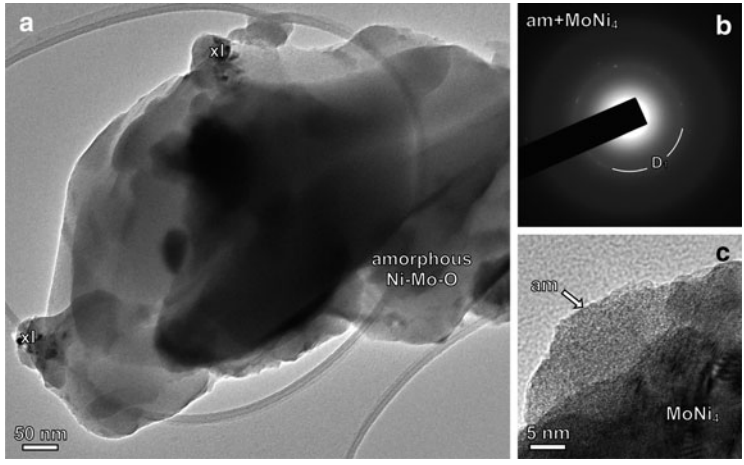

Fig. 5.61 (**a**) TEM image of the amorphous Mo–Ni–O particle detected in the powder electrodeposited at the Ni/Mo ratio 1/0.3. (**b**) SAED pattern recorded from this area (**a**) shows predominantly amorphous material (am) with weak reflections corresponding to $MoNi_4$ nanocrystals (x1). (**c**) High magnification of amorphous Mo–Ni–O particle with $MoNi_4$ nanocrystals (Reprinted from [123] with the permission of Elsevier.)

An area of prevailing $MoNi_4$ composition is shown in Fig. 5.63a, with corresponding SAED pattern in Fig. 5.63b. The strongest reflections were indexed to $D_1 = \{211\}$, $D_2 = \{002\}$, $D_3 = \{132\}$, and $D_4 = \{501\}$ [152]. In some areas we also find isolated crystals of NiO with a predominating cubic morphology and the edges truncated by rhombic dodecahedral faces. A close-up of a typical NiO nanocrystal is shown in Fig. 5.63c, showing well-resolved {200} lattice planes. The diffraction rings of the NiO phase cannot be seen most probably due to much stronger diffraction lines for the $MoNi_4$ and MoO_3 phases. Accordingly, its presence is determined by the measurement of D values, as shown in Fig. 5.63c [123].

It should also be stated that on both SAED patterns, and other SAED patterns, additional diffraction lines (more or less pronounced) are present, indicating that at the position of TEM analysis other phases are also present (actually at each position of TEM analysis mixture of different phases exists), but the best defined are

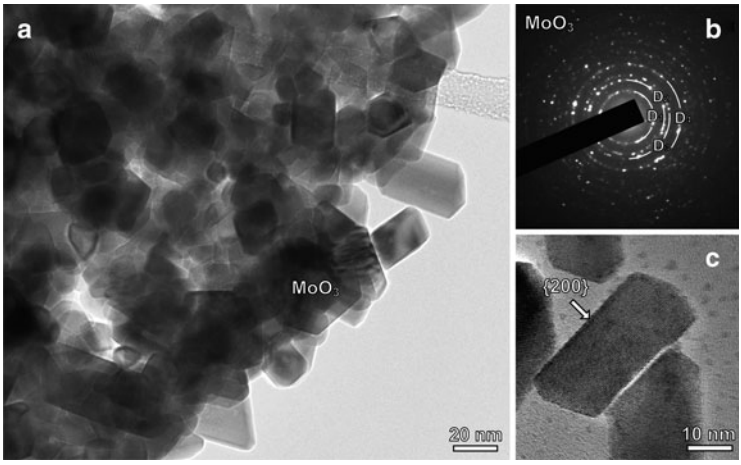

Fig. 5.62 (**a**) TEM image of euhedral MoO_3 nanocrystals in the sample with the Ni/Mo ratio 1/0.3. (**b**) Electron diffraction pattern from this area indicates the presence of monoclinic MoO_3 phase. The strongest SAED diffraction rings in the pattern correspond to and $D_1 = \{200\}$, $D_2 = \{211\}$, $D_3 = \{220\}$, and $D_4 = \{022\}$. (**c**) MoO_3 crystals are terminated with well-defined {200} dominating pinacoidal faces (Reprinted from [123] with the permission of Elsevier.)

the ones determined by the analysis of the SAED patterns. Hence, it could be concluded that the $MoNi_4$ and MoO_3 phases prevail in the powder with high Ni content (electrodeposited at the Ni/Mo ratio 1/0.3), while some amount of NiO phase has also been detected.

5.4.6.2 The TEM Analysis of Electrodeposited Mo-Rich Mo–Ni–O Powders

A general appearance of Mo-rich sample does not differ much from the Ni-rich sample. The TEM of typical amorphous cluster is shown in Fig. 5.64a. In the small crystalline areas (x1) traces of $MoNi_4$ and MoO_3 phases were detected and their diffraction patterns are presented in Fig. 5.64b, c, respectively. The diffraction lines in Fig. 5.64b are barely visible, indicating amorphous character of the

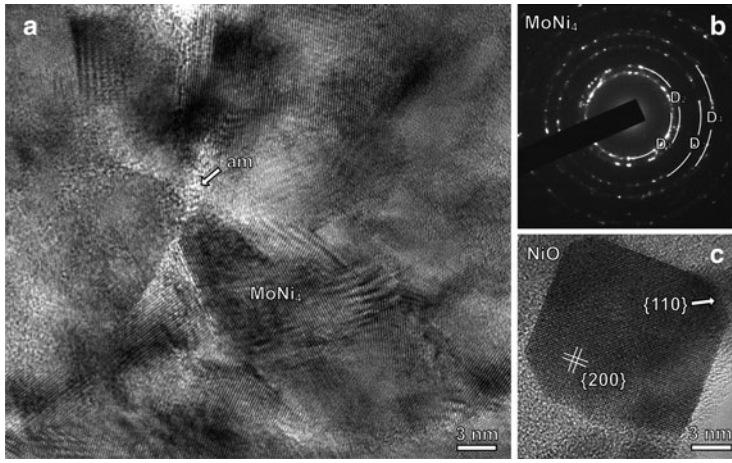

Fig. 5.63 (**a**) High-resolution TEM image of intergrown $MoNi_4$ nanocrystals. In the pockets of $MoNi_4$ grains there are remnants of uncrystallized amorphous phase (am). (**b**) SAED pattern shows rings of high intensity spots at reciprocal distances corresponding to $MoNi_4$ phase. The strongest reflections were indexed to $D_1 = \{211\}$, $D_2 = \{002\}$, $D_3 = \{132\}$, and $D_4 = \{501\}$. (**c**) Idiomorphic NiO particle (rock-salt structure) with well-resolved {200} lattice planes. The crystal is faceted with cube {001} and dodecahedral {110} faces (Reprinted from [123] with the permission of Elsevier.)

$MoNi_4$ phase, while much stronger diffraction lines for the MoO_3 phase (Fig. 5.64c) indicate its more pronounced crystallinity. In this sample the presence of NiO phase has not been detected.

It appears that in both samples $MoNi_4$ phase is more strongly bound to the amorphous phase than the oxide phases. This might be the reason why in our previous investigation [121, 122] this phase has clearly been detected by XRD in the recrystallized samples only after annealing at 600°C, while at all other temperatures a broad peak around $2\theta = 44°$ was only an indication of its existence.

It should be emphasized here that most of the phases detected in the recrystallized electrodeposited Mo–Ni–O powders [121, 122] ($MoNi_4$ and MoO_3) were also found in as-deposited Mo–Ni–O powders, indicating their formation during the process of alloy electrodeposition.

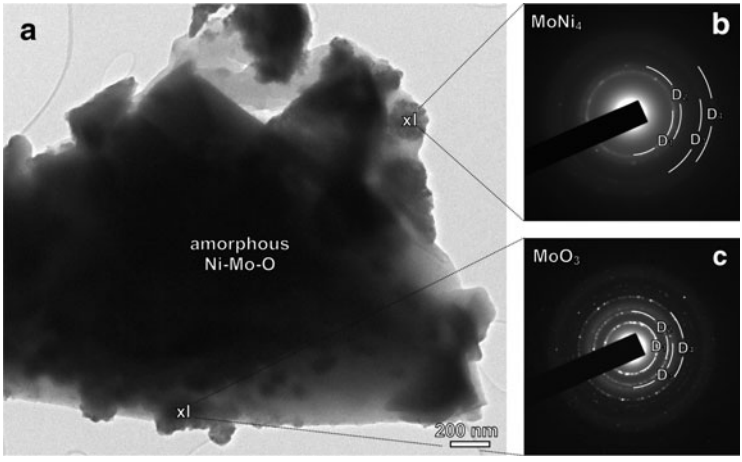

Fig. 5.64 (**a**) TEM image of the amorphous Mo–Ni–O cluster containing some crystalline areas in the powder electrodeposited at the Ni/Mo ratio 1/3. (**b**) SAED pattern from the area rich in $MoNi_4$ nanocrystals, similar to those in the Ni-rich sample, shown in this figure. (**c**) SAED pattern of the area containing MoO_3 nanocrystals, similar to those in the Ni-rich sample, shown in Fig. 5.63 (Reprinted from [123] with the permission of Elsevier.)

As stated earlier the most probable mechanism for Ni and Mo codeposition is the one reported by Podlaha and Landolt [117–120] after X-ray fluorescence analysis of the electrodeposited alloy. Their investigations were performed under controlled mass transport conditions (rotating cylinder electrode). The model assumes that the Ni electrodeposition occurs on the surface not covered by the molybdate ions as a reaction intermediate, by direct reduction of nickel species (all of them being complex of Ni^{2+} cations with the citrate anions), independently on the molybdate reaction which can occur only in the presence of nickel species [117–120]. The model of the Mo–Ni alloy electrodeposition is described by the following reduction reactions:

$$NiCit^{-} + 2e^{-} \rightarrow Ni(s) + Cit^{3-}, \tag{5.17}$$

$$MoO_4^{2-} + NiCit^- + 2H_2O + 2e^- \rightarrow [NiCitMoO_2]_{ads}^- + 4OH^- \tag{5.18}$$

$$[NiCitMoO_2]_{ads}^- + 2H_2O + 4e^- \rightarrow Mo(s) + NiCit^- + 4OH^- \tag{5.19}$$

$$H_2O + e^- \rightarrow \frac{1}{2}H_2 + OH^- \tag{5.20}$$

assuming that the Mo–Ni alloy electrodeposition is always accompanied by the simultaneous hydrogen evolution [reaction (5.20)]. This model has been recently confirmed, since the existence of adsorbed intermediate $[NiCitMoO_2]_{ads}^-$ by the in situ surface Raman spectroscopic studies has been detected [154]. However, it should be noted here that the whole mechanism has been based on the X-ray fluorescence analysis of the electrodeposited alloys, and from the content of Ni and Mo their partial current densities of electrodeposition were calculated and used for the analysis of the mechanism [117–120].

In our investigations Ni^{2+} ions were complexed with ammonia. Six complexes of nickel with ammonium anion can be formed (their stability constants are also given): [124]

$$Ni^{2+} + NH_3 \leftrightarrow [Ni(NH_3)]^{2+} \quad K_1 = 6.31 \times 10^2 \tag{5.21}$$

$$Ni^{2+} + 2NH_3 \leftrightarrow [Ni(NH_3)_2]^{2+} \quad K_2 = 2.51 \times 10^5 \tag{5.22}$$

$$Ni^{2+} + 3NH_3 \leftrightarrow [Ni(NH_3)_3]^{2+} \quad K_3 = 5.89 \times 10^6 \tag{5.23}$$

$$Ni^{2+} + 4NH_3 \leftrightarrow [Ni(NH_3)_4]^{2+} \quad K_4 = 9.12 \times 10^7 \tag{5.24}$$

$$Ni^{2+} + 5NH_3 \leftrightarrow [Ni(NH_3)_5]^{2+} \quad K_5 = 5.13 \times 10^8 \tag{5.25}$$

$$Ni^{2+} + 6NH_3 \leftrightarrow [Ni(NH_3)_6]^{2+} \quad K_6 = 5.49 \times 10^8 \tag{5.26}$$

Another complex which could be involved in the reaction mechanism is $[Ni(OH)_3]^-$ complex. Taking into account that the

solution pH is 9, the concentration of OH^- ions is very low (of the order of 10^{-5} M), while the concentration of ammonium ions is 1.7 M. Due to the low dissociation constant of ammonium hydroxide, actual concentration of ammonia in such solution is 0.6 M [155]. According to the literature [156], the dominant complex of nickel is $[Ni(NH_3)_3]^{2+}$, formed by reaction (5.23), although its stability constant is not the highest. Hence, this complex is involved in the reaction of Mo–Ni–O powder deposition.

Taking into account that NiO, MoO_3, and $MoNi_4$ phases were detected in as-deposited samples by TEM, it is obvious that the mechanism of alloy electrodeposition similar to the one presented by equations (5.17)–(5.20) could be applied for the formation of $MoNi_4$ phase only, since it assumes complete reduction of both metal ions. By the analogy with the mechanism proposed by Podlaha and Landolt [117–120], we believe that the $MoNi_4$ phase could be formed by the following mechanism:

$$[Ni(NH_3)]^{2+} + 2e^- \rightarrow Ni(s) + 3NH_3 \tag{5.27}$$

$$MoO_4{}^{2-} + [Ni(NH_3)_3]^{2+} + 2H_2O + 2e^- \rightarrow [Ni(NH_3)_3MoO_2]_{ads}{}^{2+} + 4OH^- \tag{5.28}$$

$$[Ni(NH_3)_3MoO_2]_{ads}{}^{2+} + 2H_2O + 4e^- \rightarrow Mo(s) + [Ni(NH_3)_3]^{2+} + 4OH^- \tag{5.29}$$

The most probable mechanism for the MoO_3 phase formation is

$$MoO_4{}^{2-} + [Ni(NH_3)_3]^{2+} + H_2O + 2e^- \rightarrow MoO_3 + Ni(s) + 3NH_3 + 2OH^- \tag{5.30}$$

The presence of NiO phase cannot be explained by the reduction of nickel complex. According to Palmer et al. [157] NiO could be formed by following chemical reactions:

$$Ni^{2+} + H_2O \rightarrow NiO + 2H^+ \tag{5.31}$$

$$[Ni(OH)]^{+} \rightarrow NiO + H^{+} \tag{5.32}$$

$$[Ni(OH)_2] \rightarrow NiO + H_2O \tag{5.33}$$

$$[Ni(OH)_3]^{-} + H^{+} \rightarrow NiO + 2H_2O \tag{5.34}$$

Reactions (5.31), (5.32), and (5.34) are highly impossible since Ni^{2+}, $[Ni(OH)]^{+}$, and $[Ni(OH)_3]^{-}$ are not present in the solution, while the reaction (5.33) could be considered as possible (as explained below). Although at a given pH the concentration of the OH^{-} ions is very low (of the order of 10^{-5} M), due to massive hydrogen evolution during the process of powder electrodeposition, reaction (5.20), the concentration of the OH^{-} ions in the vicinity of the electrode surface significantly increases and the reaction between OH^{-} ions and $[Ni(NH_3)_6]^{2+}$ can occur producing $[Ni(OH)_2]$, since the stability constant for $[Ni(OH)_2]$ is two orders of magnitude higher than that for $[Ni(NH_3)_3]^{2+}$. Hence, $[Ni(OH)_2]$ could be formed by the reaction

$$[Ni(NH_3)_3]^{2+} + 2OH^{-} \rightarrow [Ni(OH)_2] + 3NH_3 \tag{5.35}$$

Formed $[Ni(OH)_2]$ becomes entrapped in the deposit to a certain extent. During the procedure of powder drying at 120°C, reaction (5.33) can take place. The "transition temperature at which nickel hydroxide dehydrates to form the oxide is *ca.* 75°C" [Eq. (5.33)] [157]. Thus, the most possible way for the NiO formation is dehydration of entrapped $[Ni(OH)_2]$ during the procedure of powder drying. In such a case smaller amount of the NiO phase than the amounts of other phases (MoO_3 and $MoNi_4$) should be expected in the deposit, as it was the case in the TEM analysis [123].

Hence, it seems that complete reduction of both metal ions occurs to some extent [reactions (5.27)–(5.29)] forming $MoNi_4$ phase, but the MoO_3 and NiO phases must be produced by additional reactions, (5.30), (5.33) and (5.35), respectively. It is important to note that the formation of metallic Ni(s) is a result of two reactions, (5.27) and (5.30), and that this could be the reason for a formation of $MoNi_4$ phase during complete reduction of both metal ions by

reactions (5.27)–(5.29). Of course, it should be stated here that the most probable mechanism proposed by Podlaha and Landolt [117–120] is valid for the deposition of compact deposits from citrate containing solution (although there is an indication for the presence of oxygen in the compact deposits too [152–154]), while we were investigating powder electrodeposition from different ammonium sulfate solution. On the other side, it seems reasonable to assume that the electrodeposition mechanism does not depend on the potential (current) and that it should be the same for the deposition of compact and powderous deposits.

After these findings it is much easier to understand the process of solid state reaction that is supposed to take place during the annealing of these powders [121, 122]. The formation of $NiMoO_4$ phase should be the consequence of the reaction between NiO and MoO_3 in the solid state, which takes place at a temperature of about 600°C [150, 158, 159] and is more pronounced in the Ni-rich Mo–Ni–O powder [122].

5.5 Conclusions

The composition of the electrolyte, i.e., Ni^{2+}/Co^{2+} ions ratio, influences polarization curves for Co–Ni alloy powders electrodeposition, as well as alloy powder composition and morphology. It is also concluded that the shape of the polarization curves in all cases is practically defined by the shape of the polarization curve for hydrogen evolution. In the case of Ni powder cauliflower and spongy-type particles are detected, while Co powder contains only spongy-type particles. Both types of particles are present in the Co–Ni alloy powders obtained at Ni^{2+}/Co^{2+} ions ratios 4.00, 1.50, and 0.67, while only spongy-type particles are detected in the Co–Ni alloy powder obtained at Ni^{2+}/Co^{2+} ions ratio 0.25. In all cases of alloy powder electrodeposition anomalous type of codeposition is detected.

The morphology and composition of electrodeposited Fe–Ni alloy powders depend on the Ni/Fe ions concentration ratio in both electrolytes. Anomalous codeposition of Fe and Ni has been

confirmed by the EDS analysis of alloy powders, being more pronounced in the electrolyte containing Fe(III) salts due to the possibility of $Fe(OH)_2$ formation. A common characteristic for all alloy powder samples was the presence of cone-shaped cavities and nodules. The possibility of the formation of single crystal $FeNi_3$ phase was found to exist in both electrolytes. It appears that it is better to use electrolyte with Fe(II) salts, independently of the supporting electrolyte, since the current efficiency for Fe–Ni powder electrodeposition is much higher than that from the solution containing Fe(III) salts.

After annealing in air at 400°C, 600°C, and 700°C for 3 h all alloy powders oxidized forming NiO, $NiFe_2O_4$, and Fe_2O_3 with the NiO phase disappearing in the samples with higher percentage of Fe. The $NiFe_2O_4$ phase was found to be dominant in the sample with the highest percentage of Fe annealed at 600°C. From the EDS and XRD analysis it could be concluded that the powders were not completely oxidized during annealing in air at 400°C and 600°C.

The morphology, chemical, and phase composition of as-deposited and annealed Mo–Ni–O powders depend on the Ni/Mo ions concentration ratio. XRD and SEM analysis revealed that all alloy powders are partially recrystallized already at 300°C, showing the presence of MoO_3 and $NiMoO_4$ phases. After annealing at 600°C complete recrystallization of all powders is confirmed by SEM analysis, showing the absence of any powder agglomerates and the presence of well-defined crystal grains. In the powder electrodeposited at the Ni/Mo ratio 1/0.3 XRD revealed the presence of only one phase, $NiMoO_4$, indicating that a single phase powder of the system Ni–Mo–O could be obtained by proper choice of electrodeposition parameters. At the same time the disappearance of MoO_3 phase for this sample confirmed that the phase transition from MoO_3 into $NiMoO_4$ phase occurred during annealing at 600°C. The TEM and XRD analysis revealed that two types of particles could be detected in both Ni-rich and Mo-rich as-deposited powders: amorphous and crystalline particles. Among the crystalline particles in both powders MoO_3 and $MoNi_4$ phases prevail, while in the Ni-rich powder NiO phase has also been detected. Based on these findings the corresponding mechanism of Mo–Ni–O powders electrodeposition has been proposed.

Acknowledgments This work was financially supported by the Ministry of Education and Science of the Republic of Serbia through the Projects No. 1806/2002, No. 142032G/2006, and No. 172054/2011.

The authors are indebted to D. Poleti from the Faculty of Technology and Metallurgy University of Belgrade, Serbia, for DSC-TGA analysis.

The authors are also indebted to V.M. Maksimović from the Institute of Nuclear Sciences—Vinča, Belgrade, Serbia, for the XRD analysis of all investigated systems.

Special thanks to A. Rečnik from the Jožef Stefan Institute, Ljubljana, Slovenia, for TEM analysis of as-deposited samples.

The authors also wish to express their gratitude to M.G. Pavlović, Institute of Electrochemistry ICTM, Belgrade, Serbia, for useful discussions in the case of the Co–Ni system.

References

1. Papers CT, Brabyn SM (1987) Met Powder Rep 42:863
2. Ekemar S, Lindholm L, Hartzell T (1982) Int J Refract H 1:37
3. Erol S, Nursel D (1999) J Adhes Sci Technol 13:679
4. Rehim SS, Halim AM, Osman MM (1985) J Appl Electrochem 15:107
5. Laughlin D, Lu B, Hsu Y, Zou J, Lambeth D (2000) IEEE Trans Magn 36:48
6. Vassal N, Salmon E, Fauvarque J (1999) J Electrochem Soc 146:20
7. Benvenuti F, Carlini C, Marchetti F, Marchionna M, Galletti A, Sbrana G (2001) J Organomet Chem 622:286
8. Tsay M, Chang F (2000) Appl Catal A Gen 203:15
9. Diskin A, Cunningham R, Ormerod R (1998) Catal Today 46:147
10. Kapoor S, Salunke HG, Tripathi AK, Kulshreshtha SK, Mittal JP (2000) Mater Res Bull 35:143
11. Ishihara T, Horiuchi N, Inoue T, Eguchi K, Takita Y, Arai H (1992) J Catal 136:232
12. Kikuko K, Teruh iko I (1998) Jpn Kokai Tokkyo Koho JP 10302790
13. Bianco A, Gusmano G, Montanari R, Montesperelli G, Traversa E (1994) Mater Lett 19:263
14. Bianco A, Gusmano G, Montanari R, Montesperelli G, Traversa E (1995) Thermochim Acta 269(270):117
15. Aymard L, Dumont B, Viau G (1996) J Alloys Compd 242:108
16. Huang J, Wu Y, Ye H (1996) Acta Mater 44:1201
17. Koltypin Y, Katabi G, Cao X, Prozorov R, Gedanken A (1966) J Non Cryst Solids 201:159
18. Kapoor S, Salunke H, Tripathi A, Kulshreshta S, Mittal J (2000) Mater Res Bull 35:143

19. Kurikka V, Gedanken A, Prozorov R, Revesz A, Lendvai J (2000) J Mater Res 15:332
20. Fievet F, Lagier J, Blin B, Meaudoin B, Figlarz M (1989) Solid State Ionics 32(33):198
21. Li Y, Li L, Liao H, Wang H, Qian Y (1999) J Mater Chem 9:2675
22. Degen A, Macek J (1999) Nanostruct Mater 12:225
23. Gibson KP (1995) Science 267:1338
24. Chen D, Wu S (2000) Chem Mater 12:1354
25. Zhang D-E, Ni X-M, Zhang X-J, Zheng H-G (2006) J Magn Magn Mater 302:290
26. Hayashi T, Ohno T, Yatsuda S, Uyeda R (1977) Jpn J Appl Phys 16:705
27. Dong L, Zhang Z, Jin S, Sun W, Chuang Y (1998) Nanostruct Mater 10:585
28. Bianco A, Gusmano G, Montanari R, Montesperelli G, Traversa E (1995) Thermochim Acta 269:117
29. Viau G, Ravel F, Acher O, Fiévet-Vincent F, Fiévet F (1995) J Magn Magn Mater 144:377
30. Gao X, Chen D, Dollimore D, Skrzypczak-Jankum E, Burckel P (1993) Thermochim Acta 220:75
31. Neddermann R, Binnewies M (1996) Z Anorg Allg Chem 622:17
32. Girirdin D, Maurer M (1990) Mater Res Bull 25:119
33. Xiaoli X, Zuoren N, Yabao J, Peiyun T, Shunlin S, Jie X, Tieyong Z (2008) J Alloys Compd 466:387
34. Jang HC, Ju SH, Kang YC (2009) J Alloys Compd 478:206
35. Abd El-Halim AM, Khalil RM (1986) Surf Coat Technol 27:103
36. Yur'ev BP, Golubkov LA (1969) Trudy—Leningradskii Politekhnicheskii Institut imeni M. I. Kalinina 14:269
37. Jović VD, Maksimović V, Pavlović MG, Popov KI (2006) J Solid State Electrochem 10:373
38. Jović VD, Jović BM, Pavlović MG, Maksimović V (2006) J Solid State Electrochem 10:959
39. Jović VD, Jović BM, Maksimović V, Pavlović MG (2007) Electrochim Acta 52:4254
40. Jović VD, Jović BM, Pavlović MG (2006) Electrochim Acta 51:5468
41. Jović VD, Maksimović V, Pavlović MG, Jović BM (2006) Mater Sci Forum 518:307
42. Maurice DR, Courtney TH (1990) Metall Mater Trans A 21A:289
43. Hamzaoui R, Elkedim O, Greneche JM, Gaffet E (2005) J Magn Magn Mater 294:e145
44. Hamzaoui R, Elkedim O, Gaffet E (2004) Mater Sci Eng A 381:363
45. Valderruten JF, Perez Alcazar GA, Greneche JM (2006) Phys B 384:316
46. Zhou PH, Deng LJ, Xie JL, Liang DF, Chen L, Zhao XQ (2005) J Magn Magn Mater 292:325
47. Kaloshkin SD, Tcherdyntsev VV, Tomilin IA (2001) Phys B 299:236
48. Tcherdyntsev VV, Kaloshkin SD, Tomilin LA, Shelekhov EV, Baldokhin YuV (1999) Nanostruct Mater 12:139

49. Baldokhin YuV, Tcherdyntsev VV, Kaloshkin SD, Kochetov GA, Pustov YuA (1999) J Magn Magn Mater 203:313
50. Baldokhin YV, Kolotyrkin PY, Petrov YI, Shafranovsky EA (1994) Phys Lett A 189:137
51. Schirmer B, Wuttig M (1999) Phys Rev B 60:945
52. Kuhrt C, Schultz L (1993) J Appl Phys 73:1975
53. Jartych E, Zurawicz JK, Oleszak D, Pekala M (2000) J Magn Magn Mater 208:221
54. Koohkana R, Sharafia S, Shokrollahib H, Janghorbanb K (2008) J Magn Magn Mater 320:1089
55. Pandey B, Verma HC (2007) J Phys Condens Matter 19:406207
56. Wang H, Liu Q, Zhang J, Hsu TY (Zuyao X) (2003) Nanotechnology 14:696
57. Schneeweissa O, Davida B, Zaka T, Zborilb R, Mashlanb M (2007) J Magn Magn Mater 310:e858
58. Song HB, Lee KJ, Kim KH, Oh ST, Lee SK, Choa YH (2010) J Nanosci Nanotechnol 10:106
59. Kim KH, Yu JH, Lee SB, Lee SK, Choa YH, Oh ST, Kim JR (2008) IEEE Trans Magn 44:3805
60. Kasagi T, Tsutaoka T, Hatakeyama K (1999) IEEE Trans Magn 35:3424
61. Oh ST, Joo MH, Choa YH, Kim KH, Lee SK (2010) Phys Scr T139:014050
62. Lačnjevac U, Jović BM, Jović VD (2009) Electrochim Acta 55:535
63. Lačnjevac U, Jović BM, Maksimović VM, Jović VD (2010) J Appl Electrochem 40:701
64. Zhelibo EP, Kravets NN, Gamarkin MYu, Remez SV (1995) Powder Metall Metal Ceram 34:113
65. Zhelibo EP, Kravets NN (1997) Powd Metall Metal Ceram 36:264
66. Chu CM (2003) J Chin Inst Eng 34:689
67. Morrish AH, Haneda KJ (1981) Appl Phys 52:2496
68. Ishino K, Narumiya Y (1987) Am Ceram Soc Bull 66:1469
69. Zhang Q, Itoh T, Abe M, Tamaura Y (1992) In: Yamaguchi T, Abe M (eds) Proceedings of the 6th international conference on ferrites. The Japan Society of Powder and Powder Metallurgy, Tokyo, p 481
70. Dube GR, Darshane YS (1993) J Mol Catal 79:285
71. Gopal Reddy CV, Manorama SV, Rao VJ (1999) Sens Actuators B Chem 55:90
72. Satyanarayana LK, Reddy KM, Manorama SV (2003) Mater Chem Phys 82:21
73. Abe M, Itoh T, Tamaura Y et al (1998) J Appl Phys 63:3774
74. Itoh T, Abe M, Sasao T et al (1989) IEEE Trans Magn 25:4230
75. Suran G, Heurtel A (1972) J Appl Phys 43:536
76. Naoe M, Yamanaka S (1970) Jpn J Appl Phys 9:293
77. Marshall DJ (1971) J Cryst Growth 9:305
78. Gibart P, Robbins M, Kane AB (1974) J Cryst Growth 24–25:166
79. Pulliam GR (1967) J Appl Phys 38:1120
80. Mee JE, Pulliam GR, Archer JL et al (1969) IEEE Trans Magn 5:717

81. Fitzgerald AG, Engin R (1974) Thin Solid Films 20:317
82. Itoh H, Takeda T, Naka S (1986) J Mater Sci 21:3677
83. Tsuchiya T, Yamashiro H, Sei T et al (1992) J Mater Sci 27:3645
84. Jung DS, Kang YC (2009) J Magn Magn Mater 321:619
85. Deschanres JL, Langlet M, Joubert JC (1990) J Magn Magn Mater 83:437
86. Lee PY, Ishizaka K, Suematsu H et al (2006) J Nanocryst Res 8:29
87. Sartale SD, Lokhande CD, Giersig M et al (2004) J Phys Condens Matter 16:773
88. Fang J, Shama N, Tung L et al (2003) J Appl Phys 93:7483
89. Ceylan A, Ozcan S, Ni C et al (2008) J Magn Magn Mater 320:857
90. Kinh VO, Chassaing E, Saurat M (1975) Electrodep Surf Treat 3:205
91. Yao SW, Zeng Y, Guo HT (1994) Surf Tech (Japan) 45:643
92. Friend WZ (1980) Corrosion of nickel and nickel-base alloys. Wiley Interscience, New York, p 248
93. Kriz JF, Shimada H, Yoshimura Y, Matsubayashi N, Nishijama A (1995) Fuel 74:1852
94. Astier MP, Dji G, Teichner SJ (1991) Appl Catal 72:321
95. Tsenta TE, Knyazheva VM, Svistunova TV, Kolotyrkin YM, Zakharin DS (1989) Prot Met 25:28
96. Beltowska-Lehman E (1990) J Appl Electrochem 20:132
97. Drown DE, Mahmood MN, Turner AK, Hall SM, Fogarty PO (1982) Int J Hydrogen Energy 7:405
98. Huot JY, Brossard L (1988) J Appl Electrochem 18:815
99. Conway BE, Bai L, Sattar MA (1987) Int J Hydrogen Energy 12:607
100. Raj IA, Vasu KI (1992) J Appl Electrochem 22:471
101. Conway BE, Bai L, Tessier DF (1984) J Electroanal Chem 161:39
102. Fan C, Piron DL, Paridis P (1994) Electrochim Acta 39:2715
103. Conway BE, Bai L (1985) J Chem Soc Faraday Trans I 81:1841
104. Raj IA, Kovenkatesan V (1988) Int J Hydrogen Energy 12:215
105. Fan C, Piron DL, Sleb A, Paridis P (1994) J Electrochem Soc 141:382
106. Divisek J, Schmotz H, Balej J (1989) J Appl Electrochem 19:519
107. Lasia A, Rami A (1990) J Electroanal Chem 294:123
108. Jakšić JM, Vojnović MV, Krstajić NV (2000) Electrochim Acta 45:4151
109. Gennero de Chialvo MR, Chialvo AC (1998) J Electroanal Chem 448:87
110. Jakšić MM (1989) Mater Chem Phys 22:1
111. Kedzierzawski P, Oleszak D, Janik-Czachor M (2001) Mater Sci Eng A300:105
112. Oleszak D, Portnoy VK, Matyja H (1999) Mater Sci Forum 312:345
113. De la Torre SD, Oleszak D, Kakitsuji A, Miyamoto K, Miyamoto H, Martinez SR, Almeraya CF, Martinez VA, Rois JD (2000) Mater Sci Eng A276:226
114. Goswami GL, Kumar S, Galun R, Mordike BL (2003) Lasers Eng 13:1
115. Bhattacharjee PP, Ray RK, Upadhyaya A (2006) Physica C449:116
116. Brenner A (1963) Electrodeposition of alloys. Priniciples and practice, vol 2. Academic, New York

117. Podlaha EJ, Landolt D (1996) J Electrochem Soc 143:885
118. Podlaha EJ, Landolt D (1996) J Electrochem Soc 143:893
119. Podlaha EJ, Landolt D (1997) J Electrochem Soc 144:1672
120. Marlot A, Kern P, Landolt D (2002) Electrochim Acta 48:29
121. Jović BM, Jović VD, Maksimović VM, Pavlović MG (2008) Electrochim Acta 53:4796
122. Lačnjevac U, Jović BM, Baščarević Z, Maksimović VM, Jović VD (2009) Electrochim Acta 54:3115
123. Jović VD, Jović BM, Lačnjevac U, Branković G, Bernik S, Rečnik A (2010) Electrochim Acta 55:4188
124. Dean JA (1985) Lange's handbook of chemistry, 13th edn. Mc-Graw Hill, New York, p 5
125. Despić AR, Jović VD (1995) In: White RE et al (eds) Modern aspects of electrochemistry, chap 2, vol 27. Plenum, New York
126. Horkans J (1979) J Electrochem Soc 126:1861; (1981) J Electrochem Soc 128:45
127. Jepson F, Meecham S, Salt FW (1955) Trans Inst Met Finish 32:160
128. Young CBF, Struyk C (1946) Trans Electrochem Soc 89:383
129. Schoch EP, Hirsch A (1907) Trans Am Electrochem Soc 11:135
130. Jović VD, Tošić N, Stojanović M (1997) J Electroanal Chem 420:43
131. Lönnberg B (1994) J Mater Sci 29:3224
132. Hansen M, Andrenko K (1958) Constitution of binary alloys. Mc-Graw Hill, New York
133. Calusaru A (1979) Electrodeposition of powders from solutions. Elsevier, New York
134. Wranglen G (1960) Electrochim Acta 2:1845
135. Kieling VC (1997) Surf Coat Technol 96:135
136. Bard AJ, Faulkner LR (2001) Electrochemical methods: fundamentals and applications, 2nd edn. Wiley, New York
137. Zhou XM, Wei XW (2009) Cryst Growth Des 9:7
138. Popov KI, Djokić SS, Grgur BN (2002) Fundamental aspects of electrometallurgy. Kluwer, New York
139. Chassaing E, Portal N, Levy AF, Wang G (2004) J Appl Electrochem 34:1085
140. Sanches LS, Domingues SH, Marino CEB, Mascaro LH (2004) Electrochem Commun 6:543
141. Donten M, Celsiulis H, Stojek Z (2005) Electrochim Acta 50:1405
142. Morgenstern T, Lienhardt JL, Reichelt W, Koenig U, Oppermann H (1993) Mater Sci Forum 133–136:627
143. Pejryd L (1985) Scand J Metall 14:268
144. Hussain OM, Ramana CV, Zaghib K, Julien CM (2006) In: Chowdari BVR et al (eds) Proceedings of the 10th Asian conference on solid state ionics: advanced materials for emerging technologies. World Scientific, River Edge, NJ, p 136
145. McCarron EM III (1986) J Chem Soc Chem Commun 336

146. Parise JB, McCarron EM III, Sleight W (1987) Mater Res Bull 22:803
147. Smith GW (1962) Acta Cryst 15:1054
148. Smith GW, Ibers JA (1965) Acta Cryst 19:269
149. Abrahams SC, Reddy JM (1965) J Chem Phys 43:2533
150. Sleight AW, Chamberland BL (1968) Inorg Chem 7:1672
151. Plyasova LM, Ivanchenko IYu, Andrushkevich MM, Buyanov RA, Itenberg ISh, Khramova GA, Karakchiev LG, Kustova GN, Stepanov GA, Tsailingold AL, Pilipenko FS (1973) Kinet Catal 14:1010
152. Harker D (1944) J Chem Phys 12:315
153. Parise JB et al (1991) J Solid State Chem 93:193
154. Zeng Y, Li Z, Ma M, Zhou S (2000) Electrochem Commun 2:36
155. Min X, Zhou M, Chai L, Wang Y, Shu Y (2009) Trans Nonferrous Met Soc China 19:1360
156. Younes O, Gileadi E (2002) J Electrochem Soc 149:C100
157. Palmer DA, Benezeth P, Wesolowski DJ (2005) In: Proceedings of the 14th international conference on the properties of water and steam, Kyoto, p 264
158. Trambouze Y, Colleuille Y, The TH, Hebd CR (1956) Seances Acad Sci Ser C 242:497
159. Yanushkevich TM, Zhukovskii VM, Ust'yantsev VM (1974) Russ J Inorg Chem 19:1056